

**ISAS - INTERNATIONAL SCHOOL  
FOR ADVANCED STUDIES**

**Structure-Function Relationship of  
Nickel-containing Superoxide Dismutase  
from *Streptomyces seoulensis***

Thesis submitted for the degree of  
“Doctor Philosophiae”

CANDIDATE  
Jochen Wuerges

SUPERVISOR  
Dr. Kristina Djinovic Carugo

Trieste  
October 2003

## DECLARATION

The work described in this dissertation was carried out at the Structural Biology Laboratory, Sincrotrone ELETTRA, Trieste (Italy) within the PhD course in Biophysics of the International School for Advanced Studies, Trieste (Italy) between November 1999 and September 2003. All the results reported here arise from my own experiments. This work has not been submitted in whole or in part to any other university.

## ABSTRACT

Superoxide dismutases (SOD) are enzymes that play an important role in the defence against oxidative stress and are found ubiquitously in oxygen metabolising organisms. The substrate of SOD is the superoxide radical anion which is responsible both for direct damage of biological molecules and for generating other reactive oxygen species. Superoxide is generated by a one electron transfer to dioxygen and its concentration is kept in low limits by SODs. SODs are generally classified according to the metal species which acts as redox-active centre to catalyse the overall dismutation reaction  $2\text{O}_2^{\bullet-} + 2\text{H}^+ \rightarrow \text{O}_2 + \text{H}_2\text{O}_2$ . Until recently, three different metal species have been found; copper- and zinc-containing SOD, with copper as the catalytically active metal, manganese-containing SOD, and iron-containing SOD. More recently a new superoxide dismutase containing nickel (NiSOD) was purified from a variety of *Streptomyces* species and characterized biochemically as well as spectroscopically. NiSOD was suggested to represent a novel class of superoxide dismutases on its own since no sequence homology is found to enzymes of the Cu,ZnSOD class or the MnSOD/FeSOD class.

The present PhD thesis has the aim to provide structural information which is needed to understand the function of NiSOD in detail. NiSOD from the aerobic soil bacterium *Streptomyces seoulensis* was crystallized in two crystal forms. The phase problem was solved by the multiple-wavelength anomalous dispersion (MAD) method exploiting anomalous scattering at the K-absorption edge of nickel. The three-dimensional molecular structures of resting, chemically and X-ray reduced enzyme were refined to a resolution of up to 1.6 Å and are analysed.

NiSOD is found to be distinct from SODs of both other classes regarding oligomeric state, subunit structure and active site. It is a homohexamer of four-helix-bundle subunits where each subunit hosts an active site in an N-terminal loop. In the resting enzyme, the Ni(III) site is five-coordinate in a square pyramidal geometry by the amino-terminal and imidazole nitrogen N $\delta$  of His 1, the amide nitrogen and thiolate sulfur of Cys 2, and the thiolate sulfur of Cys 6. The reduced enzyme state was obtained either by thiosulfate soaking of crystals or by X-ray induced reduction in the course of exposure to high X-ray doses. Loss of the axial ligand His 1 N $\delta$  is observed upon reduction to Ni(II). Neither the nickel ion nor its ligands except His 1 N appear to be solvent accessible through a small pocket in the enzyme's surface. This pocket shows a narrow bottleneck at its entrance and may account for substrate specificity. Long-range electrostatic attraction of superoxide anions to this pocket is not of importance for NiSOD's activity in contrast to other SOD classes.

# Contents

<b>1</b>	<b>Introduction</b>	<b>1</b>
<b>I</b>	<b>Oxidative Stress and Superoxide Dismutases</b>	<b>3</b>
<b>2</b>	<b>Oxidative Stress</b>	<b>4</b>
<b>3</b>	<b>Superoxide Dismutases</b>	<b>7</b>
3.1	General Features . . . . .	7
3.2	SOD Classes and their Distribution . . . . .	9
3.3	Structural Description of Cu,ZnSOD, MnSOD & FeSOD . . . . .	9
3.4	Biochemical Description of Cu,ZnSOD, MnSOD & FeSOD . . . . .	11
<b>II</b>	<b>The Ni-containing Superoxide Dismutase from <i>Streptomyces seoulensis</i></b>	<b>14</b>
<b>4</b>	<b>Introduction to Ni-containing Superoxide Dismutases</b>	<b>15</b>
4.1	Distribution of NiSOD . . . . .	15
4.2	Expression of NiSOD . . . . .	15
4.3	Biochemical and Spectroscopic Studies on NiSOD . . . . .	17
<b>5</b>	<b>Crystallization of NiSOD</b>	<b>23</b>
5.1	Screening for Crystallization Conditions . . . . .	23
5.2	Crystals of thiosulfate-reduced NiSOD . . . . .	25
5.3	Crystals of inhibited NiSOD . . . . .	26
5.4	Xenon & Heavy Metal Derivatization . . . . .	26
5.5	Preliminary Crystallographic Analysis . . . . .	28
<b>6</b>	<b>Determination of the NiSOD Structure</b>	<b>30</b>
6.1	X-ray Data Collection and Processing . . . . .	30
6.2	Determination of Ni-sites . . . . .	32
6.3	Determination of Phases by MAD . . . . .	35
6.4	Phase Improvements . . . . .	38
6.5	Model Building & Refinement . . . . .	39
<b>7</b>	<b>Crystal Structures of NiSOD</b>	<b>46</b>
7.1	Overall Structure . . . . .	46

7.2	Subunit Structure and Interactions . . . . .	48
7.3	Active site Structure . . . . .	51
7.3.1	Resting Enzyme . . . . .	51
7.3.2	Thiosulfate-Reduced Enzyme . . . . .	55
7.4	Active site Accessibility . . . . .	56
7.5	Accessibility probed by Xenon Binding . . . . .	58
7.6	Electrostatic Steering to Active Site . . . . .	59
7.7	Inhibited NiSOD . . . . .	61
7.8	NiSOD and Cyanobacteria . . . . .	62
<b>8</b>	<b>A catalytic mechanism for NiSOD</b>	<b>64</b>
8.1	Experimental Information & their Interpretation . . . . .	64
8.2	Open Questions . . . . .	67
<b>9</b>	<b>Structural &amp; Functional Comparison</b>	<b>68</b>
9.1	NiSOD compared to other SOD Classes . . . . .	69
9.2	NiSOD compared to other Ni-containing Enzymes . . . . .	70
<b>10</b>	<b>Conclusions</b>	<b>74</b>
	<b>Appendices</b>	<b>76</b>
<b>A</b>	<b>Protein X-ray Crystallography</b>	<b>76</b>
A.1	Protein Crystallization . . . . .	76
A.2	Steps in Crystal Structure Determination . . . . .	80
A.3	Translational Non-crystallographic Symmetry . . . . .	89
<b>B</b>	<b>Spectroscopic Methods</b>	<b>93</b>
B.1	Visible/UV Spectroscopy . . . . .	93
B.2	Electron Paramagnetic Resonance Spectroscopy . . . . .	94
B.3	X-ray Absorption Spectroscopy . . . . .	99
<b>C</b>	<b>Kinetic Studies on Superoxide Dismutases</b>	<b>102</b>
C.1	General aspects of Kinetics . . . . .	102
C.2	Superoxide Dismutase Activity Assays & Kinetics . . . . .	106
	<b>Acknowledgements</b>	<b>109</b>
	<b>Bibliography</b>	<b>110</b>

# List of Figures

3.1	Cu,ZnSOD: Subunit Ribbon Representation . . . . .	10
3.2	Cu,ZnSOD: Active Site Representation . . . . .	10
3.3	MnSOD: Subunit Ribbon Representation . . . . .	11
3.4	MnSOD: Active Site Representation . . . . .	11
4.1	pH-dependence of $k_{cat}$ for NiSOD . . . . .	18
4.2	pH-stability of NiSOD . . . . .	18
4.3	Ionic Strength Dependence of NiSOD's $k_{cat}$ . . . . .	19
4.4	Visible/UV-absorption spectrum of NiSOD . . . . .	20
4.5	X-band EPR Spectra of NiSOD . . . . .	20
4.6	XANES Spectra of NiSOD . . . . .	21
5.1	Photographs of NiSOD crystals . . . . .	25
6.1	Fluorescence & Scattering Factors at the Ni K-edge . . . . .	31
6.2	Native Patterson map of Crystal Form I . . . . .	33
6.3	Anomalous Patterson maps of Crystal Form III . . . . .	33
6.4	Ni-site Arrangement & NCS Axes in NiSOD . . . . .	34
6.5	Estimation of MAD signal . . . . .	35
6.6	NCS Averaging for Phase Improvement . . . . .	39
7.1	Surface Representation of NiSOD . . . . .	47
7.2	$C_{\alpha}$ -trace Representation of NiSOD . . . . .	48
7.3	Subunit Structure of NiSOD . . . . .	49
7.4	Stabilization of NiSOD's Active Site Loop . . . . .	50
7.5	pH-dependence of NiSOD EPR spectra . . . . .	52
7.6	Active Site of Resting & X-ray Reduced NiSOD . . . . .	53
7.7	Rotation of the His 1 Imidazole upon X-ray Exposure . . . . .	54
7.8	Active Site of Thiosulfate-reduced NiSOD . . . . .	56
7.9	Active Site Accessibility in NiSOD . . . . .	57
7.10	Accessibility probed by Xenon . . . . .	59
7.11	Electrostatic Potential of NiSOD's Surface . . . . .	60
7.12	NiSOD and Cyanobacteria . . . . .	63

9.1	Active Sites of Ni-containing Enzymes . . . . .	71
A.1	Scheme of a 2D solubility diagram . . . . .	77
A.2	Set-ups for vapour diffusion crystallization . . . . .	80
A.3	Set-up of an X-ray Diffraction Experiment . . . . .	81
A.4	Nickel $f'$ and $f''$ at the K-edge . . . . .	85
A.5	Anomalous Scattering & Harker Diagrams . . . . .	86
B.1	Generation of an EPR spectrum . . . . .	96
B.2	Basic Spectra for a $S = \frac{1}{2}$ paramagnet . . . . .	97

# List of Tables

5.1	The NiSOD crystal forms . . . . .	28
6.1	Data Processing and reduction statistics . . . . .	32
6.2	Dispersive & Anomalous Differences of MAD Data . . . . .	37
6.3	Final Phasing Statistics . . . . .	38
6.4	Map Correlation Coefficients . . . . .	41
6.5	Final refinement statistics . . . . .	45
7.1	Mutagenesis Studies on NiSOD . . . . .	50
7.2	Ni-ion Bond Lengths . . . . .	55
9.1	Reactions catalysed by Ni-containing Enzymes . . . . .	70
A.1	Structure Factor Modulations in Crystal Form I . . . . .	90

# List of Abbreviations

B-factor	Crystallographic 'Temperature'-Factor
Cu,ZnSOD	Copper- and zinc-containing superoxide dismutase
EPR	Electron Paramagnetic Resonance
EXAFS	Extended X-ray Absorption Fine Structure
$f$	Scattering factor
$f'/f''$	Real/imaginary component of the anomalous scattering factor
$F_{hkl}$	Structure factor of reflection $h, k, l$
$F_{\text{obs}}/F_{\text{calc}}$	Observed/calculated structure factor amplitude
FeSOD	Iron-containing superoxide dismutase
FOM	Figure of Merit
$h, k, l$	Miller-indices of a reflection
I	Reflection-Intensity or Nuclear Spin quantum number
$k_{\text{cat}}$	Catalytic rate constant
$K_M$	Michaelis constant
$\lambda$	X-ray wavelength
M	Molar (mol per Liter)
MAD	Multiple-wavelength Anomalous Dispersion
MALDI-TOF	Matrix-assisted Laser Desorption Ionisation - Time of Flight
MIR	Multiple Isomorphous Replacement
MnSOD	Manganese-containing superoxide dismutase
NCS	Non-crystallographic Symmetry
NiSOD	Nickel-containing superoxide dismutase
NHE	Normal Hydrogen Electrode
PDB	Protein Data Bank
R-factors	Crystallographic Residual- (or Reliability-)Factors
rms	Root mean square
$\sigma$	Standard deviation
S	Spin quantum number
SAD	Single-wavelength Anomalous Dispersion
SDS-PAGE	Sodium dodecyl sulfate polyacrylamide gel electrophoresis
SOD	Superoxide Dismutase
UV	Ultra-violet
XANES	X-ray Absorption Near Edge Structure
XAS	X-ray Absorption Spectroscopy

# Chapter 1

## Introduction

Superoxide dismutases are ubiquitous metallo-enzymes which catalyse the dismutation of superoxide radicals ( $O_2^{\bullet-}$ ) to molecular oxygen ( $O_2$ ) and peroxide ( $H_2O_2$ ). This thesis focuses on the determination and interpretation of three-dimensional crystal structures of the Nickel-containing Superoxide Dismutase (NiSOD).

Research on NiSOD started in the mid 1990's in the laboratory of Prof. Sa-Ouk Kang at the Seoul National University where NiSOD was first isolated from *Streptomyces* species. Since then the enzyme has been well characterized biochemically and spectroscopically and was found also in bacteria other than *Streptomyces*. First evidence of nickel as the catalytically active metal species in NiSOD came from Electron Paramagnetic Resonance spectroscopy. In collaboration with the group of Michael J. Maroney at the University of Massachusetts, the metal environment was further investigated by X-ray absorption spectroscopic studies. In addition, kinetic studies on the enzyme using pulse radiolysis were performed. Subsequently, a collaboration between Sa-Ouk Kang and Kristina Djinovic Carugo at the Structural Biology Laboratory of the synchrotron radiation facility ELETTRA in Trieste was started to obtain three-dimensional structures of NiSOD by X-ray crystallography.

In Part I of this thesis, superoxide dismutases (SODs) are first placed in their biological context of oxidative stress in  $O_2$  metabolizing organisms (chapter 2) and then classified with respect to the superoxide dismutase family (chapter 3). The three already well-characterized SODs will be introduced to the reader. These are the Cu- and Zn-containing SOD, the first to be discovered, the Mn-containing SOD and the Fe-containing SOD.

Part II deals with NiSOD from *Streptomyces seoulensis* in particular. After a review of the literature about NiSOD, summarizing results from cell biology, biochemistry and spectroscopy (chapter 4), my work is presented starting with crystallization of the enzyme (chapter 5) and followed by determination of crystal

---

structures in chapter 6. The resulting atomic models are then described and discussed in chapter 7 which begins with the native (hexameric) architecture and then zooms in, via the subunit structure to the active site.  $\text{O}_2^{\bullet-}$ -accessibility of and long-range electrostatic  $\text{O}_2^{\bullet-}$ -attraction to the active site will subsequently be analysed. Chapter 8 summarizes and discusses all information about the catalytic mechanism of NiSOD that is so far available. It follows in chapter 9 a comparison of NiSOD to other superoxide dismutases and other Ni-containing enzymes with the aim to identify common and particular features of NiSOD. This may help to better understand important aspects of the dismutation mechanism and Ni-related catalysis, respectively, not only with regards to NiSOD itself but also regarding the enzymes used in the comparison. All findings are finally concluded in chapter 10.

Three appendices are added to provide additional background for topics which could not be mentioned in detail in the main text. They cover methods used in X-ray crystallography, in spectroscopy and in kinetical studies.

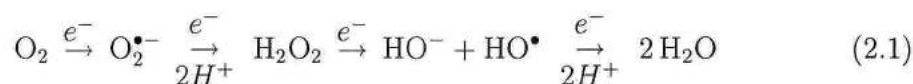
Part I

Oxidative Stress  
and  
Superoxide Dismutases

## Chapter 2

# Oxidative Stress

Oxygen-metabolizing organisms benefit energetically from the reduction of  $O_2$ , but whenever this reduction does not take place in controlled ways, they have to face the potential toxicity of oxygen. Most of the  $O_2$  reduction in respiring cells is performed by the enzyme cytochrome oxidase which does not release any intermediates during the four-electron reduction to  $2 H_2O$ . Reactive oxygen metabolites such as the superoxide radical ( $O_2^{\bullet-}$ ), peroxide ( $H_2O_2$ ) or the hydroxyl radical ( $HO^{\bullet}$ ) are generated by the incomplete reduction of  $O_2$  in the following way:



These are agents of oxidative stress and are produced, besides in a spontaneous mode, also in enzymatic reactions (Fridovich 1998a+b). Sites of their origin are the various cell compartments, in particular the mitochondria, and the extracellular space.  $O_2^{\bullet-}$  can act as reductant or oxidant and damages specific chemical groups on many important biological molecules. Some reactive oxygen metabolites show target selectivity (as e.g.  $O_2^{\bullet-}$ ) while others, as  $HO^{\bullet}$ , do not. Although  $O_2^{\bullet-}$  dismutates spontaneously with a rate of  $2 \cdot 10^5 \text{ M}^{-1}\text{s}^{-1}$  at pH 7.4 in aqueous solvents (Fridovich, 1989) and is estimated to amount to less than 1-3% of the total  $O_2$  consumption, its concentration would increase rapidly to considerable levels if there were no means of catalysing its dismutation. Cells have developed various defence systems to keep reactive oxygen metabolites under control. Those shall be described briefly now.

Superoxide dismutases dismute  $2 O_2^{\bullet-}$  to  $O_2$  and  $H_2O_2$ . They will be discussed in detail throughout this thesis and therefore only a distinct enzyme family with  $O_2^{\bullet-}$  as substrate is further described at this point. The superoxide reductase (SOR, EC 1.15.1.2) is an iron-containing enzyme in anaerobic bacteria and archaea which catalyses the reduction rather than the dismutation of superoxide, i.e.  $O_2^{\bullet-} + 2 H^+ + e^- \rightarrow H_2O_2$  (Adams *et al.*, 2002; Kurtz & Coulter, 2002; Abreu *et al.*, 2002). This

---

reaction may also take place with the help of an iron-sulfur redox protein called rubredoxin (Rd) which serves as electron-donor:  $O_2^{\bullet-} + 2H^+ + Rd_{red} \rightarrow H_2O_2 + Rd_{ox}$ . Superoxide reductase appears to play in anaerobes the oxygen detoxifying role that is attributed to superoxide dismutases in aerobes. In the oxidized enzyme state, the mononuclear ferric active site shows an octahedral coordination geometry with four histidine imidazolate ligands in the equatorial plane and a cysteinate and a glutamate ligand in axial positions. The latter is lost in the reduced (ferrous) state (see crystal structures with PDB accession codes 1DQI and 1DQK).

Peroxide is a cytotoxic oxidant as well. Two enzyme families, catalases and peroxidases, eliminate it from the cells. Catalases dismute  $2H_2O_2$  to  $O_2 + 2H_2O$  while peroxidases utilize a variety of reductants  $RH_2$  to reduce  $H_2O_2$  to  $2H_2O + R$  (Fridovich, 1998a).

Some targets of direct oxygen metabolites mentioned above will become secondary reactive species and, in a chain reaction like mechanism, the initial damage can be amplified considerably. Another level of defence is thus to diminish damage by preventing the initiation or propagation of chain reactions. This task is performed by antioxidants which generate insufficiently reactive species from those of the chain reaction (Fridovich, 1989). As prominent examples may serve  $\alpha$ -tocopherol (vitamin E) and ascorbic acid (vitamin C).

The last stage of defence consists of repair of already occurred damage. The affected targets may either be replaced by newly synthesized molecules as for lipids and proteins or may be corrected by specific substitution of damaged parts as for hydroxylated bases in DNA.

The role of superoxide in biology and medicine is still the topic of intense research (Halliwell & Gutteridge, 1999; McCord, 2000). Physiological consequences of an increased  $O_2^{\bullet-}$  concentration include strongly elevated rate of spontaneous mutagenesis, lysis of plasma membranes and inactivation of a number of important enzymes. Among pathologies to which oxidative stress is related are inflammatory and neurologic diseases as well as reperfusion injuries. The fatal motoneuron degenerative disease familial amyotrophic lateral sclerosis (FALS) is related to mutations in the cytoplasmic Cu,ZnSOD (Deng *et al.*, 1993). In addition, life span and the process of ageing in general is shown to be connected to oxidative stress, as even low-level oxidative damage takes effect constantly throughout an organism's life (Finkel & Holbrook, 2000).

Considering the oxidative damage of important biomolecules caused by  $O_2^{\bullet-}$ , cells are expected to reduce the amount of  $O_2^{\bullet-}$  to its minimum level possible. However, pur-

---

poseful production of  $O_2^{\bullet-}$  is observed in some cases. A membrane-bound NADPH oxidase generates  $O_2^{\bullet-}$  during the “respiratory burst” where superoxide acts together with its reactive by-products as weapon against microbes inside phagocytic cells. In other cell types, the task of released  $O_2^{\bullet-}$  is not yet understood. Another role of superoxide that is not based on its damaging action has been proposed. Superoxide and other oxidants as well as antioxidants are incorporated in regulation of gene expression via careful tuning of the cell’s redox state. Reactive oxygen species are thought to function as redox-signals to the genetic machinery of the cell (see (McCord, 2000) and references therein).

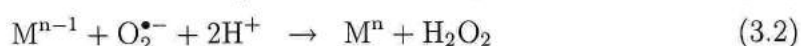
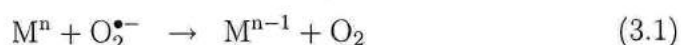
# Chapter 3

## Superoxide Dismutases

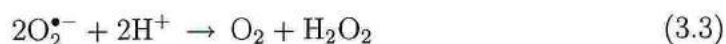
### 3.1 General Features

The superoxide dismutase (SODs, EC 1.15.1.1) is an enzyme dedicated to the dismutation of the superoxide radical anion  $O_2^{\bullet-}$ . As described in the previous chapter, SODs play an important role in managing oxidative stress both in prokaryotic and eukaryotic cells. In 1969, the first member of this enzyme family, Cu,ZnSOD (McCord & Fridovich, 1969), has been shown by Joe M. McCord and Irwin Fridovich to have SOD activity (Fridovich, 2001). Since then, a large amount of information has been gathered together about superoxide dismutases of which the most important results are summarised here.

The general dismutation reaction is written as a two-step reaction for which SODs use metal centres (M):



This yields the overall dismutation reaction



It was shown that the metal ion Cu(II) alone is able to dismute superoxide, however, cells cannot rely solely on free Cu(II) since it is cytotoxic at relevant concentrations. Also Mn(II) can mimic the SOD function and the fact that it is much less efficient is compensated in *Lactobacillus plantarum* by its large concentration of about 25 mM (Fridovich, 1998a). For therapeutic purposes, non-protein mimics are of great interest due to practical drawbacks associated with enzyme therapies (Salvemini *et al.*, 1999). In addition, spontaneous dismutation is possible (Fridovich, 1998a), e.g. reaction (3.3) which occurs in a direct encounter of two superoxide anions at a rate smaller than  $2 \cdot 10^5 \text{ L mol}^{-1} \text{ s}^{-1}$  at pH 7.

SOD shortens the lifetime of  $\text{O}_2^{\bullet-}$  enormously. Assuming a SOD concentration of  $10^{-5} \text{ mol L}^{-1}$  and a  $\text{O}_2^{\bullet-}$  concentration of  $10^{-10} \text{ mol L}^{-1}$ , the encounter of a superoxide anion with a SOD molecule is  $10^5$  times more likely than the spontaneous dismutation just mentioned. The catalytic rate constant of SOD is about  $2 \cdot 10^9 \text{ L mol}^{-1} \text{ s}^{-1}$ , i.e.  $10^4$  times higher than the uncatalysed reaction, resulting in an effective shortening of superoxide lifetime in a cell by the factor of  $10^9$  (Fridovich, 1998a).

From the above reactions it is evident that SODs use an electron obtained from superoxide in the first encounter to reduce another  $\text{O}_2^{\bullet-}$  in the subsequent encounter. The fact that the metal centre is first reduced and then reoxidized by  $\text{O}_2^{\bullet-}$  imposes constraints on the redox potential of the pair ( $\text{M}^n, \text{M}^{n-1}$ ); in order to supply equal driving forces for the two steps, it should lie midway between the redox potentials of the pairs ( $\text{O}_2^{\bullet-}, \text{O}_2$ ) and ( $\text{O}_2^{\bullet-}, \text{H}_2\text{O}_2$ ), i.e. between  $-0.16 \text{ V}$  and  $+0.89 \text{ V}$  versus the Normal Hydrogen Electrode (NHE) (Holm *et al.*, 1996). Once the SOD is in its reduced form after the first step, autoxidation of the metal centre has to be avoided for the complete reaction cycle to take place. This feature together with the need for a relatively low redox potential of about  $0.3 \text{ V}$  represent requirements for a given metal centre in terms of ligation type and geometry.

Nature has invented more than one type of SOD to fulfill the above requirements of the dismutation reaction. But before mentioning these various SODs in the next section, it is interesting to note that  $\text{O}_2^{\bullet-}$  is not the only substrate of SODs. The nitroxyl-ion has been revealed as substrate for SOD (Liochev & Fridovich, 2002).  $\text{NO}^-$  can be oxidized to  $\text{NO}$  when  $\text{O}_2^{\bullet-}$  is present to bring the enzyme back to its resting state. Even a peroxidase function of SOD has been observed *in vitro* (Liochev & Fridovich, 2001), however, its *in vivo* significance has still to be verified. It is evident from the single steps of the dismutation reaction that whenever a reductant other than  $\text{O}_2^{\bullet-}$  reduces the metal centre (reaction 3.1), the resulting SOD may still be able to carry out reaction 3.2, i.e. to function as a superoxide reductase. Vice versa, SOD may act as a superoxide oxidase if the metal centre is reoxidized by an oxidant other than  $\text{O}_2^{\bullet-}$ . This has indeed been observed *in vitro* (Liochev & Fridovich, 2000) and is believed to have *in vivo* relevance as well. The SOD function varies with the reducing character of the medium in which the enzyme exists and may also depend on the organism's ability to cope with the divers products of the oxidase function (only  $\text{O}_2$ ), the reductase function (only  $\text{H}_2\text{O}_2$ ) and the dismutase function (both  $\text{O}_2$  and  $\text{H}_2\text{O}_2$ ). Therefore, each organism may correspondingly rely more on either of these functions (Auchère & Rusnak, 2002).

## 3.2 SOD Classes and their Distribution

Superoxide dismutases are generally classified according to the metal species which acts as redox active centre in these enzymes. Until recently three different metal species have been found. Copper- and zinc-containing SOD (Cu,ZnSOD), with copper as the catalytically active metal, manganese-containing SOD (MnSOD), and iron-containing SOD (FeSOD) (Fridovich, 1995 and references therein). More recently two new superoxide dismutases have been purified from a variety of *Streptomyces* species (Youn *et al.*, 1996a+b, Kim *et al.*, 1996). These are iron- and zinc-containing SOD (Fe,ZnSOD) and nickel-containing SOD (NiSOD), the latter introducing a novel class of SODs regarding the metal type.

Another classification scheme, employing the three-dimensional structures of these enzymes as criterion, yields only two classes since MnSOD and FeSOD show high structural similarity and can thus be grouped together (see section 3.3).

These enzymes were isolated from prokaryotes as well as from eukaryotes and may coexist, even though in some cases in different cell compartments, inside the same organism (Halliwell & Gutteridge, 1999). *E. coli* for example contains all of the above SODs, with Cu,ZnSOD being periplasmic. Mammals may contain a cytosolic and an extracellular Cu,ZnSOD and a MnSOD in the mitochondrial matrix but they lack the FeSOD. Cu,ZnSOD can generally be found in the cytosol of eukaryotic cells, in the periplasm of gram-negative bacteria and the plastids of plants (Fridovich, 1998a). MnSOD is very widespread in bacteria, plants and animals as Cu,ZnSOD but regarding eukaryotic cells, exists mainly in the mitochondria. The similarity of mitochondrial MnSOD to its prokaryotic relative can be regarded as the result of the endosymbiotic origin of mitochondria. FeSOD is encountered in bacteria, primitive eukaryotes and plants but not in animals.

## 3.3 Structural Description of Cu,ZnSOD, MnSOD & FeSOD

The oligomerization states of Cu,ZnSODs, MnSODs and FeSOD ranges from monomers to tetramers with the exception of trimers. Cytosolic Cu,ZnSOD was found in mammals as homodimers and in the extracellular space as homotetramers; prokaryotic Cu,ZnSODs are either monomeric or dimeric, e.g. *E. coli* contains a monomeric Cu,ZnSOD in its periplasm and *Photobacterium leiognathi* a dimeric Cu,ZnSOD. MnSOD exists in homotetrameric form in the eukaryotic mitochondria and in homodimeric form in the bacterial cytosol. FeSOD forms homodimers or homotetramers as MnSOD.

The above SODs can be grouped in two structural classes; one comprises the Cu,ZnSODs and the other both Mn- and FeSODs. The Fe,ZnSOD found in *S. coelicolor* and *S. griseus* is homologous to the FeSODs.

The first crystal structure of a SOD was determined by Tainer *et al.* in 1982 (see PDB entry 2SOD of the bovine erythrocyte Cu,ZnSOD). The subunit structure of Cu,ZnSOD is composed of eight antiparallel  $\beta$ -strands in Greek key topology and hosts one Cu- and one Zn-ion (Fig. 3.1). The catalytically active Cu(II) is coordinated by the imidazolates of four histidine residues, one of which bridges this ion to the Zn-ion, and a water molecule which is located in the apical position of the distorted square pyramidal ligand environment (Fig. 3.2). Two other histidines and the carboxyl group of an aspartate coordinate the Zn-ion which is believed to play a structurally stabilizing role since it is not needed for catalysis. During the catalytic cycle, the Cu-ion switches between the oxidation states II (resting enzyme) and I (reduced form). The active site is accessible via a channel of cone-like shape. The bottom of the channel below which the Cu-ion is located has a diameter of about 4 Å admitting only small anions or water. A lysine lines the channel close to the enzyme's surface and an arginine (Arg141 in Fig. 3.2) is located close to the Cu-ion, such that the overall charge at the active site is strongly positive. Apart from contributing to electrostatic attraction of substrate to the Cu-ion, this arginine positions the substrate relative to the Cu and (together with a threonine) takes part in formation of the channel's dead end (Bordo *et al.*, 2001).

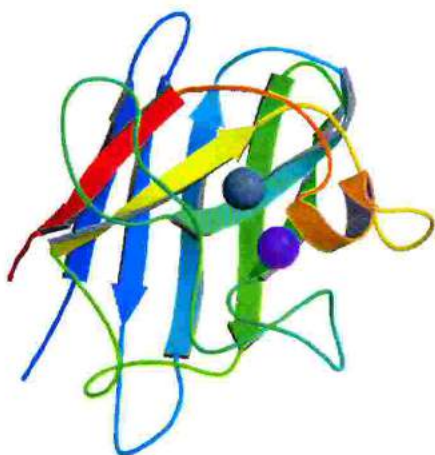


Figure 3.1: Ribbon representation of a subunit of human dimeric Cu,ZnSOD (PDB entry 1SPD, grey sphere: Cu-ion, purple sphere: Zn-ion).

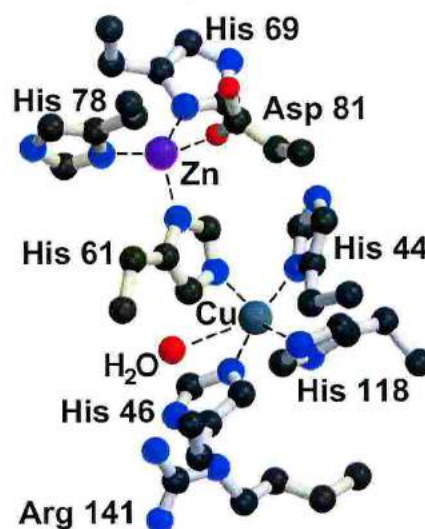


Figure 3.2: Ball-and-stick representation of the active site of bovine Cu,ZnSOD (PDB entry 2SOD).

MnSOD as well as FeSOD show mainly  $\alpha$ -helices and few  $\beta$ -strands (Fig. 3.3). The active site metal ion is bound in a trigonal bipyramidal geometry by three equatorial ligands (two histidine imidazoles and an aspartate) and two axial ligands (another histidine and a hydroxyl ion or water molecule, see Fig. 3.4 and (Maliekal *et al.*, 2002)). Despite the high structural homology between MnSOD and FeSOD, some enzymes are found in an active form only if the respective metal ion is present at the active site. The structural basis for this specificity has not yet been fully revealed. Some others, however, termed 'cambialistic SODs', are active with either a Mn- or Fe-ion at the metal centre. Residues which line up the substrate access channel to the metal site are found important for the activity of the enzyme although they are outside the first coordination shell of the metal ion. Their functional role lies in fine tuning important chemical parameters rather than in conformational aspects (Edwards *et al.*, 2001).

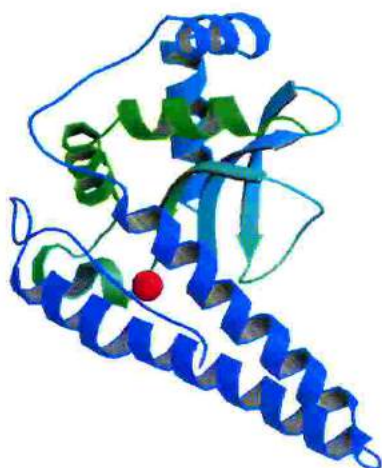


Figure 3.3: Ribbon representation of a subunit of a tetrameric MnSOD from *Propionibacterium shermanii* (PDB entry 1AR4, red sphere: Mn-ion).

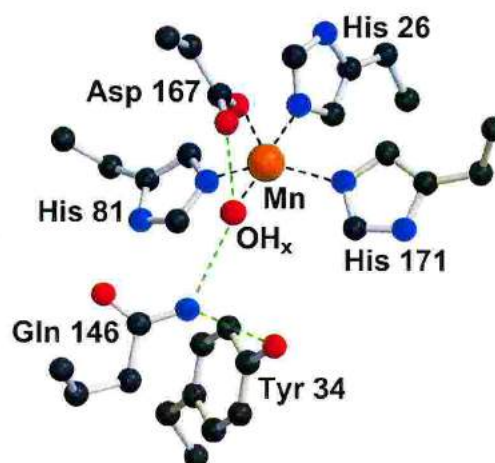


Figure 3.4: Ball-and-Stick representation of the active site of *E. coli* MnSOD (PDB entry 1D5N). Green dashed lines: hydrogen-bond interactions.

### 3.4 Biochemical Description of Cu,ZnSOD, MnSOD & FeSOD

#### Kinetics.

SODs have been found to catalyse the disproportionation of  $O_2^{\bullet-}$  at almost diffusion limited rate. The second-order catalytic rate constant for Cu,ZnSOD has been reported as  $2.3 \cdot 10^9 \text{ M}^{-1}\text{s}^{-1}$  for the dimeric enzyme at pH 7.0 and room temperature

(Klug *et al.*, 1972).  $O_2^{\bullet-}$  binding to the enzyme corresponds to a second-order process while the conversion of  $O_2^{\bullet-}$  to product was found to be a pseudo-first-order process (Fee & Bull, 1986). The mentioned rate constant represents the observed pseudo-first-order rate constant divided by the enzyme concentration and was determined by direct activity assays using pulse radiolysis (see appendix C.2).

The pH- and ionic strength dependence of the catalytic rate will be compared to that of NiSOD in section 4.3, see Figures 4.1 and 4.3. However, it is worth mentioning already here that the strong dependence of  $k_{cat}$  on the solution's ionic strength has been most important especially for Cu,ZnSOD to explain the high catalytic rate of the enzyme. As the active site represents only about 1% of the enzyme's surface, most of the random collisions would not allow the approach of substrate to the metal centre and thus, a rate constant close to the diffusion limit would not be feasible (Fridovich, 1998a). Competition of the substrate and anions from the solvent which screen the metal ion at the bottom of the positively charged channel can account for the observed high ionic strength dependence and implies that the enzyme uses electrostatic attraction to guide the substrate to the active site (Getzoff *et al.*, 1983).

### Inhibition.

Small anionic molecules are able to competitively inhibit the described SODs primarily in their high valence form. Differences in the inhibition efficiency of various small anions were initially used as criterion to distinguish between the SOD species (Halliwell & Gutteridge, 1999). Cu,ZnSOD is sensitive to cyanide ( $CN^-$ ) and to peroxide. The  $CN^-$ -concentration required for a 50 % loss of human cytosolic Cu,ZnSOD activity is 0.2 mM compared to 22 mM azide ( $N_3^-$ ), showing that azide is less efficient (Inarrea, 2002). Also fluoride ( $F^-$ ) binds to the Cu(II)-ion while iodide ( $I^-$ ) cannot access the Cu(II) due to its too large diameter with respect to the bottom of the substrate channel. MnSOD is instead more sensitive to azide but almost insensitive to cyanide. Also FeSOD is effectively inhibited by azide but not by cyanide, however, it is much more sensitive to peroxide than MnSOD. The inhibition constant of FeSOD regarding fluoride is 33 mM.

### Catalytic Mechanism.

The catalytic mechanism for Cu,ZnSOD was addressed by studies on structures of wild type enzyme, mutants, inhibitor-bound and  $O_2$  pressurized enzyme from eukaryotic organisms (including human, bovine, yeast) and prokaryotes (including *E. coli*, *Photobacterium leiognathi*). The structural and functional informations led to the formulation of a reaction scheme which is recollected in (Bordo *et al.*, 2001). It states that  $O_2^{\bullet-}$  binds directly to the Cu(II) in the first reaction step (inner sphere electron transfer to the metal) but remains about 3 Å from the Cu(I) when it accepts

the electron in the second reaction step, i.e. in an outer sphere electron transfer. The coordination number of the Cu-ion changes upon reduction from five to three, losing the water ligand and the Cu and Zn bridging imidazole which becomes protonated. Simultaneously to the electron transfer in the second reaction step, one proton is thought to be delivered to the substrate from a solvent water and another from N $\epsilon$  of the imidazole that bridges Cu and Zn in the resting enzyme state. The Cu-ion then moves towards N $\epsilon$  of this imidazolate to re-establish the previously broken ligation. A relay of water molecules between the solvent and the metal centre is present to supply protons needed for the formation of peroxide. Proton transfer pathways along solvent water molecules were inferred with high accuracy from the structure of reduced bovine Cu,ZnSOD which was refined to 1.15 Å resolution (Hough & Hasnain, 2003).

## Part II

# The Ni-containing Superoxide Dismutase from *Streptomyces seoulensis*

## Chapter 4

# Introduction to Ni-containing Superoxide Dismutases

### 4.1 Distribution of NiSOD

NiSOD, initially known in *Streptomyces* genera only, was purified and characterized in several species of *Streptomyces* (aerobic filamentous Gram-positive soil bacteria) including *S. seoulensis*, *S. coelicolor* and *S. griseus*. The amino acid identity between mature NiSOD from *S. seoulensis* and *S. coelicolor* amounts to 89%. Immunological cross-reactivity tests with antiserum against NiSOD and tests of SOD induction in the presence of Ni indicated that NiSOD exists universally in the *Streptomyces* species (Lee *et al.*, 2002; Leclere *et al.*, 1999). In addition, it was found that NiSOD is not confined to the *Streptomyces* genus, but exists in several Actinomycetes such as *Micromonospora rosaria*, *Microtetraspora glauca* and *Kitasatospora griseola* (Wuerger *et al.*, 2003). These SODs show UV-visible and EPR spectra similar to those of NiSOD from *S. seoulensis*. The amino terminal sequences are in almost perfect homology with those of *S. coelicolor* NiSOD.

NiSOD is predicted to occur in some cyanobacteria as will be discussed in detail in section 7.8. This prediction is based on amino acid similarity in most regions of the NiSOD subunit that are involved in defining the subunit fold and active site structure.

### 4.2 Expression of NiSOD

Conditions for culturing *Streptomyces* species are described in (Lee *et al.*, 2002) and references therein. Addition of 10-100  $\mu\text{M}$   $\text{NiCl}_2$  to the growth medium induces the NiSOD expression more than tenfold (Kim *et al.*, 1996 and 1998). The underlying

molecular processes of induction by Ni(II) is not yet fully understood and the transcriptional regulator not yet identified. Purification was performed as described in (Lee *et al.*, 2002) and references therein.

Post-translational cleavage of 14 N-terminal amino acids was indicated by comparing the deduced amino acid sequence from NiSOD's gene *sodN* with the N-terminal amino acids of purified active NiSOD determined by Edman degradation (Kim *et al.*, 1998, Choudhury *et al.*, 1999). Ni(II) was found to play a regulatory, or at least a facilitating role in proteolytic cleavage (Kim *et al.*, 1998). Production of active NiSOD in *E. coli* proved to be inefficient despite the high level of overexpression of precleaved NiSOD and the presence of added Ni(II). This is indicative of a lack of accessory proteins in *E. coli* which are required for post-translational processing. Identification and precise function of such proteins in NiSOD folding, N-terminal cleavage and/or Ni-ion incorporation are still the subject of investigations.

The amino acid sequence of NiSOD from *S. seoulensis*, including at position -14 to -1 the residues which are cleaved off during post-translational processing to obtain the mature form of the enzyme is as follows (Choudhury *et al.*, 1999):

```

-14  MLSRLFAPKV  KVSA                               -1
      1  HCDLPCGVYD PAQARIEAES VKAIQEKMAA NDDLHFQIRA TVIKEQRAEL AKHHLVDLWS  60
      61  DYFKPPHFES YPELHTLVNE AVKALSAAKA STDPATGQKA LDYIAQIDKI FWETKKA    117

```

*S. coelicolor* and *S. griseus* contain besides NiSOD a second SOD, the iron- and zinc-containing SOD, that had not been isolated from other sources before (Youn *et al.*, 1996a, Kim *et al.*, 1996 and 1998). Competitive expression of NiSOD and Fe,ZnSOD is observed in these species. The relative amounts of NiSOD and Fe,ZnSOD that are expressed in these two *Streptomyces* species depends on the concentration of Ni-ions in the growth medium, but does not change with varying concentrations of other ions of Fe, Zn, Mn or Cu. Increasing NiSOD and decreasing Fe,ZnSOD expression levels are found upon increasing the medium's Ni(II) concentration. The Ni-dependent regulation of expression of both NiSOD and Fe,ZnSOD results from modulation in transcription of the respective gene (*sodN* and *sodF*) which may be achieved via Ni-sensitive DNA-binding proteins (see (Chung *et al.*, 1999) and (Carrington *et al.*, 2003)).

In conclusion, Ni-ions play various different roles in producing active NiSOD:

1. modulation of the transcription of the NiSOD gene *sodN*,
2. regulation of post-translational proteolytic processing,
3. acting as catalytic cofactor.

## 4.3 Biochemical and Spectroscopic Studies on NiSOD

Biochemical and spectroscopic studies on NiSOD were carried out in the laboratory of Prof. Kang at the Seoul National University, except for kinetics studies using radiolysis and X-ray absorption spectroscopy, which were carried out at the Brookhaven National Laboratory (USA) in a collaboration of Prof. Kang.

**Oligomeric State.** The molecular mass of a subunit of NiSOD was initially estimated by denaturing polyacrylamide gel electrophoresis (SDS-PAGE) to be 13.4 kDa (Youn *et al.*, 1996a). It was subsequently determined more accurately by mass spectrometry using Matrix Assisted Laser Desorption Ionisation - Time of Flight (MALDI-TOF) to be 13.2 kDa which is close to the mass calculated from the amino acid composition of a subunit, 13 188 Da. The mass of the native enzyme has been originally estimated as about 60 kDa by size exclusion chromatography (gel filtration) which led to the conclusion that NiSOD contains four identical subunits. Equilibrium sedimentation, however, suggested subsequently that NiSOD is a homohexamer based on the re-determination of the native enzyme mass as 84.9 kDa (Wuerges *et al.*, 2003). This was confirmed by heterologous expression tests (Wuerges *et al.*, 2003) and for the crystalline state by crystallographic analysis (Wuerges *et al.*, 2002).

**Metal Contents.** The notion that nickel is present in this novel SOD came initially from the determination of metal contents by atomic absorption spectroscopy and the similarity of Electron Paramagnetic Resonance (EPR) spectra to those of Ni-containing short peptides and [NiFe]-hydrogenase (Youn *et al.*, 1996a + b). The observed nickel content suggested one Ni-ion per enzyme subunit. Additionally, the apo-enzyme showed only 7% of SOD activity relative to the native enzyme, showing that nickel is involved in enzymatic function (Youn *et al.*, 1996b). The oxidation state of the Ni-ion in resting NiSOD was determined by EPR spectroscopy to be +3 as described at the end of this section.

**Kinetics.** Kinetic studies on NiSOD were performed both by direct activity assay using pulse radiolysis (Choudhury *et al.*, 1999) and indirect assays (Youn *et al.*, 1996a + b, Kim *et al.*, 1996, Lee *et al.*, 2002). Appendix C.2 contains a description of assay methods for SOD activity.

The calculated second-order catalytic rate constant was reported as  $k_{cat} = 1.3 \cdot 10^9 \text{ M}^{-1} \text{ s}^{-1}$  per Ni-centre (Choudhury *et al.*, 1999). It represents the observed rate constant in  $[\text{s}^{-1}]$  divided by the respective metal concentration in  $[\text{M}]$  (not by the enzyme

concentration, thus allowing the comparison between SODs with different number of active sites per multimeric enzyme). This value is very close to what has been measured for Cu,ZnSOD under the same conditions ( $1.2 \cdot 10^9 \text{ M}^{-1}\text{s}^{-1}$  per Cu-centre), thus NiSOD's catalytic efficiency is on the same high level as that of Cu,ZnSOD. The pH-dependence of the catalytic rate constant has been studied by direct assaying the activity in the pH-range 6 to 11 (Choudhury *et al.*, 1999). The result shows a relatively pH-independent rate constant in the pH-range 6-8 and a sharp decrease of activity above pH = 8 (Fig. 4.1). The enzyme stability, determined as enzyme activity assayed by indirect methods, is pH-independent in the range  $\approx 4 - 8$  and falls off rapidly outside this range (Youn *et al.*, 1996b), see Fig. 4.2. The enzyme proved considerably thermostable up to 70 °C, a feature that has been reported also for many other SODs (Youn *et al.*, 1996b).

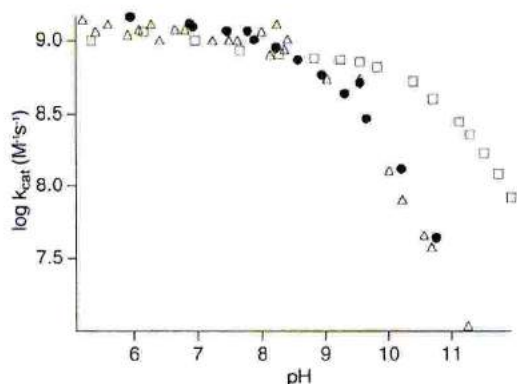


Figure 4.1: pH-dependence of  $k_{cat}$  for NiSOD as determined by pulse radiolysis. NiSOD (circles), Cu,ZnSOD (squares) and MnSOD (triangles). Taken from (Choudhury *et al.*, 1999).

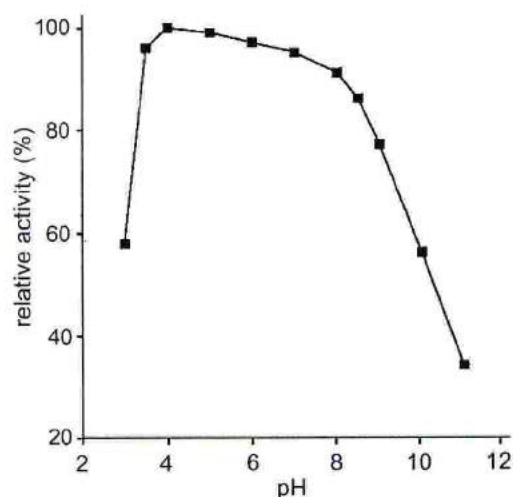


Figure 4.2: pH-stability of NiSOD as determined by assaying activity through indirect methods. Taken from (Youn *et al.*, 1996b).

The ionic strength dependence of the catalytic rate constant was investigated at pH 7.0 using various concentrations of  $\text{NaClO}_4$  and pulse radiolysis and was compared to that of bovine Cu,ZnSOD and *E. coli* MnSOD (Choudhury *et al.*, 1999). As is evident from Fig. 4.3, the effect of screening the positive charge of the metal ion by negatively charged ions in solution is strongest for MnSOD and smallest for NiSOD. This is interpreted with regard to the influence of electrostatic attraction of the anionic substrate  $\text{O}_2^{\bullet -}$  to the active site of the enzyme. The finding that NiSOD exhibits only a small decrease in catalytic rate with increasing concentration of competing anions from the solution is taken as an indication that electrostatic guidance of the

substrate is not an important aspect of NiSOD's catalytic mechanism.

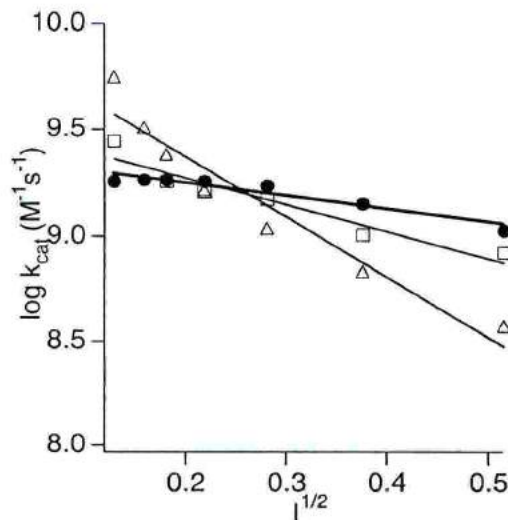


Figure 4.3: Dependence of NiSOD's catalytic rate constant  $k_{cat}$  on ionic strength  $I$  of the solution, here plotted as the logarithm of  $k_{cat}$  as a function of the square root of  $I$ . NiSOD (circles), Cu,ZnSOD (squares) and MnSOD (triangles). Taken from (Choudhury *et al.*, 1999).

**Inhibition Studies.** The pattern of SOD inhibition by small anions or peroxide has been described for Cu,ZnSOD, MnSOD and FeSOD in section 3.4. The pattern for NiSOD was characterized using direct and indirect activity assays (see (Choudhury *et al.*, 1999) and (Youn *et al.*, 1996b), respectively) and shown to differ from those of other SODs. NiSOD is much less inhibited by azide ( $N_3^-$ ) than Cu,ZnSOD: it needs 42 mM azide to obtain a 50% inhibition compared to 12.7 mM in case of bovine Cu,ZnSOD (Choudhury *et al.*, 1999). NiSOD is sensitive to cyanide and, although slightly less, to peroxide. At pH 7.4 and in micromolar concentration, NiSOD is inhibited to 100% by 10 mM  $CN^-$ , to 73.4% by 10 mM  $H_2O_2$  and to only 15% by 10 mM  $N_3^-$  (Youn *et al.*, 1996b).

**Spectroscopic Studies.** A brief introduction to the spectroscopic methods mentioned in this section can be found in appendix B. Visible/UV-spectroscopy was initially used to show that NiSOD is distinct from other SOD classes. An absorption maximum at 378 nm is due to the Ni-ion, i.e. absent in the spectrum of the apo-enzyme which features a peak at 280 nm (Fig. 4.4). The 378 nm peak is considered to result from charge transfer between the Ni and a ligand (Lee *et al.*, 2002).

EPR spectroscopy has been very useful for the characterization of the metal centre in

NiSOD. As mentioned above, EPR played an important role in identifying the metal type on which this enzyme's function relies. Moreover, the X-band EPR spectrum (Fig. 4.5 A) of resting NiSOD has features which gave insight into the oxidation state and the ligand environment of the metal ion. NiSOD shows a rhombic EPR signal with  $g$ -values of 2.302, 2.231 and 2.014 which vanishes upon reduction of NiSOD by dithionite, Fig. 4.5 B (Lee *et al.*, 2002).

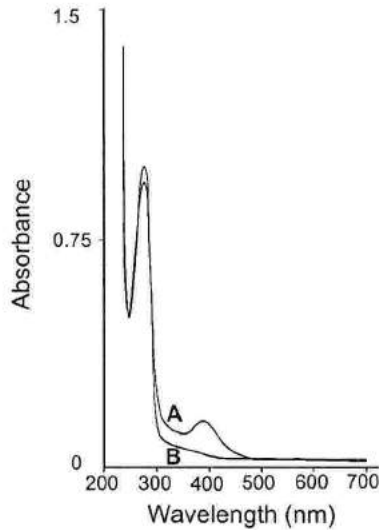


Figure 4.4: Visible/UV absorption spectrum of *Streptomyces seoulensis* NiSOD. Curve A: native SOD, curve B: apo-enzyme. Taken from (Youn *et al.*, 1996b).

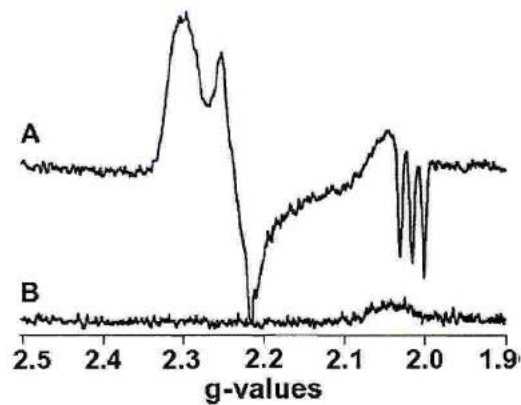


Figure 4.5: X-band EPR spectra at 100 K of *Streptomyces seoulensis* NiSOD in resting state (labelled A) and dithionite-reduced state (B). The enzyme is in a sodium phosphate buffer at pH 7.4. Taken from (Choudhury *et al.*, 1999).

Superhyperfine splitting into three lines is present at  $g = 2.01$  with a splitting constant of 2.5 mT. These features are observed also for Ni(III)-bound oligopeptides containing histidines and indicate that the superhyperfine splitting originates from a single nitrogen nucleus ( $^{14}\text{N}$ ) (Youn *et al.*, 1996b). Its spin  $I = 1$  results in the observed number of lines,  $2I + 1 = 3$ , and the position of this nitrogen-donor is suggested to be axial. To obtain information about the type and oxidation state of the metal, the spectrum is compared to those of various other metals in different oxidation states and ligand environments. The  $g$ -values point to a transition metal of spin  $S = \frac{1}{2}$  with its unpaired electron in a more than half filled shell, leaving as possible ions those with low-spin  $d^7$  or  $d^9$  states (Sa-Ouk Kang, personal communication). Among these ions, only Ni(I) ( $d^9$ ) and Ni(III) ( $d^7$ ) fitted well to the observed  $g$ -values and hyperfine interactions. Ni(III) is more likely since the signal is characteristic of an oxidized complex.

EPR spectra were also recorded from NiSOD samples under conditions in which crystals were grown in order to allow interpretation of EPR spectra in relation to the solved crystal structures. These spectra are discussed in section 7.3.1.

Sulfur ligands of nickel in NiSOD were first suggested by X-ray absorption spectroscopy (XAS, appendix B.3) which gave preliminary insight into the structure of the Ni-site (Choudhury *et al.*, 1999). The X-ray absorption near edge structure (XANES) analysis indicates a five- or six-coordinate Ni-ion in the resting enzyme and a four-coordinate Ni-ion with planar geometry in the dithionite-reduced enzyme, implying the loss of one or two ligands, presumably axial ligands, upon reduction (Fig. 4.6).

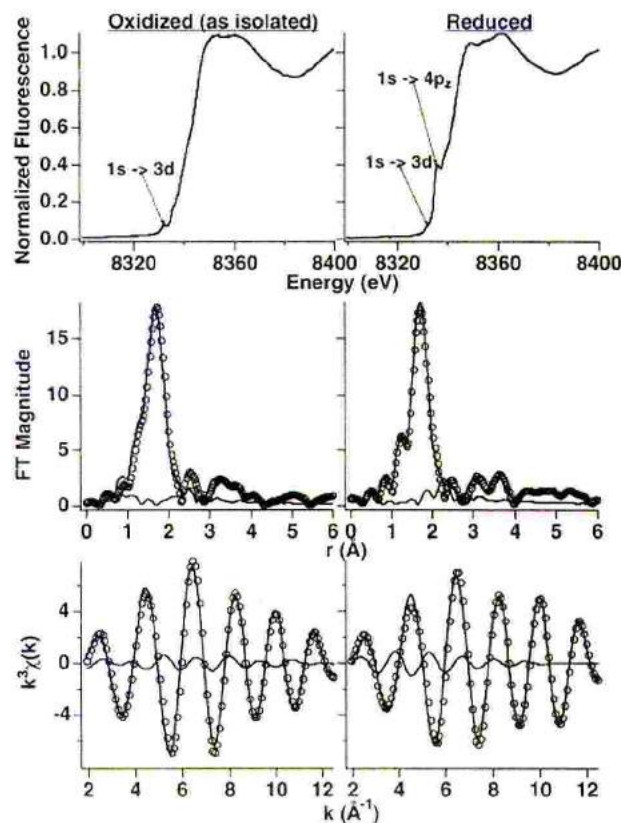


Figure 4.6: K-edge XANES spectrum of *Streptomyces seoulensis* NiSOD. The electronic transition  $1s \rightarrow 4p_z$  is indicative of a planar Ni-site and is present only in the spectrum of the reduced form of NiSOD. The area under the peak associated with a  $1s \rightarrow 3d$  electronic transition lies between values typical for five- and six-coordinate Ni-sites. Taken from (Choudhury *et al.*, 1999).

The decrease in coordination number is assumed to moderate the change in charge at the nickel which would result from reduction alone. The Ni K-edge extended x-ray

absorption fine structure (EXAFS) suggested a five-coordinate Ni-ion being ligated by three sulfur atoms and a nitrogen atom in both resting and reduced state and additionally a nitrogen or oxygen ligand in the resting enzyme. One of the N- (or O-) atoms is lost upon reduction. This was derived from the best curve-fit to the EXAFS spectra using a Ni-S distance of 2.158 Å and a Ni-N/O distance of 1.909 Å in case of resting NiSOD. The distances in case of reduced NiSOD were 2.154 Å and 1.87 Å, respectively. These shorter bonds obtained for the reduced enzyme state appear inconsistent with redox chemistry and were thought to result from the change in coordination geometry and number upon reduction. The EXAFS results were interpreted in two different ways, one assuming a mononuclear Ni-site in which all three S-ligands come from the same protein subunit and another being based on a dinuclear site with the involvement of two subunits (Choudhury *et al.*, 1999). Since there are only three sulfur-containing amino acids in the mature enzyme, two cysteines at position 2 and 6 and a methionine at position 28, these residues would necessarily be implicated in mononuclear coordination. Alternatively, the dinuclear coordination scheme could do with cysteine ligands from the N-terminal Cys-X-X-X-Cys motif alone if the Ni-ions are bridged by two of the four involved Cys residues. This arrangement would be similar to the [Ni,Fe] site in the hydrogenase of *Desulfovibrio gigas* which has already been structurally well characterized. The involvement of sulfur ligands in the coordination environment of NiSOD is a new feature among superoxide dismutases. However, this feature is common among redox-active Ni-containing enzymes (see chapter 9).

# Chapter 5

## Crystallization of NiSOD

This chapter describes the screening for crystallization conditions and the initial crystallographic characterization of crystals. In addition, preparations to obtain crystals of NiSOD in its reduced or inhibited state are described as well as heavy atom derivatization. Background information about the methods mentioned in this chapter can be found in the appendix 'Protein X-ray Crystallography', section A.1.

### 5.1 Screening for Crystallization Conditions

Purified protein was obtained from the laboratory of Prof. Sa-Ouk Kang. Size exclusion chromatography on a Superdex 200 column and ion-exchange chromatography on a mono-Q column (Amersham Pharmacia) were used in final steps of purification (Lee *et al.*, 2002). NiSOD was stored in 50 mM sodium phosphate, pH 7.4, and 30% glycerol at a concentration of 40 mg mL<sup>-1</sup>. Slow inactivation was observed under more dilute conditions (< 10 mg mL<sup>-1</sup>) at room temperature. Prior to use in crystallization trials, the protein was further purified on a Superdex 200 gel filtration column (Amersham) and, for the purpose of crystallization, the protein solution was thereby changed to 50 mM NaCl and 20 mM TRIS, pH 8.0. The protein concentration was adjusted to 10.6 mg mL<sup>-1</sup> as determined by  $OD_{\lambda=280nm}$ \*. The molar extinction coefficient used to calculate the protein concentration was derived theoretically from the primary sequence of a subunit as  $\epsilon_{280nm} = 16620 \text{ cm}^{-1}\text{M}^{-1}$ . The monodispersity of the sample was checked by dynamic light scattering, yielding a polydispersity factor of only 6%.

Crystallization trials were carried out according to the sparse matrix approach (Jancarik & Kim, 1991) by the hanging-drop vapour-diffusion method (appendix A.1) at a temperature of 277 K (4 °C) and 293 K (20 °C). Initial screens utilized

---

\*The Lambert-Beer law (see appendix B.1) assumes that the protein is denatured. A small deviation of the calculated concentration from the real value may thus occur.

premixed conditions (Crystal Screen I and II, Hampton Research) which were subsequently refined to improve crystal growth. NiSOD crystallizes in more than one form and, in the following, only those crystal forms are described which exhibited a quality suitable for collection of X-ray diffraction images. In all cases, about 1  $\mu\text{L}$  of protein solution was mixed with an equal amount of crystallization reagent and the 24 well Linbro-plates (VDX-plates from Hampton Research) were stored at 293 K (20°C). Photographs of the various crystal forms are compiled in (Fig. 5.1).

**Crystal form I.** The first crystals of NiSOD grew readily from a premixed crystallization reagent consisting of 2 M ammonium sulfate and 5% 2-propanol (Crystal Screen II, Hampton Research). The small amount of 2-propanol proved to be necessary for crystal growth. The pH of this condition is 5.25, i.e. below the protein's theoretical isoelectric point (pI) of 5.9. Plate-like crystals with approximate dimensions of  $0.21 \times 0.21 \times 0.05 \text{ mm}^3$  appeared after 1-2 weeks.

**Crystal form II.** A number of needle-shaped crystals per drop were obtained after 8-10 days from 1.85 M ammonium sulfate and 0.1 M sodium acetate, pH 5.25, showing an approximate length of 0.3 mm and diameter of 0.03 mm. A small improvement in needle diameter to 0.04 mm was obtained by adding a thin layer of oil mixture (silicon and paraffin oil purchased from Hampton Research, in 1:1 or 2:3 ratio) of 0.2-0.3 mL volume on top of the reservoir (Chayen, 1997). The purpose of the oil layer is to reduce the number of nuclei per drop by slowing down the equilibration process and thus allows growth of fewer but larger crystals. Macroseeding (Thaller *et al.*, 1981) these needle crystals to pre-equilibrated crystallization drops containing 1  $\mu\text{L}$  of 1.78 M ammonium sulfate, 0.1 M sodium acetate pH 5.25, and 1  $\mu\text{L}$  fresh protein solution was tried to increase the crystal size. No significant crystal growth could be observed, but instead a new crystal form III appeared after 5-6 weeks in the macroseeding drops, showing a different morphology and space group. The phenomenon of crystal growth from a seeded crystal that was obtained from different conditions in a different crystal form is called epitaxial jump (Stura, 1999).

**Crystal form III.** Rod like crystals with typical dimensions of approximately  $0.5 \times 0.2 \times 0.2 \text{ mm}^3$  were first obtained as byproduct of macroseeding form II crystals as described above. This way of growing form III crystals was reproducible, but more convenient growth conditions were found to be 1.85 M ammonium sulfate, 0.1 M sodium acetate, pH 5.25, and 10% glycerol from which crystals grew in 5-6 weeks.

**Crystal form IV.** Irregular shaped cubic-like crystals grew from conditions which are very similar to those of form II crystals, the only variation being the higher pH of 5.55 of the sodium acetate buffer. After two weeks a number of small crystals appeared which would not grow to a size larger than about  $(0.1 \text{ mm})^3$ .

**Crystal form V.** A crystal form that was obtained only below room temperature, at 277 K, showed irregular shaped big crystals with rugged surfaces. The reservoir conditions consisted of 18 % PEG 8000, 0.1 M sodium cacodylate, pH 6.1, and 0.2 M magnesium acetate.

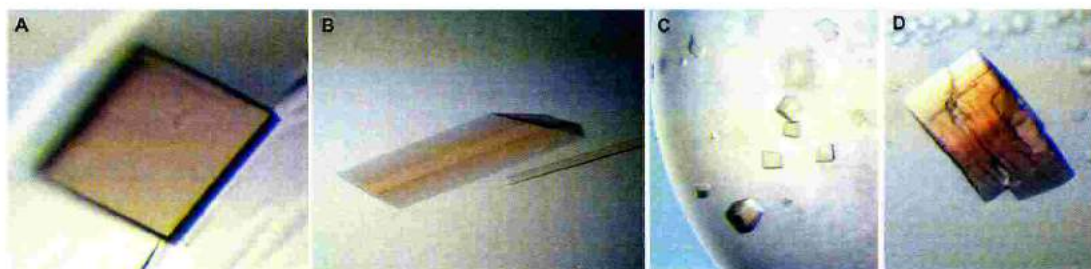


Figure 5.1: Photographs of NiSOD crystals. (A) Crystal form I with approximate dimensions of  $0.21 \times 0.21 \times 0.05 \text{ mm}^3$ . (B) Rod-like crystal form III obtained by epitaxial jump after macroseeding the small needle crystal (form II) in the drop shown here. (C) Crystal form IV with approximate dimensions of  $(0.05 \text{ mm})^3$ . (D) Crystal form V with approximate dimensions of  $(0.3 \text{ mm})^3$ .

## 5.2 Crystals of thiosulfate-reduced NiSOD

Thiosulfate ( $\text{S}_2\text{O}_3^{2-}$ ) was used as reducing agent to mimic the reduction of the metal centre upon the first encounter with the substrate  $\text{O}_2^{\bullet-}$ . Crystals of reduced NiSOD were obtained by soaking form I crystals of resting NiSOD in 2 M ammonium sulfate, 5% 2-propanol and 0.1 M sodium thiosulfate ( $\text{Na}_2\text{S}_2\text{O}_3$ ) for 24 hours before they were used for data collection. Upon soaking, the crystals lost rapidly and almost completely their characteristic yellow-brownish colour, indicating that the reduction of Ni(III) had taken place (see section 4.3 for UV/visible spectra on NiSOD). The reduction was checked further by an X-ray fluorescence experiment on a crystal before collection of diffraction data. A small shift to lower energy in the Ni K-edge absorption was observed with respect to the resting enzyme, in agreement with the formal transition of Ni(III) to Ni(II) (Choudhury *et al.*, 1999).

### 5.3 Crystals of inhibited NiSOD

Cyanide and azide ions are known to act as inhibitors of NiSOD (Youn *et al.*, 1996b) and therefore it was tried to obtain crystals of  $\text{CN}^-$ - and  $\text{N}_3^-$ -inhibited enzyme. Soaking of crystals in solutions containing the inhibitor and co-crystallization trials of NiSOD and inhibitor were carried out. A principle difference between aqueous solutions of cyanide ( $[\text{:C}\equiv\text{N:}]^-$ , derived from its salts like KCN or NaCN) and azide ( $[\text{:N}=\text{N}=\text{N:}]^-$  from  $\text{NaN}_3$ ) is the tendency of cyanide to form the acid HCN, with a  $\text{p}K_a$  of about 9.2, whereas azide mainly remains in its ionic form. Because  $\text{H-C}\equiv\text{N:}$  is such a weak acid and the unprotonated form is needed in the inhibition, a difficulty arises from the fact that the above crystal forms grow under acidic conditions ( $\text{pH} \approx 5$ ). Attempts to grow crystal form I at  $\text{pH} = 7$  or transfer crystals stepwise (Berisio *et al.*, 1999) to  $\text{pH} = 7$  were not successful.

The literature concerning NiSOD inhibition by cyanide and azide, section 4.3, suggests minimum values for the inhibitor concentrations to be used in soaking and co-crystallization trials. As these values refer to  $\text{pH} = 7.4$  and low protein concentration, an estimation is necessary as to how much the concentration of KCN should be increased with respect to the literature value in order to supply sufficient  $\text{CN}^-$  ions for NiSOD inhibition under the given crystallization conditions, i.e. low pH and high [NiSOD]. Using the acid-dissociation equilibrium constant for HCN and  $[\text{H}^+] = 10^{-5} \text{ mol L}^{-1}$ , it is

$$\frac{[\text{H}^+][\text{CN}^-]}{[\text{HCN}]} = K_A = 4 \cdot 10^{-10} \text{ mol L}^{-1},$$

$$\frac{[\text{CN}^-]}{[\text{HCN}]} = 4 \cdot 10^{-5} \text{ mol L}^{-1} \quad \text{at } \text{pH} = 5.$$

$[\text{CN}^-]$  should be at least (but better much higher) than [NiSOD] which gives as lower limit the condition, using  $[\text{NiSOD}] \approx \frac{10.6}{2} \text{ mg mL}^{-1} = 4 \cdot 10^{-4} \text{ M}$ ,

$$[\text{HCN}] = \frac{1}{4} \cdot 10^5 [\text{NiSOD}] = 10 \text{ M}.$$

This is not a practicable concentration, but already at  $\text{pH} = 7$ , this values decreases to 0.1 M.

To prepare crystals of inhibited NiSOD, original form I crystals were either soaked at concentrations of 50 mM  $\text{CN}^-$  or 150 mM  $\text{N}_3^-$  for up to one week or at concentrations of 200 mM  $\text{CN}^-$  or 800 mM  $\text{N}_3^-$  for few minutes. The higher the concentration the shorter the soaking time that was permitted in order to avoid crystal damage.

### 5.4 Xenon & Heavy Metal Derivatization

Crystal form I was used to prepare heavy atom derivatives. This section contains the technical aspects of NiSOD derivatization. Heavy metals bind specific sites

mainly on the protein's surface whereas the noble gases xenon and krypton interact with hydrophobic sites which often are buried in the protein's core. The purpose of derivatization is usually to label the protein with electron-rich atoms for use in solving the phase problem by the methods of Single- or Multiple Isomorphous Replacement (SIR or MIR) which may also make use of the anomalous scattering of these atoms (then called SIRAS or MIRAS). In the particular case of NiSOD, only the heavy metal derivatives aimed at this purpose. The xenon derivative instead was prepared after the phase problem had been solved. Rather than for providing phasing signal, xenon was employed for probing accessibility of sites inside the protein (to be discussed in section 7.5).

### **Xenon Derivatives**

Crystals of form I were transferred with a loop to a drop of cryoprotecting solution (2 M ammonium sulfate, 5% 2-propanol, 20% glycerol). Immediately after the transfer, the drop was covered with a layer of paraffin oil and the crystal was transferred to the pressurization cell. Paraffin oil helps to avoid the dehydration of the crystal and the formation of ammonium sulfate crystals in the cryoprotecting solution during the time interval in which the crystal is exposed to the xenon gas. The optimum derivatization procedure should maximise the amount of xenon in the crystal to obtain high occupancies of xenon binding sites in the protein and keep the damage of the crystal due to dehydration at a minimum. Therefore, a series of different gas pressures and pressurization times was tested ranging from 5 to 19 bar and from 1 to 5 minutes. At the end of pressurization, the crystal was transferred to liquid nitrogen (77 K) to prevent further dehydration and the desorption of xenon.

### **Heavy Metal Derivatives**

Solutions containing a heavy metal were prepared using the Hampton Research kit. These solutions consisted of the crystallization liquor for form I crystals (2 M ammonium sulfate, 5% 2-propanol) with a series of different final concentrations of metals (0.5 mM, 1 mM, 2 mM, 5 mM and 10 mM). Crystals were soaked in these solutions before data collection for a range of different times (12 to 48 hours for higher metal concentrations and up to 100 hours for lower metal concentrations) to find optimal soaking condition.

The choice of metal compounds depended on three points specific for the case of NiSOD crystals:

- Sufficient binding capability at low pH of 5.25.
- Compatibility with high concentration of ammonium sulfate.
- Not relying on Cys or Met residues as binding sites since these residues are

expected to be involved in Ni-coordination.

Metals that fulfill the above requirements and were thus used are the lanthanides Europium (in  $\text{EuCl}_3$ ), Lutetium (in  $\text{LuCl}_3$ ) and Gadolinium (in  $\text{GdCl}_3$ ).

In addition, another technique of inserting anomalous scatterers in crystals of NiSOD was attempted using halide-containing cryoprotecting solutions (Dauter *et al.*, 2000). Crystals were soaked shortly (5 to 60 seconds) in solutions containing NaBr or KI in high concentrations: 1 to 1.5 M of halides replaced an equal amount of ammonium sulfate in the cryo-solution mentioned above.

## 5.5 Preliminary Crystallographic Analysis

Table 5.1 compiles features of the various crystal forms describing crystallographic parameters of the crystals and their diffraction quality. The quality is expressed in terms of crystal mosaicity and the resolution (i.e. the smallest lattice spacing  $d_{min}$  in Bragg's law for which the corresponding diffraction spot was observable). Crystals in form I of reduced NiSOD were isomorphous to those of resting NiSOD. As can be concluded already from the estimated number of subunits per asymmetric unit, NiSOD appears to be hexameric also in the crystalline state.

Table 5.1: The NiSOD crystal forms

crystal form	I	II	III	IV	V
space group	$P2_12_12_1$	R3	$P2_12_12_1$	R3	$P2_1$
cell dimensions [ $\text{\AA}$ ]					
a	112.3	189.4	65.2	205.1	62.5
b	113.8	189.4	119.3	205.1	$124.1, \beta = 101.8^\circ$
c	128.6	159.9	121.0	315.0	101.2
mosaicity [ $^\circ$ ]	0.3-0.45	0.4-0.9	0.6-0.9	0.7-1	$\geq 1.0$
$d_{min}$ [ $\text{\AA}$ ]	1.6	2.8	1.68	3.6	6.3
$V_M$ [ $\text{\AA}^3\text{Da}^{-1}$ ] <sup>a</sup>	2.6	2.3	3.0	2.7	2.4
No. of subunits per AU <sup>b</sup>	12	18	6	36	12
Solvent content [%] <sup>a</sup>	51	46	57	53	48

<sup>a</sup>The Matthews-coefficient  $V_M$  (Matthews, 1968) and the solvent content in the unit cell were estimated using the molecular weight of a NiSOD subunit of 13.2 kDa and a molecular-density value of  $1.3 \text{ g cm}^{-3}$ .

<sup>b</sup>The number of subunits per asymmetric unit was chosen such that  $V_M$  ranges between 2-3.

The crystallization conditions for the crystal forms I-III described here are similar with respect to their chemical composition but gave rise to considerably differing

unit cell dimensions and numbers of molecules per asymmetric unit. Form I, along the crystallographic axes  $a$  and  $b$ , shows similar cell dimensions as form III along axes  $b$  and  $c$  whereas axis  $c$  is nearly twice as long as axis  $a$  of form III. The resultant reduction of the form I unit cell by half is accompanied by a reduction of the number of molecules per asymmetric unit from 12 to six as found in form III. Both crystal forms grew from ammonium sulfate as precipitant at similar molarity and at similar pH but differ in the type of organic additive: 2-propanol in the case of form I crystals and glycerol in the case of form III crystals. Glycerol may modify the hydration state of the protein (Sousa & Lafer, 1990), thus allowing the crystal contacts that are responsible for the rearrangement of molecules (with respect to form I) to result in the smaller unit cell.

# Chapter 6

## Determination of the NiSOD Structure

This chapter contains a description of all experimental and computational steps that led from the crystal to the final molecular model of NiSOD in its resting and reduced state. The reader is referred to appendix A.2 for an introduction to those techniques used in protein X-ray crystallography which are relevant to the present chapter.

### 6.1 X-ray Data Collection and Processing

Multiple-wavelength anomalous dispersion (MAD) data sets were collected at the Ni K-edge on crystals of forms I to III (see last chapter). All data collections were carried out at cryogenic temperature (100 K) to reduce radiation damage of the crystal, using cryoprotecting solutions that were prepared as the respective crystallization conditions with addition of 20% v/v glycerol. X-ray fluorescence spectra at the Ni K-edge (Fig. 6.1 A) were measured before each MAD data collection which consisted of a peak, inflection point and high energy remote data set. From the fluorescence spectra, anomalous scattering factors  $f'$  and  $f''$  were calculated with the program CHOOCH (Evans & Pettifer, 2001) in order to select suitable X-ray energy values for the data collection. Plots of  $f'$  and  $f''$  about the theoretical absorption edge energy of 8.333 keV show a broad dip in  $f'$  with a minimum of -7.7 electrons and a maximum  $f''$  of 4.3 electrons without white-line feature in both the oxidised state Ni(III) and the reduced state Ni(II) (Fig. 6.1 B). Theoretical values, following approximations developed by Cromer and Liberman, are -8.13 and 3.92 for  $f'_{min}$  and  $f''_{max}$ , respectively, as tabulated in (Merritt, 2001).

MAD data processing and reduction statistics are given in Table 6.1. The program DENZO (Otwinowski & Minor, 1997) and, for post-refinement of unit cell parameters, SCALEPACK (Otwinowski & Minor, 1997) were used as well as MOSFLM

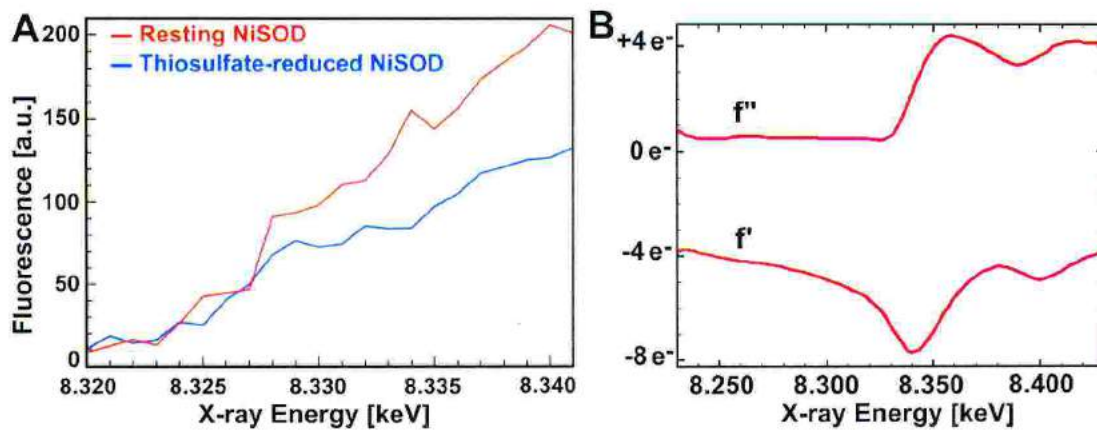


Figure 6.1: (A) Fluorescence Scan on resting and thiosulfate-reduced NiSOD at the Ni K-edge. (B) Experimentally derived anomalous scattering factors  $f'$  and  $f''$  (here for thiosulfate-reduced NiSOD) using the program CHOOCH (Evans & Pettifer, 2001).

(Leslie, 1992) for data processing and SCALA (CCP4, 1994) for data reduction, applying a MAD data specific scaling protocol. The R-factor for merging the three sub-sets of MAD data is 6.9% and 8.7% for form I and form III, respectively. Structure factor amplitudes were obtained from the intensities using TRUNCATE and further analysed by SCALEIT (CCP4, 1994).

The choice of space group for crystal forms I and III as  $P2_12_12_1$  was made on the basis of systematic absences of axial reflections with uneven indices and, noting the small difference in two of the unit cell parameters, by much worse merging statistics if treated as tetragonal. Similarly, space group R3 was chosen instead of R32 for crystal form II due to much better merging statistics. The latter crystal form was finally not used in structure determination and is therefore omitted from Table 6.1. Diffraction data to higher resolution than that of the respective MAD data were subsequently collected for both orthorhombic crystal form I (to 1.6 Å) and III (1.68 Å). Crystals of thiosulfate-reduced and xenon-pressurized NiSOD in crystal form I were prepared as described in sections 5.2 and 5.4, respectively. The crystals used for structure determination show cell dimensions (in Å) of 111.6, 113.7, 129.4 and 112.3, 113.7, 129.0, respectively and thus are isomorphous to untreated crystals. Processing and reduction statistics are compiled in Table 6.1 using the programs MOSFLM and SCALA.

All data were collected at synchrotron radiation sources on the following beamlines; MAD data of form I at BM14 and of form III at ID14-4 of the ESRF (Grenoble, France), high resolution data of form I at ID14-2 of the ESRF and of form III

at XRD1 of ELETTRA (Trieste, Italy) where also data of thiosulfate-reduced and xenon-derivatized NiSOD were collected.

Table 6.1: Data Processing and reduction statistics

MAD <sup>a</sup> data set	$\lambda^b$ (Å)	Resolution range (Å)	Completen. <sup>c</sup> (%)	$R_{ano}^d$ (%)	$\langle I/\sigma(I) \rangle$	$R_{sym}^e$ (%)	$M^f$	$R_{meas}^g$ (%)
Form I		31.1-2.2						
Pk	1.4827		99.7 (99.7)	4.2	11.9 (3.3)	5.6 (18.7)	4.7	7.1 (24.0)
Pi	1.4859		99.5 (99.5)	4.1	11.3 (3.4)	6.2 (22.4)	4.6	7.8 (28.8)
Re	1.2398		99.8 (98.7)	3.3	13.3 (5.5)	4.8 (13.6)	4.6	6.1 (17.4)
Form III		44.0-2.0						
Pk	1.4863		98.6 (98.6)	3.2	9.3 (2.2)	5.2 (21.7)	6.3	6.1 (25.9)
Pi	1.4756		98.5 (97.0)	2.9	6.7 (1.9)	6.2 (27.5)	6.3	7.3 (32.8)
Re	0.9392		99.2 (98.5)	2.4	6.3 (2.8)	7.5 (20.9)	8.0	8.6 (23.8)
High res. data set	$\lambda^b$ (Å)	Resolution range (Å)	Completen. <sup>h</sup> (%)	$R_{ano}^d$ (%)	$\langle I/\sigma(I) \rangle$	$R_{sym}^e$ (%)	$M^f$	$R_{meas}^g$ (%)
Form I	0.9326	42.6-1.6	98.9 (97.6)	-	13 (2.8)	8.0 (26.0)	3.7	10.3 (33)
Form III	1.0	34.3-1.68	99.1 (96.0)	-	11 (2.1)	4.3 (27.6)	6.6	4.6 (30.9)
Reduced data set	$\lambda^b$ (Å)	Resolution range (Å)	Completen. <sup>i</sup> (%)	$R_{ano}^d$ (%)	$\langle I/\sigma(I) \rangle$	$R_{sym}^e$ (%)	$M^f$	$R_{meas}^g$ (%)
Form I	1.127	40.2-2.1	99.6 (99.6)	-	10.3 (1.9)	5.1 (40.6)	3.8	5.8 (48.7)
Xenon data set	$\lambda^b$ (Å)	Resolution range (Å)	Completen. <sup>j</sup> (%)	$R_{ano}^d$ (%)	$\langle I/\sigma(I) \rangle$	$R_{sym}^e$ (%)	$M^f$	$R_{meas}^g$ (%)
Form I	1.45	50.6-2.13	99.9 (100)	3.9	6.1 (3.5)	8.5 (18.5)	7.9	9.9 (21.3)

<sup>a</sup>Pk, peak-energy; Pi, inflection-point; Re, remote-energy data.

<sup>b</sup> $\lambda$ , X-ray wavelength

<sup>c</sup>Values in parentheses are for outer resolution shells: form I, 2.32-2.2 Å; form III, 2.11-2.0 Å.

<sup>d</sup> $R_{ano} = \sum_{hkl} |I_+ - I_-| / \sum_{hkl} |I_+ + I_-|$ .

<sup>e</sup> $R_{sym} = \sum_{hkl} \sum_i |I_i - \langle I \rangle| / \sum_{hkl} \sum_i |I_i|$ , where  $I_i$  is the intensity of the  $i$ th measurement of a reflection  $hkl$  and  $\langle I \rangle$  is the average intensity of these  $i$  reflections.

<sup>f</sup> $M$ , multiplicity (redundancy)

<sup>g</sup> $R_{meas} = \sum_{hkl} \sqrt{\frac{N_{hkl}}{N_{hkl}-1}} \sum_i |I_i - \langle I \rangle| / \sum_{hkl} \sum_i |I_i|$ , a multiplicity-weighted  $R_{sym}$  with  $N_{hkl}$  as number of observations for reflection  $hkl$  (Diederichs & Karplus, 1997).

<sup>h</sup>Values in parentheses are for outer resolution shells: form I, 1.69-1.6 Å; form III, 1.76-1.68 Å.

<sup>i</sup>Values in parentheses are for the outer resolution shell: 2.21-2.1 Å.

<sup>j</sup>Values in parentheses are for the outer resolution shell: 2.25-2.13 Å.

## 6.2 Determination of Ni-sites

Native as well as anomalous and dispersive difference Patterson maps were calculated for the MAD data described in Table 6.1 using the program suite CNS (Brünger *et al.*, 1998). All maps calculated from data of form I crystals showed an outstanding

peak (20% of the origin peak height) at  $u = 0.05$ ,  $w = 0$  in the  $v = \frac{1}{2}$  Harker section (Fig. 6.2). This peak indicated the presence of purely translational non-crystallographic symmetry (NCS) in this crystal form. It is a special type of NCS and will be discussed in more detail in appendix A.3. Patterson maps of crystal form III (Fig. 6.3) did not show this feature.

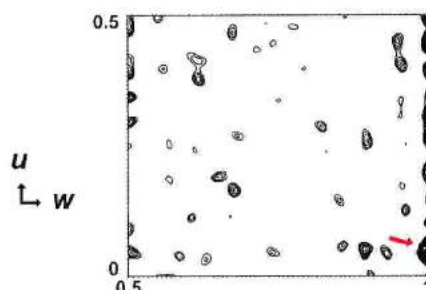


Figure 6.2: Native Patterson map in the  $(u, v = 0.5, w)$  Harker section of the  $P2_12_12_1$  'big cell' crystal form I (origin peak removed). The arrow indicates the high off-origin peak at  $(u, v, w) = (0.05, 0.5, 0)$  due to purely translational NCS which relates two hexamers in the asymmetric unit.

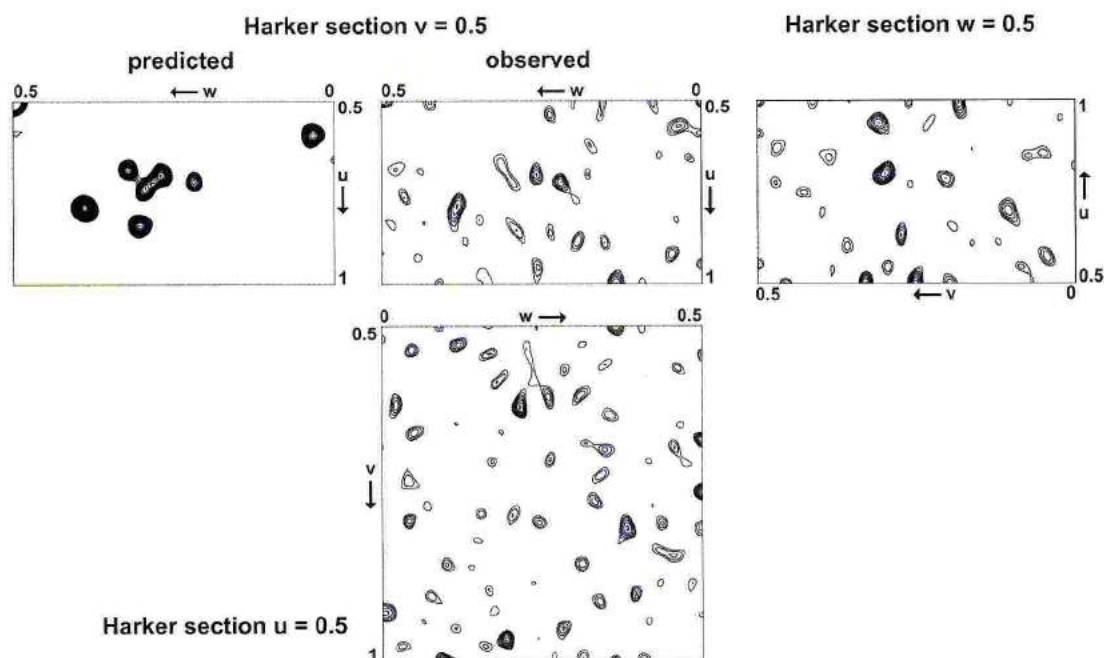


Figure 6.3: Anomalous difference Patterson maps of the  $P2_12_12_1$  'small cell' crystal form III collected at the  $f''$  maximum of the Ni K-edge (origin peak removed). A predicted Patterson map for the  $v = 0.5$  Harker section is shown, using Ni-sites of the refined 'small cell' model.

The heavy atom partial structure was solved using automated Patterson methods as implemented in the programs CNS and SOLVE (Terwilliger & Berendzen, 1999) with data in the resolution range 15 to 4 Å. Both programs found the same 12 sites per asymmetric unit and the correctness of these sites was confirmed by comparing experimental anomalous difference Patterson maps with those calculated from the found sites. An additional check was the inspection of anomalous difference Fourier and log-likelihood gradient maps in the graphics program O (Jones *et al.*, 1991) after MAD phasing with only nine sites chosen randomly among the 12 peaks. The three not included sites were clearly visible as the highest peaks in the log-likelihood gradient map. The Ni-sites are arranged in two identical spatially separated groups, each group forming a slightly distorted octahedron (Fig. 6.4). This confirms the notion based on estimated numbers of molecules per asymmetric unit by Matthews coefficient (Table 5.1) that NiSOD is a hexamer. Moreover, it is evident that NiSOD contains mononuclear Ni-centres, thus ruling out the alternative interpretation of EXAFS spectra regarding a possible dinuclear Ni-centre (section 4.3).

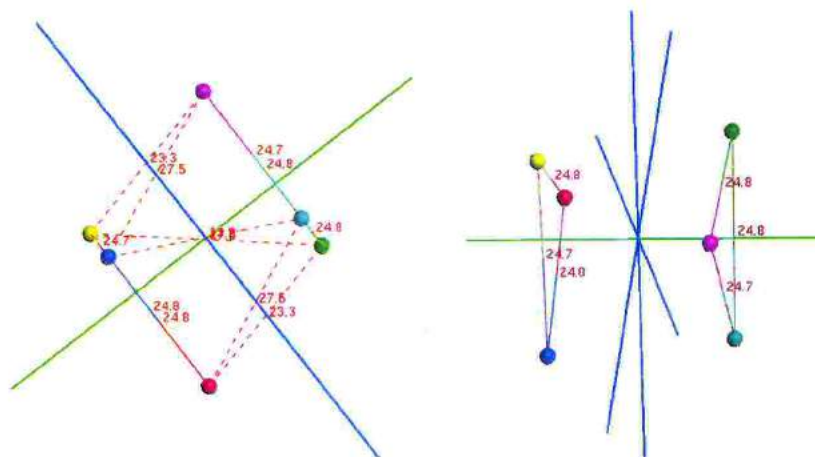


Figure 6.4: Scheme of Ni-sites and NCS axes in NiSOD. (*left*) Ni-ions are found to be arranged in a distorted octahedron with distances between Ni-positions along edges ranging from 23.4 to 27.7 Å. The threefold axis is shown as a green line and the plane of twofold axes as a blue line. (*right*) The twofold axes relate two groups of threefold NCS-related Ni-ions.

Self-rotation calculations were carried out to analyse the NCS within a hexamer, using GLRF of the Replace program package (Tong & Rossmann, 1997). Twofold and threefold non-crystallographic rotation axes could not be clearly identified in the resulting self-rotation maps. In case of crystal form I the reason for this might be the systematic modification of structure factor amplitudes due to the present translational NCS (see appendix A.3). A peak of  $3\sigma$  height indicating a fourfold

axis was present only when reflections to a resolution not higher than 4.5 Å were used in the self-rotation calculation. The peak disappeared upon extension of the resolution to 3.5 Å. This can be explained by the distortion of the octahedral Ni-site arrangement. Information about NCS within a NiSOD hexamer could be extracted from the arrangement of Ni-sites in Fig. 6.4. A threefold axis is present as well as three twofold axes in the plane perpendicular to the threefold. None of these axes runs parallel to a crystallographic axis.

### 6.3 Determination of Phases by MAD

The phase problem for NiSOD was solved by the multiple-wavelength anomalous dispersion (MAD) method that is described in appendix A.2. Fig. 6.5 shows that at 2.0 Å resolution, about 4 % of a reflection's intensity is expected to be available as

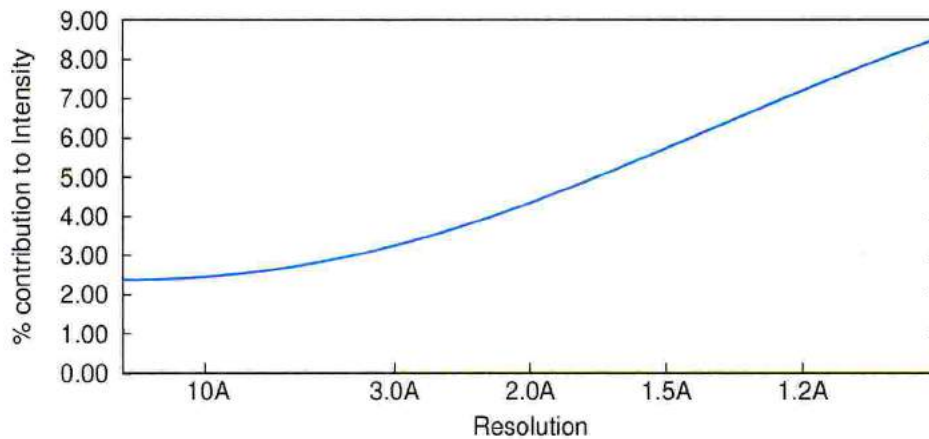


Figure 6.5: Estimated net (i.e. dispersive plus anomalous) signal versus resolution for a MAD experiment on NiSOD at the Ni K edge, assuming one anomalous scatterer per 117 amino acids,  $f'_{min} = -7 e^-$ ,  $f'_{max} = -2 e^-$ ,  $f''_{max} = 4 e^-$  (Merritt, 2001).

anomalous signal for MAD phasing. This low signal is theoretically sufficient if the reflection data are measured with high accuracy, i.e. with a merging R-factor not higher than 4 %. In practice it is found that also higher R-factors are permissible (Boggon & Shapiro, 2000). Fig. 6.5 refers to the net signal arising from contributions of both  $f'$  and  $f''$ . They are calculated as (Hendrickson & Teeter, 1981)

$$\frac{|\Delta F|}{F} = \frac{\sqrt{2N_A}(f'_{A,\lambda 1} - f'_{A,\lambda 2})}{\sqrt{N_P} Z_{\text{eff}}} \quad (f' \text{ contribution}) \quad (6.1)$$

$$\frac{|\Delta F|}{F} = \frac{\sqrt{2N_A} f''_A}{\sqrt{N_P} Z_{\text{eff}}} \quad (f'' \text{ contribution}), \quad (6.2)$$

where  $N_A$  is the number of anomalous scatterers,  $N_P$  the number of non-hydrogen protein atoms and  $Z_{\text{eff}}$  the effective normal scattering power for all atoms ( $6.7 e^-$ , assuming protein atoms and scattering angle = 0). Averaged over the full resolution range of MAD data for NiSOD ( $N_A/N_P = 1/930$ ,  $f'_{A,\lambda1} = -7 e^-$ ,  $f'_{A,\lambda2} = -2 e^-$ ,  $f''_A = 4 e^-$ ), these contributions have the following values

$$\frac{\langle |\Delta F| \rangle}{\langle F \rangle} = 3.5\% \quad (\text{due to } f') \quad \text{and} \quad \frac{\langle |\Delta F| \rangle}{\langle F \rangle} = 2.8\% \quad (\text{due to } f'').$$

Both crystal forms were used in trials of phase determination, however, only crystal form III with one hexamer per asymmetric unit yielded interpretable electron density maps. The difficulty with crystal form I is connected to the fact that either two hexamers in the asymmetric unit are related by a purely translational NCS which leads to systematic weakness of certain groups of reflections (see last section and appendix A.3). Since also the anomalously scattering Ni-ions exploited for phase calculation obey this translational NCS, their contribution to reflection intensities will be weakened in the same way, so that all systematically weak reflections have systematically smaller phase information. In addition to this principle problem, a practical problem with phase calculation programs exists regarding the computational treatment of translational NCS. As all macromolecular crystallography software packages that were available at the time of NiSOD structure determination did not offer the possibility to take into account the intensity modulations connected with translational NCS\*, the important assignment of errors to the calculated phases was largely incorrect. The programs CNS (Brünger *et al.*, 1998), SOLVE (Terwilliger & Berendzen, 1999) and SHARP (de La Fortelle & Bricogne, 1997) which were used for phasing assumed that phase errors are just a function of resolution†, i.e. that errors increase towards higher resolution where the signal to noise ratio of reflections decreases. This results in overestimation of the Figure of Merit (FOM‡) for phases of systematically weak reflections and to increased noise in FOM-weighted electron density maps. The mean FOM of initial phases to 2.4 Å resolution as reported for example by CNS is 0.6 which corresponds to about 50° error in the phase angle. This is commonly considered as sufficient for obtaining interpretable initial maps, however, the resulting maps were not interpretable in any region of the asymmetric unit. The error-related problem can in principle be overcome. Indeed, the phasing program SHELXE (Sheldrick, 2002) which was released one year after the NiSOD structure had been solved, proved

\*Gérard Bricogne, Global Phasing, UK: personal communication.

†Randy Read, University of Cambridge, UK: personal communication.

‡FOM =  $\frac{|F(hkl)_{\text{best}}|}{|F(hkl)|}$  where  $F(hkl)_{\text{best}} = \frac{\sum_{\alpha} P_{\alpha} F(hkl)_{\alpha}}{\sum_{\alpha} P_{\alpha}}$  with the phase probability distribution  $P_{\alpha}$ . FOM is also the weighted mean of the cosine of the deviation of the phase angle  $\alpha$  from the best phase angle:  $\langle \cos(\alpha - \alpha_{\text{best}}) \rangle$ . The maximum FOM thus equals 1.

to be capable of producing an interpretable map from those MAD data of crystal form I which were used previously without success.

Table 6.2 shows dispersive and anomalous differences for datasets of MAD experiments on crystal form I and III and correlation coefficients between anomalous differences.

Table 6.2: Dispersive & Anomalous Differences of MAD Data

data set <sup>a</sup>	Anom. & Disp. Differences <sup>b</sup> , %			C.C. <sup>c</sup> of anom. Differences		
Form I	Pk	Pi	Re	Pk	Pi	Re
Pk	4.8	4.0	6.0	1.0	0.41	0.33
Pi		4.6	6.5		1.0	0.21
Re			3.9			1.0
Form III	Pk	Pi	Re	Pk	Pi	Re
Pk	3.8	3.8	10.8	1.0	0.5	0.23
Pi		3.4	9.6		1.0	0.18
Re			3.4			1.0

<sup>a</sup>Pk, peak-energy; Pi, inflection-point; Re, remote-energy data.

<sup>b</sup>defined as  $\sqrt{(|F_a| - |F_b|)^2} / \sqrt{\frac{1}{2}(\langle |F_a|^2 \rangle + \langle |F_b|^2 \rangle)}$  where  $a$  and  $b$  either stands for  $+(hkl)$  and  $-(hkl)$  within a dataset (anomalous differences, diagonals) or datasets  $a$  and  $b$  (dispersive differences, off-diagonals). Statistics was calculated using CNS with reflections up to 2.8 Å resolution.

<sup>c</sup>Correlation Coefficient

A significant correlation should in practice be above 0.3 for data to a given high resolution limit. This serves as a criterion to cut off those data which should not be included in heavy atom substructure determination and initial phase calculation. Form III MAD data show sufficient quality of anomalous signal for the peak and inflection-point datasets up to 2.8 Å but rather poor quality for the remote-energy dataset. Consequently, an electron density map calculated with phases from a 3-wavelengths MAD phasing were of poorer quality than that with phases derived from 2-wavelengths MAD phasing after omitting the remote energy dataset. This is thought to result from radiation damage during collection of this dataset which was the last to be taken in the MAD experiment. Using the 2-wavelengths MAD phases to 2.8 Å as prior phase information in form of Hendrickson-Lattman coefficients, new phases were calculated now including data to 2.0 Å resolution. Final phasing statistics is given in Table 6.3. The decision which of the two heavy atom enantiomorphs is correct had to be postponed to after density modification since the 2-wavelengths MAD phases did not provide electron density maps which allowed an unambiguous choice.

Table 6.3: Final 2 $\lambda$ -MAD phasing statistics using data to 2.0 Å.

R-Cullis <sup>a</sup>	R-Kraut <sup>b</sup>	Phasing Power <sup>c</sup>	Figure of Merit <sup>d</sup>
0.72	0.03	1.43	0.59

<sup>a</sup>defined as  $\sum ||F_{PH} + F_P| - |F_H|_{calc}| / \sum |F_{PH} - F_P|$   
<sup>b</sup>defined as  $\sum ||F_{PH}|_{obs} - |F_{PH}|_{calc}| / \sum |F_{PH}|_{obs}$   
<sup>c</sup>defined as  $\sum |F_H|_{calc} / \sum ||F_{PH}|_{obs} - |F_{PH}|_{calc}|$   
<sup>d</sup>defined in the text.

Attempts to use heavy atom derivatives of the big cell crystal form (section 5.4) and the single or multiple isomorphous replacement technique to obtain phases were not successful. The X-ray wavelength has been tuned to the L-edge of the respective metal to provide additional anomalous signal for easier heavy atom finding and incorporation in phase calculation but none of the metals appeared to have bound to NiSOD. The metals could have removed the problem of translational NCS in case that they bound differently to the two hexamers in the asymmetric unit. This situation may occur if crystal packing (which differs between the two hexamers) imposes constraints on the accessibility of metal binding sites. The metals then would not obey the translational NCS and fully contribute to anomalous differences used for phasing.

## 6.4 Phase Improvements

Initial 2-wavelengths MAD phases obtained from the crystal form with one hexamer per asymmetric unit (form III crystals) were used to calculate  $\sigma_A$ -weighted (Read, 1986) electron density maps on which density modification had to be performed to choose the correct heavy atom enantiomorph. Solvent flipping and histogram matching as implemented in CNS resulted in maps with well defined protein-solvent boundary and interpretable density in parts of the protein region. Skeletonization of the density provided six  $\alpha$ -helical patches of 20 residues which were model built in the graphics program O (Jones *et al.*, 1991). Utilizing the Ni-ions as reference points, it was evident that every partial structure represented the same patch in each of the six subunits, thus allowing the use of these partial models for determination of NCS operators. The operators relating the partial models to a reference subunit were used in the program DM (Cowtan, 1994) for density modification by solvent flattening, histogram matching and averaging of NCS-related electron density. 'NCS-averaging' is exploited to reduce the noise level in electron density maps, as illustrated in Fig. 6.6.

For this technique, a mask around the reference subunit was determined automat-

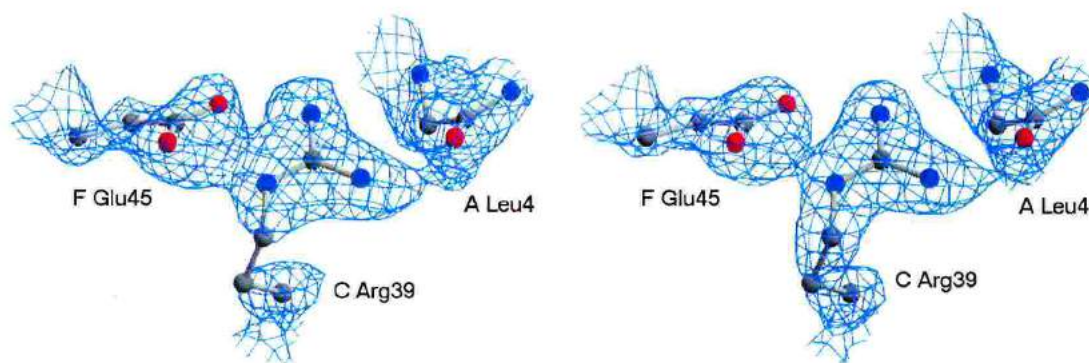


Figure 6.6: Illustration of the improvement of electron density maps by the NCS-averaging technique. The final refined NiSOD model is superimposed onto the electron density. (*left*) Before NCS-averaging. Continuous density is found between three different subunits and a break in the side chain density of an Arg residue. (*right*) After NCS-averaging. Here, correct map interpretation has become easier.

ically by the program and improved, together with the NCS operators, in the first run. The starting correlation coefficient between NCS-related regions was 0.38. In subsequent runs of DM, the improved monomer mask, phases and NCS operators were used iteratively and after the fifth run, the correlation coefficient increased to 0.81. At this stage, the electron density map was interpretable in almost all parts of the protein. Further phase refinement and extension to 1.68 Å resolution of the additionally collected dataset was performed with the program suite ARP/wARP (Perrakis *et al.*, 1997).

The improvement of phases is quantified by the map correlation coefficients in Table 6.4 further below.

## 6.5 Model Building & Refinement

### Model Building

The atomic model was built automatically into the electron density map of the small cell crystal form by ARP/wARP v5.1 (Perrakis *et al.*, 1999). The autotracing procedure of this program is based on putting dummy atoms (oxygen atoms) into the initial (experimentally phased) electron density. The dummy atoms are then interpreted with respect to protein-like patterns that obey stereochemical restraints of a protein main chain. A hybrid model of this partial protein model and uninterpreted dummy atoms is then refined by the program REFMAC v5 (Murshudov *et al.*, 1997) against the X-ray data. A new map is calculated from which an improved hybrid model can be created. Model building and refinement

are automatically iterated until no more amino acids are added to the model. The already determined Ni-ion coordinates were added to an intermediate hybrid model. In this way the initial NiSOD model was obtained to an extent of 660 residues out of 702. The remaining residues (5 at the N-terminus and 2 at the C-terminus per subunit) were model-built in the conventional manner with the graphics program O (Jones *et al.*, 1991).

### Common Points in NiSOD Model Refinements

Before describing specific details of model refinement against various reflection datasets, those points common to all procedures are mentioned. Atom positions and isotropic B-factors were refined with the program CNS (Brünger *et al.*, 1998) against the maximum likelihood target function using the stereochemical restraints from Engh and Huber (Engh & Huber, 1991). Reflections with negative structure factor amplitude were rejected from refinement and no low resolution cutoff was applied. The hexamer's subunits were treated independently, i.e. no NCS restraints were used during refinement. Computational refinement was alternated with model adjustment with the graphics program O (Jones *et al.*, 1991) against  $\sigma_A$ -weighted (Read, 1986) electron density maps of the type  $2F_{obs} - F_{calc}$  (contoured at a  $\sigma$ -level of 1.0 to 1.2) and  $F_{obs} - F_{calc}$  (difference density contoured at a  $\sigma$ -level of both +3.5 and -3.5). The quality of the model's stereochemistry was assessed with the program PROCHECK (Laskowski *et al.*, 1993). The agreement between observed amplitudes and amplitudes calculated from the model was monitored by the Free-R factor (Brünger, 1992). Weighting between experimental data on one hand and stereochemical library values for amino acids on the other hand was continuously and automatically adjusted by CNS in such a way that the model became increasingly restrained to ideal geometry as refinement proceeded. In general, no restraints were applied to bond distances between a Ni-ion and its ligands. The only exception is the refinement of the 'low-dose' dataset (see below).

In the late stage of refinement ( $R_{free} < 25\%$ ) water molecules were inserted in the model based on peaks greater than  $3.8 \sigma$  in  $F_{obs} - F_{calc}$  maps, if the following criteria were fulfilled: the waters' distances to possible hydrogen-bond partners (protein oxygen or nitrogen atoms or already inserted water molecules) had to be between 2.4 and 3.4 Å and the B-factor had to be below a certain value (usually  $55 \text{ \AA}^2$ , depending on the Wilson B-factor). In addition, ordered solvent ions from the crystallization liquor (e.g. sulfate) were added to the model. Their compound coordinates and stereochemistry library files for CNS were taken from the HIC-UP server (Kleywegt & Jones, 1998).

### Refinement of the 'small cell' model (Crystal Form III)

The refinement of this model is referred to as 'high-dose small cell' for reasons explained in the following subsection. The starting molecular model was obtained from model building as described above and refined against the 1.68 Å dataset. Initially only, experimental phases (i.e. those from MAD phasing) were included in refinement besides model-derived phases, however, the resulting electron density maps were not superior to those based on model phases alone. The last two residues of each subunit are not well ordered as judged by high B-factors and partial lack of electron density in  $2F_{obs} - F_{calc}$  maps. Eight sulfate ions were built into the electron density, two of which lie on the threefold symmetry axis. One sulfate is located close to each Ni-ion. In addition, three acetate ions were inserted into the model in three of three of the hexamer's subunits. Final refinement statistics is compiled in Table 6.5 at the end of this chapter.

The progress in the determination of phase angles from MAD phasing to the final refined model can best be summarised with the help of map correlation coefficients in Table 6.4. These allow comparison of electron density maps from various stages of phase improvement with respect to the final map.

Table 6.4: Map Correlation Coefficients using data to 2.0 Å.

Stage of phase determination	Map Correlation Coefficient
Map after MAD phasing	0.40
Map after Solvent Flipping	0.79
Map after NCS Averaging	0.83
Map after Model Building	0.87

### Refinement of 'big cell' models (Crystal Form I)

The final refined model of the 'small cell' crystal form was placed twice in the asymmetric unit of the 'big-cell' crystal form, applying to all protein atoms the transformation matrix that was obtained by superposition of pairs of Ni-ion octahedra. The known positions of the Ni-ions served as reference points for correct placement of each hexamer. Prior to refinement of individual atomic coordinates, the position of each hexamer (as a rigid body) was refined. Applying the same protocol as above, the model was then refined against the 1.6 Å dataset. Table 6.5 lists final statistics. Again, the attribute '*high-dose*' was assigned since both the small cell and the big cell high-resolution datasets were obtained from exposure of the crystals to a high X-ray dose per image which was necessary to record useful data up to the respective high-resolution shell. In the course of model

interpretation, which is the subject of the next chapter, it became clear that X-ray induced ionisation in the crystal resulted in reduction of the metal centre during data collection. The need for a 'low-dose' dataset became therefore apparent in order to provide structural information about the *resting state* of the enzyme.

Two ways were undertaken to obtain insight into the resting enzyme's metal centre geometry. One is to use only the initial images collected from each crystal and merge data from a sufficient amount of crystals to end up with a complete dataset (Berglund *et al.*, 2002). In this way one can retain the high resolution of the 'one-crystal-dataset' which suffered from X-ray induced reduction. Another way is to collect only medium resolution data from one crystal and to sacrifice the high resolution data. The advantage of this second way is that elevated noise in higher resolution shells due to problems in merging data from many crystals is not present. The dataset obtained using the first protocol manifested this problem in bad merging statistics ( $R_{sym} > 30\%$ ) in shells at a resolution of 2.4 Å and higher. Both ways offer the possibility of monitoring the gradual reduction in the course of X-ray exposure by adequate assembly of images which belong approximately to the same state of reduction.

#### 1) Assembly of datasets

The initial ten images collected from 14 crystals were scaled and merged together to yield a dataset of about 90% completeness up to 2.0 Å resolution. As these 14 datasets had already been collected before the problem of X-ray induced reduction was identified, the crystals were mounted with mutually random on the goniostat. The final 'high-dose' model was subsequently refined against the resulting merged data. The part of the Ni-ion's ligand environment which on the basis of spectroscopic data (section 7.3) was expected to be affected by X-ray induced reduction was omitted from the model: all atoms of His 1 and those within a cushion of 2 Å around its atoms were not included in initial refinement and calculation of maps (so-called 'conventional omit maps'). Omitting these atoms is necessary to avoid the influence (bias) of structure factor amplitudes  $F_{calc}$  calculated from the X-ray reduced enzyme model on  $(2)F_{obs} - F_{calc}$  electron density maps of resting NiSOD. The omitted atoms were then built again into the omit maps and subjected to refinement with the program REFMAC (Murshudov *et al.*, 1997). Unlike the refinement procedures described earlier, this refinement included a restraint on the distance between the imidazolite nitrogen N $\delta$  of His 1 and the Ni(III)-ion as suggested by the omit maps at the metal centre (see section 7.3). The restraint value of 2.1 Å was taken from (Orpen *et al.*, 1989) and is based on small molecule X-ray diffraction data. This restraint, however, was dropped in subsequent

refinement cycles because both  $2F_{obs} - F_{calc}$  and  $F_{obs} - F_{calc}$  electron density maps did not support such a close approach of the imidazole ring to the Ni-ion. Thus, the imidazolate was allowed to drift back into electron density contoured at  $1.0 \sigma$  level.

## 2) Medium resolution dataset

The initial fraction of the first dataset collected in the MAD experiment on the big cell crystal form (see Table 6.1 under Form I, PK) was used to obtain maps of the resting enzyme state. The 'high-dose' model was refined against data of the first 320 images out of 3 times 480 images collected in total on this crystal during the MAD experiment. The crystal diffracted to at least  $1.8 \text{ \AA}$  but the initial two datasets (peak and inflection point) were collected to  $2.2 \text{ \AA}$  resolution only. As just described, conventional omit maps were calculated and, in addition, 'simulated annealing omit maps' were calculated in CNS to further reduce model bias, with the atoms mentioned above being initially omitted from the annealing procedure and map calculation. A restraint for the distance between  $N\delta$  of His 1 and the Ni(III)-ion was introduced for a few refinement cycles in REFMAC and was subsequently dropped. The 480 images of the last dataset, the remote energy dataset, served as 'intermediate-dose' data which were used for model refinement in the same way as the 'low-dose' data except that there was no need to introduce a His 1  $N\delta$  to Ni(III) distance restraint.

These two ways of obtaining electron density maps that correspond as close as possible to the resting enzyme state yielded the same results. In the following chapter, discussions and figures will refer to the second way for which refinement statistics is given in Table 6.5.

## Refinement of the thiosulfate-reduced enzyme model

The 'high-dose' model was also used as starting model for refinement of the  $S_2O_3^{2-}$ -reduced enzyme dataset to  $2.1 \text{ \AA}$  resolution. In a late stage of refinement one  $S_2O_3^{2-}$ -ion per subunit was modelled into  $F_{obs} - F_{calc}$  electron density at contour levels at or above  $3.0 \sigma$ . Coordinates and stereochemistry library files for CNS were taken from the HIC-UP server (Kleywegt & Jones, 1998). The refined B-factors of these ions (Table 6.5) is on average about  $50 \text{ \AA}^2$  higher than those of protein atoms and indicate an elevated level of mobility or low specificity of binding to the protein.

## Refinement of the enzyme model in complex with inhibitors

The 'high-dose' model served as starting model for refinement against inhibitor-soak datasets using either azide or cyanide at various concentrations (section 5.3). The crystals diffracted typically to about  $1.8\text{-}1.9 \text{ \AA}$  resolution for lower inhibitor

concentrations (50 mM  $\text{CN}^-$  or 150 mM  $\text{N}_3^-$ ) and to 2.2 Å resolution for higher concentrations (200 mM  $\text{CN}^-$  or 800 mM  $\text{N}_3^-$ ). As for the  $\text{S}_2\text{O}_3^{2-}$ -reduced enzyme, all water molecules were removed from this model before it was used in the first refinement cycle in order to avoid model bias at possible inhibitor binding sites. After each cycle of automated water picking on a  $F_{obs} - F_{calc}$  electron density map, those waters which were located close to the active site were repeatedly removed until in the late stage of refinement, the dataset was assessed as to whether the inhibitor had bound to the enzyme or not.

#### **Refinement of the Xenon-pressurized enzyme model**

Xenon binding sites were first indicated by anomalous difference Fourier maps. 17 outstanding peaks were found and their coordinates were inserted in the 'high-dose' model as xenon atoms. After positional and isotropic B-factor refinement in REFMAC, the Xe-sites' occupancies were adjusted to values between 0.2 and 0.6. All sites showed high degree of anisotropy, as could be seen from difference Fourier maps. This is a commonly encountered feature of xenon (and also krypton) sites in proteins.

Table 6.5: Final refinement statistics

	low-dose		intermediate-dose		high-dose		high-dose		S <sub>2</sub> O <sub>3</sub> <sup>2-</sup> -reduced		Xe-derivative	
	big cell		big cell		big cell		small cell		big cell		big cell	
Resolution range (Å)	36.6 - 2.2		31.1 - 2.2		42.6 - 1.6		34.3 - 1.68		40.2 - 2.1		20.0 - 2.13	
(outer shell)(Å)	2.32 - 2.2		2.32 - 2.2		1.69 - 1.6		1.76 - 1.68		2.21 - 2.1		2.19 - 2.13	
Completeness <sup>a</sup> (%)	97.0 (98.4)		99.8 (98.7)		98.9 (97.6)		99.1 (96.0)		99.6 (99.6)		99.8 (100)	
I/σ(I)	12.3 (6.1)		13.3 (5.5)		13.0 (2.8)		11.0 (2.7)		10.3 (1.9)		6.1 (3.5)	
R <sub>sym</sub> <sup>b</sup> (%)	6.5 (20.8)		4.8 (13.6)		8.0 (26.0)		4.3 (27.6)		5.1 (40.6)		8.5 (18.5)	
No. of reflections	80907		83880		213373		108081		95957		90704	
R-factor <sup>c</sup> (%)	17.2		15.7		18.4		17.7		20.4		15.2	
R <sub>free</sub> (%)	18.0		16.7		20.2		20.0		23.8		20.0	
Ramachandran plot												
core (allowed) (%)	95.6 (4.4)		95.6 (4.4)		95.8 (4.2)		95.5 (4.5)		95.8 (4.2)		96.0 (4.0)	
RMSd from ideality <sup>d</sup>												
Bonds (Å), angles (°)	0.005, 1.0		0.007, 1.2		0.005, 1.0		0.005, 1.0		0.006, 1.0		0.025, 1.7	
No. of atoms [B-factor (Å <sup>2</sup> )]												
Non-H protein atoms	11 172 [19.3]		11 172 [19.6]		11 172 [19.7]		5586 [29.6]		11 172 [41.7]		11 172 [21.4]	
Nickel-ions	12 [29.9]		12 [23.3]		12 [18.4]		6 [28.3]		12 [46.2]		12 [29.6]	
Water	1 538 [32.1]		1 538 [32.0]		1 695 [33.6]		901 [44.0]		504 [47.2]		1 689 [36.8]	
Sulfate-ions	2×8 [46.0]		2×8 [48.7]		2×8 [44.6]		8 [61.6]		2×6 [105]		2×8 [58.9]	
Acetate-ions	-		-		-		3 [31.2]		-		-	
Thiosulfate-ions	-		-		-		-		2×6 [96.7]		-	
Xenon-ions	-		-		-		-		-		2×9 [57.5]	
PDB Codes	1Q0D		1Q0F		1Q0G		1Q0M		1Q0K		-	

<sup>a</sup>Values in parentheses are for the outer resolution shell.

<sup>b</sup>defined in Table 6.1

<sup>c</sup>R-factor =  $\sum_{hkl} |F_{obs}| - k |F_{calc}| / \sum_{hkl} |F_{obs}|$ ; R<sub>free</sub> defined likewise, using a 5% fraction of reflections which was omitted from refinement.

<sup>d</sup>RMSd = root mean square deviation from ideal geometry.

## Chapter 7

# The Crystal Structures of NiSOD

### 7.1 Overall Structure

The hexamer construction in NiSOD can be thought of as arising from two hollow hemispheres each of which is built by a group of threefold non-crystallographic symmetry (NCS) related subunits. These hollow hemispheres face each other at an equatorial plane and the threefold NCS axis connects the poles in this scheme. The hemispheres are interlocked at the equator plane in a way that each subunit of one hemisphere reaches into the gap opened up by two subunits of the other hemisphere. The hexameric assembly of NiSOD exhibits a globular shape in which all protein atoms lie in a hollow sphere with outer diameter of 72 Å and inner diameter of 23 Å (Fig. 7.1). Twofold symmetry axes are present in a plane perpendicular to the threefold axis. The interior of the hexamer is accessible via three thin channels each of which runs along a twofold symmetry axis. It contains solvent water as well as sulfate ions from the crystallization liquor, indicating the exchange of solvent molecules between the enzyme's exterior and interior. Since the minimum in the diameter of a channel is smaller than the van der Waals size of a sulfate ion, structural flexibility seems to exist between pairs of subunits that form a channel. Ni-ions are arranged as a distorted octahedron with distances along edges ranging from 23.4 to 27.7 Å (Fig. 7.2).

Interactions between subunits are mainly of hydrophobic character since approximately two thirds of residues in the interface have non-polar side chains. The subunits are also held together by polar interactions between residues of the N-terminal active site loop (see next section) and  $\alpha$ -helices as well as between  $\alpha$ -helices. About 35% of each subunit surface is buried in interfaces to four neighbouring subunits as calculated by the internet tool 'Protein-Protein Interaction Server' (Jones & Thornton, 1996).

The 'big cell' and the 'small cell' crystal forms differ in the identity of side chains

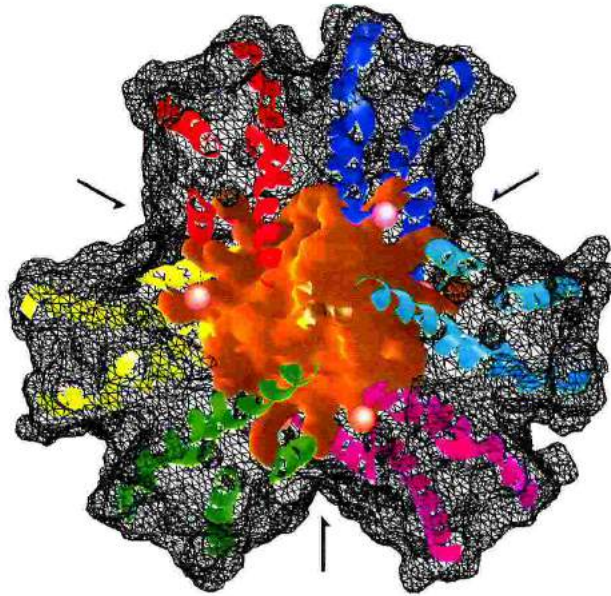


Figure 7.1: Representation of the solvent accessible surface of a NiSOD hexamer viewed along the hexamer's threefold symmetry axis. The outer surface (black mesh) is sliced to allow the view to the inner solvent filled space (in gold) and the protein backbone trace (color code: chain A yellow, B blue, C red, D magenta, E cyan, F green. Ni-ions are depicted as salmon-coloured spheres). Arrows indicate the three twofold symmetry axes in the paper plane and the entrance to channels which render the inner space accessible to solvent molecules. The Figure was prepared with GRASP (Nicholls *et al.*, 1991).

involved in crystal contacts and crystal packing is more compact in the 'big cell' form. Here, each hexamer is in contact with seven other hexamers whereas there are eight in the 'small cell' form. The larger number of direct neighbours leads to a smaller contact area of any two hexamers and necessitates enlarged solvent filled gaps in the latter crystal form in order to avoid overlap. This is reflected also by its higher solvent fraction (51% compared to 43.7% which excludes water in the protein's hydration shell). Hexamer interactions in the 'small cell' form are additionally mediated by three acetate-ions from the crystallization liquor which bridge Glu 69 of subunits C, D and F to residues of neighbouring hexamers.

The need for the 'big cell' crystal form to accommodate two hexamers in the asymmetric unit arises from a shift of about 5.6 Å parallel to the crystallographic  $a$  axis of every second hexamer when looking along the  $b$  axis. This breaks the crystallographic translational symmetry along the  $b$  axis, resulting in a doubled unit cell with respect to the 'small cell' crystal form and in the generation of a purely translational non-crystallographic symmetry between pairs of hexamers in the 'big cell' crystal (see appendix A.3 for more details).

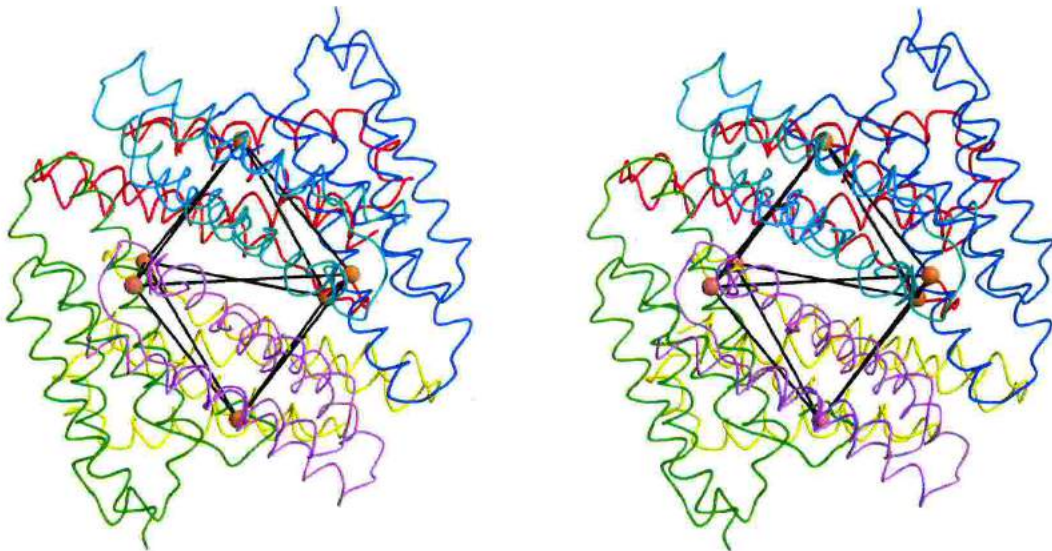


Figure 7.2: Smoothed  $C_{\alpha}$ -trace representation in stereo of a hexamer viewed along a twofold axis, emphasizing the octahedron-like Ni-ion arrangement (black lines). The Figure was prepared with MolScript (Kraulis, 1991) and Raster3D (Merritt & Bacon, 1997).

## 7.2 Subunit Structure and Interactions

The subunit structure of NiSOD comprises 117 residues (13.2 kDa) in the mature enzyme and reveals a four-helix bundle in the all-antiparallel topology (Fig. 7.3). The subunit's hydrophobic core consists of 17 aliphatic apolar residues except for Phe63. This residue participates together with Tyr9, Tyr62, Phe111 and Trp112 in an aromatic stacking at the N-terminal side of the four-helix bundle, connecting the beginning of helix 1 with the ends of helix 2 and 4 (Fig. 7.3). A short  $\alpha$ -helical loop spanning from Lys65 to Tyr70 connects the second and third helix. The eight consecutive N-terminal residues form an almost closed loop that hosts the Ni in its centre. The Pro5 in *cis*-conformation imposes the conformation of this loop, which is 'closed' by a hydrogen-bond of His1 N to Val8 O. The requirement of proteolytic cleavage of 14 N-terminal amino acids of immature NiSOD (section 4.2) now finds a plausible structural explanation. If those amino acids were still present during hexamer assembly, either a clash into the neighbouring subunit would occur or the Ni-site would be disrupted from the loop.

The four-helix body of a subunit is not involved in stabilizing the respective N-terminal loop since within a subunit there is no direct contact between residues of the core of the protein and this loop. Instead, the N-terminal active site loop of

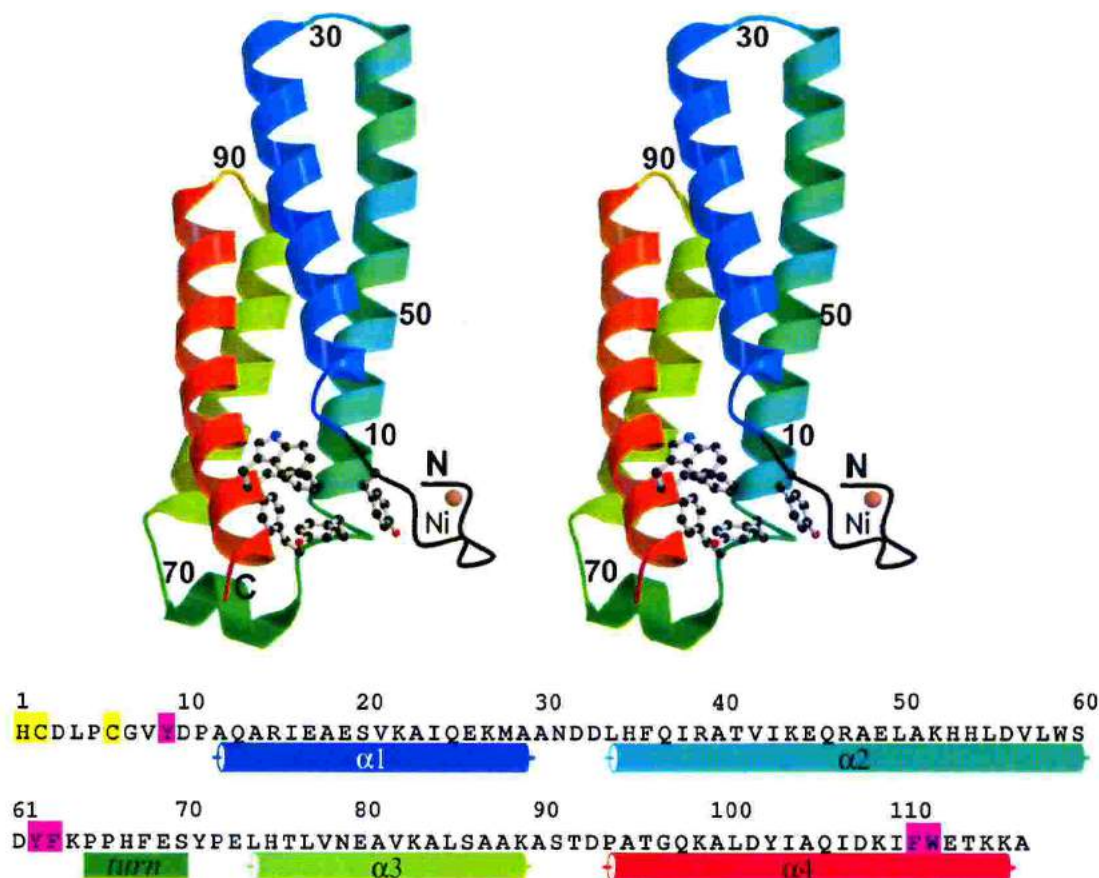


Figure 7.3: MolScript (Kraulis, 1991) ribbon representation in stereo of a NiSOD subunit. The N-terminal loop hosting the Ni-ion protrudes from the body of the four-helix bundle. Residues involved in aromatic stacking are shown in ball-and-stick representation. In the amino acid sequence below, these residues are highlighted in magenta and Ni-ion ligands (see next section) in yellow. Cylinders indicate the four helices ( $\alpha 1$  to  $\alpha 4$ ) and the  $\alpha$ -helical turn.

one subunit, e.g. subunit A, interacts via hydrogen-bonds with two neighbouring subunits, here C and F (Fig. 7.4). His 1 N $\epsilon$  of subunit A takes part in a hydrogen-bonding triangle with Glu 17 and Arg 47 of subunit C. Moreover, main chain oxygen atoms of Asp 3 and Leu 4 of subunit A hydrogen-bond to the side chain of Arg 39 in subunit C. The side chain oxygen atoms of Asp 3 of subunit A hydrogen-bond to the side chains of Lys 52, Ser 86 and Lys 89 of subunit F. Thus, the interactions between the subunits, rather than the subunit's shape on its own, are crucial for stabilization of the active site loop. This was confirmed by mutagenesis studies on some key residues, namely on His 1, Asp 3, Glu 17, Arg 39 and Arg 47. They were performed in the laboratory of Prof. Kang and are summarized in Table 7.1.

All His 1 mutations lead to inactivation of the enzyme which, however, cannot be at-

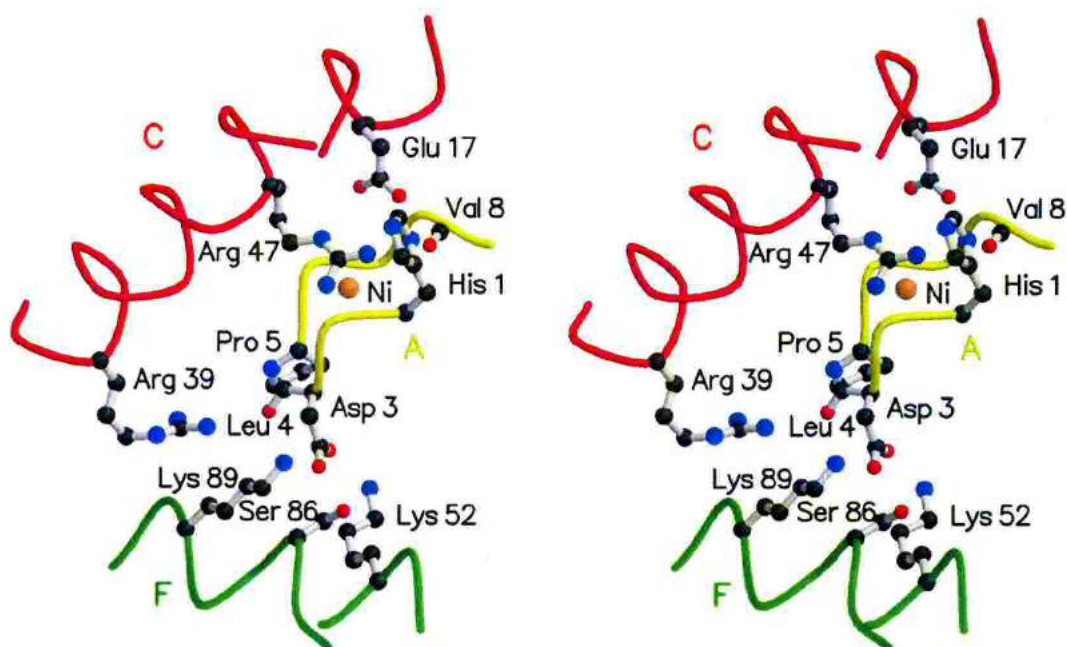


Figure 7.4: MolScript (Kraulis, 1991) stereo representation of residues linking the active site loop to neighbouring chains by polar interactions.  $C_{\alpha}$ -traces are coloured as in Fig. 7.1.

Table 7.1: Activities of NiSOD mutant proteins expressed in *S. lividans* TK24  $\Delta$ sodN

Mutated residue	Mutated to	Activity <sup>a</sup> in cell extracts
His 1	Ala, Cys, Asp, Lys, Asn, Gln, Arg, Trp, Tyr	n.d. <sup>b</sup>
Asp 3	Ala	23 %
Tyr 9	Ala	n.d.
	Phe	78 %
	Lys	n.d.
	Gln	n.d.
	Trp	45 %
Glu 17	Ala	n.d.
Arg 39	Ala	n.d.
Arg 47	Ala	89 %

<sup>a</sup>SOD activity was measured by standard cytochrome c assay and is given with respect to wild type activity, see (Wuerges *et al.*, 2003) for further details.

<sup>b</sup>not detected (defined as activity < 5%)

tributed solely to reduced loop stabilization since His 1  $N\delta$  acts as ligand to the metal centre. The Arg 47 to Ala mutation did not severely impair enzyme activity while the Glu 17 to Ala and Arg 39 to Ala mutants showed no detectable SOD activity. The Asp 3 to Ala mutant showed little but detectable SOD activity. Therefore, stability

of the active site loop appears to depend critically on polar interaction of Glu 17 to His 1 and of Arg 39 to Asp 3. This suggests that the interaction provided by active site loop hydrogen-bonds of e.g. subunit A to subunit C is more crucial for stability than that to subunit F. In addition, after expression of the Arg 39 mutant protein in wild type *S. coelicolor* A3(2) strain, the observed number of bands after activity staining on native polyacrylamide gel suggests that at least three non-mutant subunits are required for SOD activity (S.-O. Kang, personal communication).

Mutations of Tyr 9 to non-aromatic residues demonstrate the importance of this residue in formation of the aromatic stacking that stabilizes the N-terminal side of the four-helix bundle. Differences in maintained activity after Tyr 9 mutation to other aromatic residues (Phe and Trp) may be explained by obstructed active site accessibility in case of tryptophan (see Fig. 7.9). Both mutations, however, prevent the hydrogen-bonds formed by the phenolic oxygen of Tyr 9, as will be discussed in more detail in section 8.1.

## 7.3 Active site Structure

First insight into the coordination environment of the redox-active Ni-centre came from Electron Paramagnetic Resonance (EPR) and X-ray Absorption Spectroscopy (XAS) as presented in section 4.3. The Ni(III)-ion in the resting enzyme was proposed by XAS to be ligated by three sulfur atoms, a nitrogen atom and possibly one more nitrogen or oxygen atom. EPR suggested one nitrogen ligand in an axial position. Upon reduction to a formal Ni(II)-site by dithionite, a planar coordination geometry is indicated, implying the loss of one (or two) ligands of the N- (or O-) type in the axial position. The following sections describe the active site as observed in the crystal structures of untreated and thiosulfate-reduced NiSOD.

### 7.3.1 Resting Enzyme

The structures of NiSOD in both 'small cell' and 'big cell' crystal forms initially revealed a Ni coordination by the amino group of His 1, the amide group of Cys 2, and two thiolate groups, Cys 2 and Cys 6 in the N-terminal loop (Fig. 7.6 C). The imidazole of His 1 was not found to coordinate the Ni-ion but was rather involved in hydrogen-bonds to the main chain O atom of Val 8 via N $\delta$  and a neighbouring subunit via N $\epsilon$  (Fig. 7.4). Since EPR spectra, however, strongly suggested the axial N-ligand at physiological pH 7.4, EPR spectra of NiSOD were examined at various pHs and at the same buffer conditions from which the crystals were grown. Although there were small changes in the  $g$  values and hyperfine splitting constants, the EPR spectra still exhibit the  $g_3$ -triplet showing that the axial nitrogen ligand is not lost

upon pH change or under buffer conditions of crystallization (Fig. 7.5).

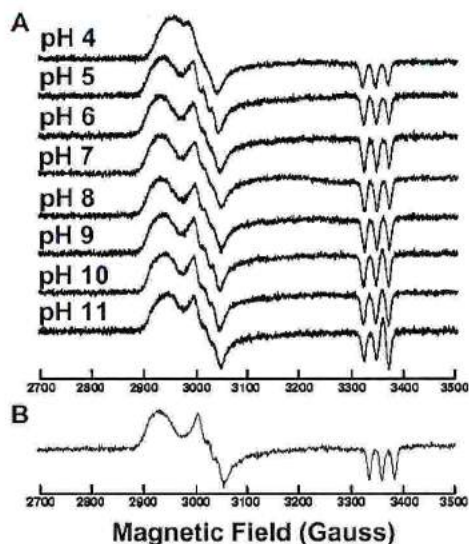


Figure 7.5: (A) The pH-dependence of EPR spectra of NiSOD using various buffer systems (adjusted to each pH with NaOH). (B) EPR spectrum under buffer conditions of crystallization. Graphs from S.-O. Kang, personal communication.

The discrepancy between spectroscopic and crystallographic results concerning Ni(III) ligation are explained considering the effect of X-ray radiation on the redox state of the Ni-ions. It has been observed that radiation-induced changes of the redox state can take place during X-ray data collection (see (Berglund *et al.*, 2002) and references therein). The reduction of the initially resting NiSOD through the course of X-ray irradiation became evident from  $F_{obs} - F_{calc}$  omit maps calculated with an initial fraction of data collected in a MAD experiment on the 'big cell' crystal form (section 6.5, 'low-dose' dataset). These maps show electron density connecting the His 1 imidazole to the Ni-ion (Fig. 7.6 A, *right*). This implies the possibility of rotation around the  $C_{\beta}$ - $C_{\gamma}$  bond of the His 1 imidazole (Fig. 7.7). The N $\delta$  to Ni-ion distance as found in  $2F_{obs} - F_{calc}$  maps of the 'low-dose' dataset is 2.63 Å on average (Fig. 7.6 A, *left*). This distance exceeds the commonly found bond length between Ni(III) and imidazoles (Orpen *et al.*, 1989) by about 0.5 Å and may indicate that already at an early stage of data collection X-ray-induced reduction occurs in a substantial fraction of Ni-sites in the crystal. The map indicates a degree of rotation that varies substantially among the 12 subunits in the asymmetric unit, a fact that might be explained by crystal-packing dependence of X-ray induced generation and propagation of photoelectrons leading to reduction of the Ni-centres.

Another experimental verification of the X-ray-induced reduction of Ni-sites was obtained by merging reflection data collected on 14 crystals, each contributing only

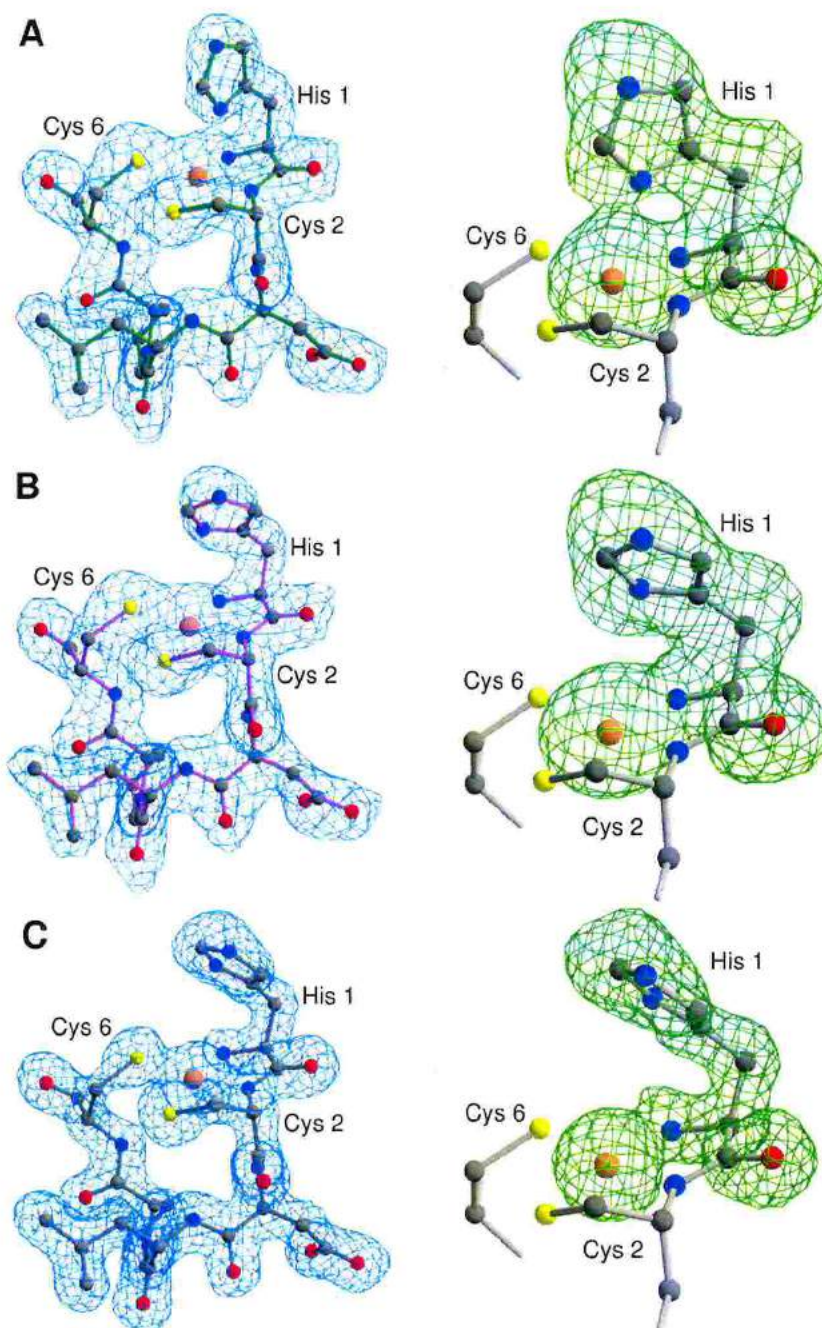


Figure 7.6: Structures of the Ni-centre in NiSOD (here of subunit F) captured at successively increasing X-ray doses. The left part of each panel shows  $\sigma_A$ -weighted (Read, 1986)  $2F_{obs} - F_{calc}$  electron density maps and the right part simulated annealing  $F_{obs} - F_{calc}$  maps, contoured at  $3\sigma$ , with His 1 and Ni omitted from calculations using CNS. (A, left) The fifth ligand His 1 N $\delta$  (2.5 Å distant to Ni-ion here) is revealed at low X-ray exposure (map resolution 2.2 Å, 1.0  $\sigma$  contour level). (right) Continuous  $F_{obs} - F_{calc}$  density between His 1 N $\delta$  and the Ni-ion is present. (B) After longer exposure of the same crystal as in (A), the imidazole ligation is disrupted. (C) Map at 1.6 Å resolution obtained with the highest X-ray dose from a crystal different from that in (A) and (B). The Figure was prepared with BobScript (Esnouf, 1999).

the initial ten frames, for calculation of an electron density map (section 6.5). The map at 2.0 Å resolution confirms the liganding imidazole conformation and shows distances between His 1 N $\delta$  and the Ni-ion very similar to those of the 'low-dose' dataset. This is indicative of a reduction process which starts in the very beginning of X-ray data collection. Consequently, the electron density map in Fig. 7.6 A and the corresponding N $\delta$  to Ni-ion distance represent an early intermediate state of the active site geometry in the transition from the resting enzyme to its reduced form (described below). This is also reflected by the temperature factors of His 1 side chain atoms being about 10 Å<sup>2</sup> higher than the average value of all protein atoms. Ligation of His 1 in the resting state of the enzyme, however, is evident and the effect of its disruption upon X-ray exposure becomes visible in Fig. 7.6 B from maps calculated with an 'intermediate-dose' dataset collected on the same crystal (section 6.5). Here, the imidazole ring has turned about 55° relative to the conformation seen in the 'low-dose' structure such that N $\delta$  reaches hydrogen-bond distance to the carbonyl oxygen of Val 8 (Fig. 7.7).

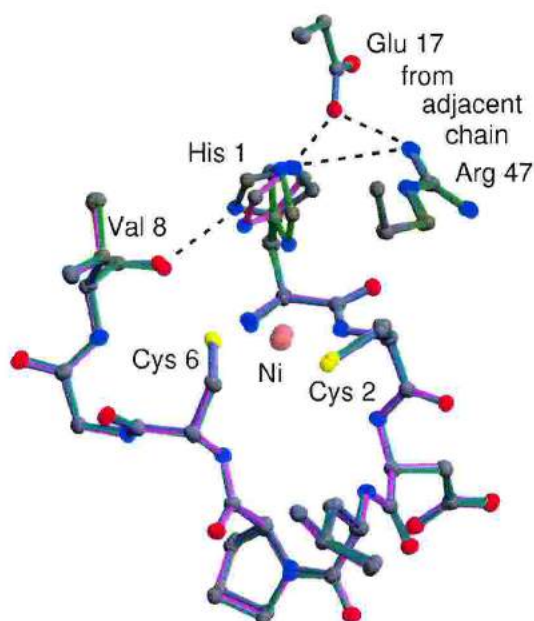


Figure 7.7: Superposition of the model structures in Fig. 7.6 (A) in green, (B) in magenta and (C) in grey illustrating the X-ray-induced His 1 imidazole rotation upon which N $\delta$  reaches a distance of about 2.9 Å to Val 8 O, thereby maintaining the hydrogen-bond triangle of His 1 N $\epsilon$  to Glu 17 O $\epsilon$  and Arg 47 N $\eta$  of an adjacent subunit. The Figure was prepared with MolScript (Kraulis, 1991).

Fig. 7.6 C shows the Ni-site structure initially obtained from a 'high X-ray dose' data set at 1.6 Å resolution. The imidazole has turned about 60° relative to the 'low-dose'

structure. Based on the observed hydrogen-bond pattern of the imidazole nitrogens in this conformation, His 1 is believed to be double-protonated. The ligands are in a slightly distorted *cis* square-planar geometry which equals the situation observed for the thiosulfate-reduced NiSOD. The angle between planes defined by N(His 1)-Ni-N(Cys 2) and S(Cys 2)-Ni-S(Cys 6) is  $7.5^\circ$  on average over all 12 subunits in the asymmetric unit.

### 7.3.2 Thiosulfate-Reduced Enzyme

Sodium thiosulfate  $\text{Na}_2\text{S}_2\text{O}_3$  was used as reducing agent to mimic the reduction of the metal centre on the first encounter with superoxide. The Ni(II)-coordination environment as deduced from the 2.1 Å crystal structure of the thiosulfate-reduced NiSOD (Fig. 7.8) has a square-planar geometry with ligand distances to the Ni-ion close to those found in structures shown in Fig. 7.6. Distances averaged over the 12 (6) independently refined subunits in the asymmetric unit of the 'big cell' ('small cell') crystal form are compiled in Table 7.2.

Table 7.2: Ni-ion bond lengths in NiSOD (Å)

	low-dose big cell	intermediate-dose big cell	high-dose big cell	high-dose small cell	$\text{S}_2\text{O}_3^{2-}$ -reduced big cell
Ni - His 1 N $\delta$	2.63	3.69	3.87	3.96	3.81
Ni - His 1 N	2.11	2.12	2.06	2.07	2.17
Ni - Cys 2 N	1.93	1.94	1.93	1.94	1.99
Ni - Cys 2 S $\gamma$	2.24	2.23	2.22	2.24	2.30
Ni - Cys 6 S $\gamma$	2.26	2.25	2.20	2.18	2.29

His 1 is in the same conformation as observed in the 1.6 Å structure obtained after long exposure to X-rays. The hydrogen-bonding pattern of N $\epsilon$  remains unchanged with respect to the 'low-dose' crystal structure (see Fig. 7.7). In particular Glu 17 may be regarded as an anchor for the imidazolate, leaving the rotation about the C $\beta$ -C $\gamma$  bond as the only degree of freedom in His 1 imidazole movements during catalysis. The electron density map in Fig. 7.8 shows one thiosulfate-ion ( $\text{S}_2\text{O}_3^{2-}$ ) per subunit 7-8 Å away from each metal centre at the surface of the inner open space of the hexamer. One water molecule is found close to but not within hydrogen-bond distance from the Ni-ion and is involved in a hydrogen-bonding network to Asp 3 N, Tyr 9 O $\eta$  and Asp 61 O $\delta$ 2. The precise bonding pattern of thiosulfate-ions varies among the 12 subunits in the asymmetric unit, indicating a certain degree of disorder and low specificity of binding.

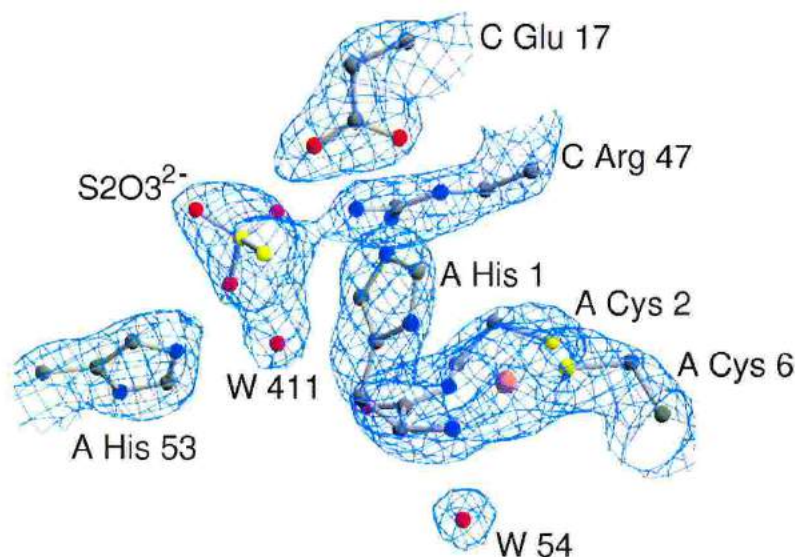


Figure 7.8: The  $2F_{obs} - F_{calc}$  electron density map of thiosulfate-reduced NiSOD contoured at  $1.1 \sigma$  shows the square-planar Ni(II) coordination and the hydrogen-bond pattern of the  $S_2O_3^{2-}$ -ion in subunit A. One water molecule (labelled W 54) is observed in the solvent accessible pocket (see Fig. 7.9) about  $4.1 \text{ \AA}$  away from the Ni-ion. The Figure was prepared with BobScript (Esnouf, 1999) and Raster3D (Merritt & Bacon, 1997).

## 7.4 Active site Accessibility

Upon approaching the active site, the access is first impeded by the side chains of Pro5 and Tyr9 and then obstructed by a remarkable arrangement of the loop's backbone nitrogen atoms (Fig. 7.9 A). As a result, a depression or 'pocket' is formed in the outer surface of the hexamer. It is solvent accessible through the bottleneck at its entrance which is due to Pro5 and Tyr9 about  $5 \text{ \AA}$  away from the Ni-ion.

Accessible area is defined as the area traceable by the centroid of a probe of given radius. The radius of  $1.4 \text{ \AA}$  corresponds to that of a water molecule. Atomic accessibility values were calculated with the program NACCESS (Hubbard & Thornton, 1993) applying a surface probe radius of  $1.25 \text{ \AA}$  and a Ni-ion radius of  $1.0 \text{ \AA}$  as upper estimate of the ionic radius of about  $0.6 \text{ \AA}$  (Shannon, 1976). Calculations of solvent accessible areas for active site atoms reveal that both the Ni-ion and four of five ligands are essentially buried. A non-zero accessible area is obtained solely for His 1 N, which amounts to only about  $1.1 \text{ \AA}^2$ .

In all but the thiosulfate-reduced NiSOD structures, two water molecules (W 828 and W 54 in Fig. 7.9 A) are found in the pocket. W 828 is located close to the vacant

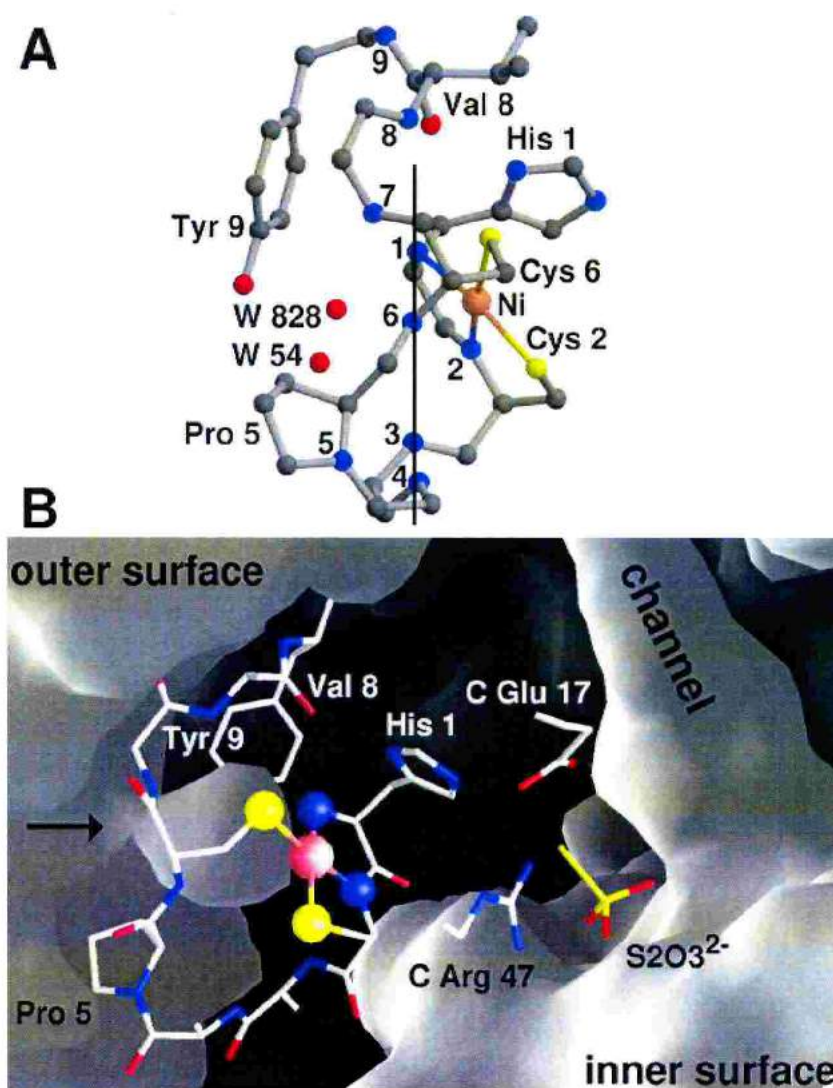


Figure 7.9: Accessibility of the active site of NiSOD. (A) Active site environment from His 1 to Tyr 9 of the 'high-dose' structure (Fig. 7.6C). Nitrogen atoms are labelled with the respective residue number. For Cys 2 to Gly 7 only backbone atoms are shown and oxygen atoms are omitted for clarity. Backbone nitrogen atoms from His 1, Asp 3, Cys 6 and Gly 7 separate the Ni-ion and all other ligands (Cys 2 N, Cys 2 S $\gamma$ , Cys 6 S $\gamma$ , right to the vertical line) from the solvent accessible pocket (hosting two water molecules, W 54 and W 828, left to the line). The Figure was prepared with MolScript (Kraulis, 1991) and Raster3D (Merritt & Bacon, 1997). (B) Surface representation of thiosulfate-reduced NiSOD at the active site loop and the innermost end of a channel that allows thiosulfate-ions to approach the Ni-sites. Only selected side chains are shown. The solvent accessible pocket close to the Ni-centre is marked by an arrow and exhibits a bottleneck mainly formed by Pro 5 and Tyr 9 about 5 Å away from the Ni-ion. The Figure was prepared with GRASP (Nicholls *et al.*, 1991).

axial position (i.e. opposite the His 1 imidazole) at about 3.5 Å from the Ni-ion, 3.3 Å from His 1 N and hydrogen-bonds to Cys 6 N. High temperature factors for this solvent molecule indicate elevated mobility which may explain why it is not observed in the structure of thiosulfate-reduced NiSOD that showed a high average B-factor due to the soaking procedure.

A sulfate-ion from the crystallization liquor is found at the pocket's entrance in all described structures. It was not included in the accessible surface calculation for Fig. 7.9 B since it renders the pocket inaccessible to solvent. Sulfate- and thiosulfate-ions are found in the inside of the hexamer, showing that this space is accessible to molecules of these ions' size. The channels to the hexamer's interior pass through the midpoint between two Ni-sites but do not allow direct contact with the metal or any of its ligands (Fig. 7.9 B).

## 7.5 Accessibility probed by Xenon Binding

The fact that sulfate-ions in all the structures and thiosulfate-ions in the thiosulfate-reduced NiSOD structure are observed in the hexamer's interior reveals the possibility of exchange of small molecules between the exterior and the interior. It also points to structural flexibility between pairs of subunits that form a channel along each twofold symmetry axis (see Figs. 7.1 and 7.9 B) since these three channels show at their narrowest point a diameter smaller than the van der Waals radius of the above ions. Fast movements of subunits relative to each other may allow broadening of the channels for short but sufficient time intervals, making ion exchange between exterior and interior possible. These movements are sometimes termed 'breathing' of the molecule and are the subject of general studies in protein science (see (Fersht, 1999) and references therein).

Sulfate- and thiosulfate-ions are charged particles and will bind to polar sites of the enzyme. They 'probe' the accessibility of hydrophilic patches and thus, a probe for hydrophobic parts can complement the map of accessible sites in NiSOD. Xenon is such a probe since it binds to hydrophobic cavities in proteins as has been observed for example in the case of another Ni-enzyme, the [NiFe]hydrogenase (Montet *et al.*, 1997). Regarding NiSOD, hydrophobic sites are the core of each of the four-helix bundles and certain regions of the subunits' interfaces.

NiSOD was pressurized with xenon gas (section 5.4) and a structure with bound xenon atoms was determined (section 6.5). The nine binding sites per hexamer are shown in Fig. 7.10.

One Xe atom binds inside each channel leading to the hexamer's interior. This

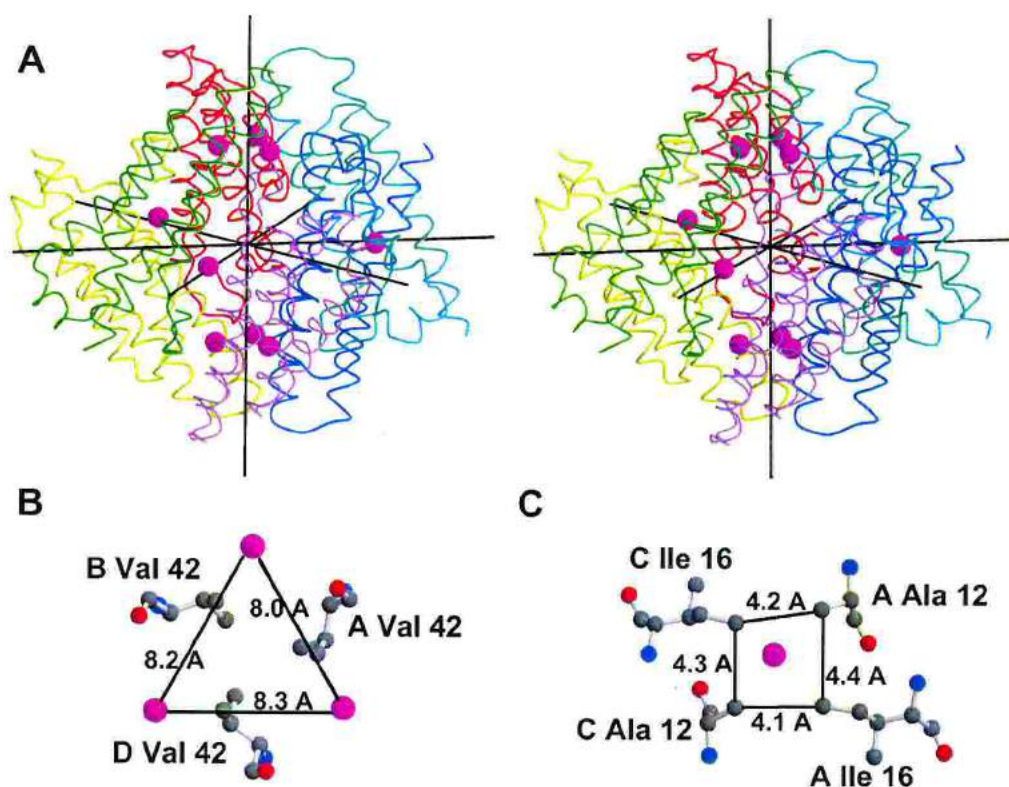


Figure 7.10: Xenon binding sites. The crystal used to obtain this structure was pressurized at 19 bar for 1 min. (A) Stereo view of Xe binding sites in the NiSOD hexamer. One Xe atom is found on each of the three twofold symmetry axis and two Xe triplets are located around the threefold axis (vertical line). (B) A triplet of Xe atoms is found in proximity to Val42 in three subunits. (C) Ala 12 and Ile 16 of either two subunits form a hydrophobic binding site for Xe along the twofold symmetry axes.

confirms the possibility of small molecules to immerse below the hexamer's outer surface as already observed for solvent anions. These latter can reach the inner space whereas Xe atoms do not due to their preference for hydrophobic patches. The observation of Xe triplets extends the number of sites that small molecules can occupy inside the enzyme to those close to the threefold symmetry axis. A channel along the threefold axis, however, does not exist according to calculations of the solvent accessible surface of NiSOD. This indicates once more that considerable flexibility is present between the subunits of NiSOD's hexameric assembly.

## 7.6 Electrostatic Steering to Active Site

Electrostatic steering of substrate to the active site was addressed by calculating the electrostatic potential at the hexamer surface with all His side chains either

double-protonated (corresponding to the structures presented here,  $\text{pH} \approx 5$ , i.e. below the  $\text{pK}_a$  of free histidines) or single-protonated (corresponding to physiological  $\text{pH}$ ) since enzymatic activity is present within the  $\text{pH}$  range of 4-8 (Youn *et al.*, 1996b). Assuming single-protonated histidines, the surface at the entrance to the pocket does not show high potential areas of extensions greater than that produced by a single charged residue (Fig. 7.11).

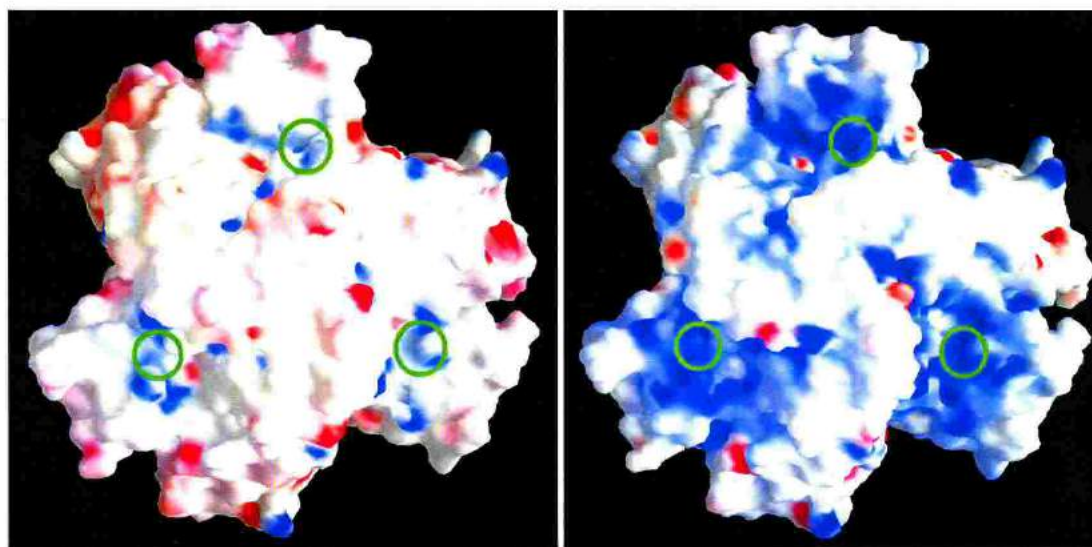


Figure 7.11: Electrostatic potential maps of the surface of NiSOD, prepared with GRASP (Nicholls *et al.*, 1991). Blue corresponds to positive, red to negative potential. Entrances to active site pockets are marked for three of the six subunits by green circles. They are the sites where sulfate-ions bind to the protein surface. (*left*) All His side chains are assumed to be electrically neutral, corresponding to physiological  $\text{pH}$ . (*right*) All His side chains are assigned a charge of  $+1e$  corresponding to the case of crystallization conditions ( $\text{pH} \approx 5$ ), i.e. well below the  $\text{pK}_a \approx 6.2$  of free histidines.

Thus, *long-range* electrostatic steering of superoxide anions to the active site as seen for Cu,ZnSODs (Bordo *et al.*, 2001, and references therein) does not seem present in NiSOD. Assuming double-protonated histidines, the surface of the channel leading to the hexamer's interior and the accessible outer surface closest to each active site become more positively charged (Fig. 7.11 B). It should be noted that the  $\text{pK}_a$  values of individual histidine residues may differ considerably from each other as well as from that of free histidine ( $\approx 6.2$ ) due to differences in the chemical environment. Especially for His 1, a substantial deviation from the free histidine value is expected because its imidazole group is not solvent accessible and the high positive charge of the Ni-ion is present close to it.

Sulfate and thiosulfate ions bound to residues inside the hexamer are likely to reach

their final position via electrostatic attraction by positively charged side chains (His 1, His 53, His 54 and Arg 47) along the channels leading to the inner space.

## 7.7 Inhibited NiSOD

Azide and cyanide ions were used to prepare complexes of inhibited NiSOD. Problems that led to difficulties in the preparation of NiSOD crystals with efficiently bound inhibitors were already pointed out in section 5.3: at the low pH of crystallization, cyanide is present mainly in its protonated form while azide shows much lower enzyme inhibition compared to cyanide (section 4.3). Since NiSOD crystals proved to be very sensitive to increase of pH, an alternative approach was sought using high inhibitor concentrations in soaking procedures.

Nevertheless, resulting electron density maps showed no or only little additional difference density in the pocket at the active site.  $3.5 \sigma F_{obs} - F_{calc}$  density in the interior of the small pocket was observed connecting the amide nitrogen of Asp 3 with the Ni-ion, however, no corresponding  $2F_{obs} - F_{calc}$  density is present at  $1.0 \sigma$ . A  $CN^-$ -ion fitted into the  $F_{obs} - F_{calc}$  density shows 1.92 Å distance to the Asp 3 N and 1.84 Å to the Ni-ion. The presence of a  $CN^-$ -ion is doubtful due to the fact that this  $F_{obs} - F_{calc}$  density appears in only one subunit out of 12 in the asymmetric unit and the lack of  $2F_{obs} - F_{calc}$  density. Although native, thiosulfate-reduced and xenon-pressurized NiSOD structures do not have this additional density feature but show only well-defined density for water molecules (see Fig. 7.9 A), its interpretation as bound inhibitor is not possible.

A possible explanation as to why the inhibitors did not bind to the active site despite their high concentration regards the X-ray-induced reduction of the Ni(III) site in the resting enzyme to a Ni(II) site. This site may not retain the coordination of  $CN^-$  because it results in a square-pyramidal geometry which is atypical for a Ni(II) centre. A dataset was therefore collected in a 'low-dose' manner as described in the context of Ni(III)-coordination by His 1. Imidazole ligation of the Ni-ion was utilized as indicator that the resting enzyme state was present also during data collection. However, no convincing electron density emerged even in the map calculated from these data. Both water molecules are observed at their usual position.

An alternative explanation centres on the sulfate ion at the entrance to the active site pocket (at the position of the arrow in Fig. 7.9 B). It hydrogen-bonds to the amide nitrogen of Gly 7, to the phenolic oxygen of Tyr 9 and to the side chain nitrogen of Lys 64, thereby blocking the access to the pocket's interior. Due to this tight hydrogen-bonding and its at least fivefold higher concentration compared to  $CN^-$ , it is not replaced by cyanide. To circumvent this problem, the precipitating agent ammonium sulfate could be replaced by other salts such as sodium potassium tar-

trate once the crystals have been grown (see (Leonidas *et al.*, 2001) and (Schreuder *et al.*, 1988)). This has not been carried out yet.

## 7.8 NiSOD and Cyanobacteria

Using the sequence similarity search tool BLAST (Altschul *et al.*, 1990), four putative open reading frames (ORFs) of unknown function from cyanobacteria were found to show high homology to NiSOD from *S. seoulensis*. Sequences were aligned using ClustalW (Thompson *et al.*, 1994) and are given in Fig. 7.12 A for *S. seoulensis* (S.seo), *S. coelicolor* (S.coe), *Trichodesmium erythraeum* IMS101 (T.ery), *Synechococcus sp.* WH 8102 (Synec), *Prochlorococcus marinus* subsp. *Pastoris* (P.ma1) and *Prochlorococcus marinus* str. MIT 9313 (P.ma2). The sequence alignment shows that these ORFs contain the His 1-Cys 2-X-X-X-Cys 6 motif involved in Ni-coordination and the conservation of residues Asp 3, Tyr 9 and Arg 39 which are important for NiSOD activity, as they stabilize the active site loop (Table 7.1). Glu 17, however, is not conserved in all ORFs, and its lack is compensated by a concerted mutation at position 47 only in case of *Synechococcus sp* (Fig. 7.12 A).

In addition, the ORFs were analysed by secondary structure prediction using the tool PROF (Rost & Sander, 1993). The ORFs appear to contain the four-helix motif and have conserved all the residues (Tyr 9, Tyr 62, Phe 63, Phe 111, Trp 112) which participate in the stabilization of the N-terminal side of the four-helix bundle by aromatic stacking (Fig. 7.3). The insertion between the first and second helix is located in a loop that is solvent exposed in the hexameric assembly of NiSOD from *S. seoulensis*, and is therefore compatible with the formation of this oligomeric state also in the analysed polypeptides. Most of the residues involved in inter-subunit contacts are either conserved or show a concerted mutation at the corresponding position in the adjacent subunit.

When mapping the per-residue sequence similarity derived from the aligned ORFs onto the subunit structure of *S. seoulensis* NiSOD (Fig. 7.12 B), it becomes visible that the N-terminal part of the four-helix bundle and some residues of the subunit interface are fully conserved. It is therefore predicted that these ORFs are NiSOD, provided that the expression and post-translational processing of N-terminal residues in *S. seoulensis* NiSOD (section 4.2) is feasible also for these polypeptides from cyanobacteria.



# Chapter 8

## A catalytic mechanism for NiSOD

This chapter aims at presenting a picture for the catalytic mechanism of NiSOD even though it can at this stage of analysis neither be a complete nor final one. Experimental facts about the structure are first summarized from the last chapter and discussed in the light of their significance for the function of the enzyme NiSOD. Biochemical results from the literature (section 4.3) are recalled to draw a preliminary picture of NiSOD's catalysis using all the available data. Finally, some questions are posed regarding mechanistic aspects that remained unsolved.

### 8.1 Experimental Information & their Interpretation

#### Chemical identity and geometry of Ni-ligands

The particular ligand field N3S2 (resting state) and N2S2 (reduced state) may be critical to NiSOD's function since redox properties as well as the stability of the high oxidation state (III) in resting NiSOD depend on the type of ligands and the coordination geometry. The fact that  $O_2^{\bullet-}$  is able to reduce and subsequently reoxidize the Ni-centre requires this centre to possess a redox potential in-between those of the couples  $O_2^{\bullet-}/O_2$  and  $O_2^{\bullet-}/H_2O_2$  for optimal turnover, i.e. at approximately 360 mV vs. Normal Hydrogen Electrode. Of importance for NiSOD's catalytic function is the ability of the Ni(II)/(III) redox couple to reach this low potential value by means of the Ni coordination described in section 7.3. Insight into this issue comes from investigations on synthetic small molecule compounds that are aimed at mimicking the metal centre. An effective way to obtain a stable low-potential Ni(III) state is coordination by polarizable anionic ligands (Krüger *et al.*, 1991). In particular, deprotonated nitrogen ligands and/or thiolate ligands were found to achieve stabilization (Hanss & Krueger, 1998) in accordance with the observed ligand field in NiSOD.

### Accessibility of active site atoms

The pockets in the outer surface of the hexamer (Fig. 7.9) represent most likely the place of catalysis. Each pocket is just large enough to host two water molecules in a distance of about 2.8 Å from each other. On one hand, there is space for the substrate  $O_2^{\bullet-}$  and on the other hand, substrate selectivity can be achieved by the pocket's bottleneck which prevents larger molecules from occupying the active site of the enzyme. The sulfate-ion  $SO_4^{2-}$  that is found to hydrogen-bond to residues at the bottleneck is already too large to enter the pocket. Both water molecules are thought to be replaced when superoxide takes up its binding site. The structure of inhibited NiSOD will help to clarify this hypothesis.

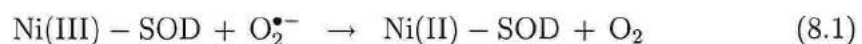
Although thiosulfate reached the proximity of the active site via channels to the hexamer's interior (Fig. 7.9B), the substrate is not expected to occupy the same site for catalysis due to its greater distance (7-8 Å) from the Ni-ion. In order to verify this assumption, a suitable mutation (e.g. Ala 12 to Val, see Fig. 7.10) could be designed to block the channels and subsequently record the enzyme's activity.

The Ni-ion and its ligands do not show solvent accessibility except for the small area of 1.1 Å<sup>2</sup> for His 1 N. It should be noted that this result was derived from the static structures and structural flexibility of the protein (especially upon substrate approach to the active site) was not considered in accessibility calculations. Based on these accessible areas, only an outer sphere electron transfer between the superoxide anion and the Ni-ion can be suggested.

Both S-ligands are protected from direct contact with substrate or product molecules, preserving the thiolate ligands from oxidation by  $O_2^{\bullet-}$ . Ni-thiolate complexes, such as the active site in [NiFe]-hydrogenase, are known targets of damage by superoxide. The inaccessibility of the S-ligands thus reconciles the apparent implausibility of a Ni-thiolate complex as an agent of protection against oxidative stress.

### Proton conduction

NiSOD is believed to act like other SODs according to the formal equations of the dismutation reaction,



where Ni(III)-SOD and Ni(II)-SOD represent the oxidized and reduced metal centre

in NiSOD. According to this reaction, two protons are required in the second step to form hydrogen peroxide. The structure of NiSOD points to some residues in the vicinity of the metal centre as potential proton donors. Assuming that superoxide approaches the Ni(II) through the small pocket, it may pick up one or both  $H^+$  from main chain nitrogen atoms (Asp 3 or Cys 6) of the active site loop (Fig. 7.9 A). At the entrance of the pocket, Tyr 9  $O\eta$ , Lys 64  $N\zeta$  or water molecules of the protein's hydration shell are available  $H^+$ -donors. Another scheme for proton-donation has been proposed for Cu,ZnSOD (Hart *et al.*, 1999). According to this,  $O_2^{\bullet-}$  obtains one  $H^+$  from a water and simultaneously an  $H^+$  from the Cu- and Zn-ion bridging His 61 (bovine Cu,ZnSOD numbering, Fig. 3.2) upon re-establishing ligation to the Cu-ion which was broken after reduction of the Cu-ion. A similar scheme may be present in NiSOD as the His 1  $N\delta$  ligation is broken in the reduced form and thus has to be re-established to obtain the initial enzyme state. The distance between the proton at  $N\delta$  and a possible  $O_2^{\bullet-}$  binding site inside the accessible pocket is about 4 to 5 Å.

#### A functional role for Tyr 9

The existence of Tyr 9 at the entrance of the pocket about 5.5 Å away from the Ni-ion (Fig. 7.9) is interesting since all known Mn- and FeSODs contain a strictly conserved Tyr 34 (*E. coli* numbering) at the gateway to the active site, with Tyr  $O\eta$  distances between 5.2-5.5 Å from the metal ion (Edwards *et al.*, 2001). This residue has been implicated in playing an important role in the catalytic fine-tuning of these SODs, based on its proximity to the metal centre and its involvement in a conserved hydrogen-bonding pattern in the active site. The role of Tyr 9 in NiSOD may be similar to that of Tyr 34 in Fe- or MnSOD with respect to redox tuning but differences are to be expected regarding proton transfer. This is due to an important structural difference between the active sites of NiSOD and Mn- or FeSOD: in NiSOD there is no conserved glutamine (Gln 69 in FeSOD or Gln 146 in MnSOD, Fig. 3.4) which bridges the tyrosine to *metal-coordinated solvent* in Fe- and MnSOD and involves in this way the second coordination sphere of the metal ion in proton transfer. Moreover, the disruption of hydrogen-bonds formed by the phenolic oxygen of Tyr 9 after mutation to phenylalanine in NiSOD does not lead to complete loss of activity but to a small reduction of only 18% (Table 7.1). This indicates that the hydrogen-bonding network centred around Tyr 9  $O\eta$  is not critically disrupted upon mutation of Tyr 9 to Phe. The role of Tyr 9 in NiSOD rather appears to be in subunit stabilization by participating in an aromatic stacking at the N-terminal side of the four-helix bundle. This is confirmed by mutations to non-aromatic residues (Table 7.1) which is accompanied by inactivation of the enzyme. Additionally, Tyr 9 helps in

shaping the bottleneck at the entrance to the small pocket that is believed to be the substrate binding site and thus in conferring substrate selectivity to small molecules.

### **Electrostatic surface properties**

The ionic strength dependence of catalytic activity is regarded as a measure of electrostatic attraction of substrate to the active site because the higher the ionic strength of the solution is the more the positively charged active site will be screened. The lack of an extended positive surface potential in the environment of the active site is in accordance with the small ionic strength dependence of the catalytic rate constant for NiSOD (Choudhury *et al.*, 1999), confirming the interpretation that electrostatic steering of the substrate to the catalytic centre is not an important aspect for NiSOD.

## **8.2 Open Questions**

A question concerning the catalytic rate constant arises when the above findings of a small active site accessibility and lack of electrostatic attraction are combined: how to explain the high catalytic rate of NiSOD ? As it is on the same high level as that of Cu,ZnSOD which utilizes long-range electrostatic attraction to its active site one may ask which feature in NiSOD may compensate for the lack of this facilitating property.

Another point centers about the path and the final site of the substrate molecule  $O_2^{\bullet-}$ . Is the small pocket in the outer surface of the hexamer the only possible site and where does the superoxide anion bind ? At His 1 N which is the only ligand with an accessible area  $> 0$  ? Are the channels to the interior important for substrate (or  $H^+$  donor) conductance ? These questions were started to be addressed by structural studies using the inhibitors cyanide and azide and are still ongoing.

Finally, is the rotation of His1 imidazole in the transition between the enzyme's resting and reduced state involved in proton donation to superoxide in the second step of the dismutation reaction ? The actual importance of various potential  $H^+$  donors has still to be investigated.

## Chapter 9

# Structural & Functional Comparison

Part of the interest in studying NiSOD comes from the possibility to compare its structure to other proteins with the aim to find common features and to link these features to function. A lot may be learned about NiSOD (and the proteins compared to NiSOD) once the rationale behind common features is understood. In the next section, NiSOD is compared to the other superoxide dismutase classes and then confronted with other enzymes which utilize nickel in catalysis.

Before, however, the NiSOD subunit structure is used to search for structurally similar proteins (or protein fragments) in the Protein Databank (PDB). Two web-based tools were employed which apply different methods to compare structures: the DALI server (Holm & Sander, 1996) aligns fragments of the search structure (here the four-helix bundle of a NiSOD subunit) to obtain the best superposition to databank structures (so-called local alignment). The PRIDE server (Carugo & Pongor, 2002) compares two structures based on their similarity regarding distances between atoms in residue  $x$  and  $x + n$ , where  $n$  runs from 1 to 20.

Using the DALI server, the highest structural similarity in a local alignment was observed for a four-helix bundle from the M-fragment of  $\alpha$ -1 catenin (PDB code 1H6G) yielding a root mean square (rms) coordinate deviation of 106 residues of 2.5 Å and 8% sequence identity. The PRIDE server yields highest similarity to the cytochrome  $c'$  subunit from *Rhodobacter capsulatus* (PDB code 1RCP). DALI reports a rms coordinate deviation of 100 locally aligned residues of 3.1 Å and 11% sequence identity for this cytochrome  $c'$ . Both proteins are functionally unrelated to NiSOD. Cytochrome  $c'$  which is involved in electron transport might be linked remotely to a superoxide dismutase since the main location of both proteins in the cell is where oxygen is used in the respiratory chain. More likely, however, is that Nature used the four-helix bundle as scaffold to perform several unrelated tasks as

other often encountered motifs, such as the immunoglobulin domain.

## 9.1 NiSOD compared to other SOD Classes

NiSOD is structurally fully unrelated to other superoxide dismutase classes, i.e. the Cu,ZnSOD class and the Mn-/Fe-SOD class that were described in chapter 3. Neither the oligomeric state of NiSOD, a homohexamer, nor the four-helix bundle subunit structure is found in any of the other two classes. It is interesting to note that Nature has invented three different enzyme classes to perform the same reaction, the dismutation of superoxide.

Regarding SOD activity, it is apparent from the high catalytic rate constant of about  $10^9 \text{ L mol}^{-1} \text{ s}^{-1}$  of *all* SODs that the four transition metals Cu, Mn, Fe and Ni are equally suited to carry out the one-electron redox cycle (see equations 3.1 and 3.2). One may therefore ask which properties these transition metals and their respective ligand environments have in common. This can help to identify the features which are indispensable for an enzyme to perform the superoxide dismutation. In addition, one has to analyse the influence of residues outside the first coordination shell of a transition metal on the overall catalytic power of a SOD, concerning for example generation of substrate specificity, electrostatic guidance of  $\text{O}_2^{\bullet -}$  to the metal centre, fine-tuning of redox properties,  $\text{H}^+$  conduction in the second half of the dismutation reaction, etc.

One of the common features of SODs has already been mentioned in section 3.1: the relatively low redox potential of the metal centre of about 0.3 V vs. NHE\*. The way this feature is realized does not only depend on the type of transition metal but includes the influence of atoms in the first coordination shell and possibly even beyond. Therefore, the fact that metal coordination by sulfur ligands in NiSOD is unique among known SODs should be considered in close relation to the presence of the Ni-ion.

Electrostatic guidance of superoxide to the active site of Cu,ZnSOD and also for MnSOD and FeSOD has been suggested based on the electrostatic potential map of the enzyme's surface and on the dependence of the catalytic rate on ionic strength of the solvent. NiSOD appears to be an exception or at least, the *long-range* character of this facilitation means is less pronounced. This finding correlates well with the dependence of the catalytic rate constants on ionic strength, see Fig. 4.3.

---

\*Reported redox potentials are 0.40 V for Cu,ZnSOD, 0.26 V for FeSOD and 0.31 V for MnSOD, see (Holm *et al.*, 1996) and references therein.

For Cu,ZnSOD, an inner sphere electron transfer in the reduction step and outer sphere electron transfer in the reoxidation step was proposed (Hart *et al.*, 1999). This was based on interpretation of structures of native, inhibited and O<sub>2</sub>-pressurized enzyme. In case of MnSOD and FeSOD, details of the mechanism and the reasons for metal ion specificity of almost identical active sites in these two enzymes is still under debate (Maliyekal *et al.*, 2002). The situation in NiSOD differs from other SODs due to the lack of a solvent molecule coordinating the metal. For NiSOD, an outer sphere transfer in both reaction steps seems the more likely mechanism. This results from interpretation of the atomic accessibility areas alone since inhibitor studies are not yet available.

## 9.2 NiSOD compared to other Ni-containing Enzymes

Only a small number of Ni-containing enzymes is known to date. Before 1975, when the first of these enzymes was shown to rely on nickel (urease, (Dixen *et al.*, 1975)), no biological relevance was attributed to the element Ni. Since then, at least six other enzymes were found to contain nickel: the hydrolytically active glyoxalase I from *E. coli*, and the redox-active enzymes [NiFe]-hydrogenase (Volbeda *et al.*, 1995), methyl coenzyme M reductase (Ermler *et al.*, 1997), CO dehydrogenase (Dobbek *et al.*, 2001) and acetyl-CoA synthase, (Doukov *et al.*, 2002) and (Darnault *et al.*, 2003). All these enzymes occur in microbial organisms. Several reviews about the biochemistry of Ni-containing enzymes were published: (Maroney *et al.*, 1998), (Ragsdale, 1998), (Ermler *et al.*, 1998), (Maroney, 1999) and (Mulrooney & Hausinger, 2003). A schematic representation of the active site in some of these enzymes is compiled in Fig. 9.1 and Table 9.1 lists the reactions they catalyse together with entry codes of structures in the Protein Databank (PDB).

Table 9.1: Reactions catalysed by Ni-containing Enzymes

Enzyme	Catalysed Reaction	PDB codes
Urease	$\text{H}_2\text{N-CO-NH}_2 \rightarrow 2 \text{NH}_3 + \text{H}_2\text{CO}_3$	2KAU, 2UBP
NiFe hydrogenase	$2 \text{H}^+ + 2 \text{e}^- \rightleftharpoons \text{H}^+ + \text{H}^- \rightleftharpoons \text{H}_2$	2FRV, 1FRF
Methyl CoM reductase	$\text{CH}_3\text{-CoM} + \text{CoB-SH} \rightarrow \text{CH}_4 + \text{CoM-S-S-CoB}$	1MRO, 1E6V
CO dehydrogenase	$\text{CO} + \text{H}_2\text{O} \rightleftharpoons \text{CO}_2 + 2 \text{H}^+ + 2 \text{e}^-$	1JJY, 1JQK
Acetyl-CoA synthase	$\text{CH}_3\text{-CoFeSP} + \text{CO} + \text{CoA} \rightleftharpoons \text{acetyl-CoA} + \text{CoFeSP}$	1MJG, 1OAO
Superoxide Dismutase	$2 \text{O}_2^{\bullet -} + 2 \text{H}^+ \rightarrow \text{O}_2 + \text{H}_2\text{O}_2$	see Table 6.5

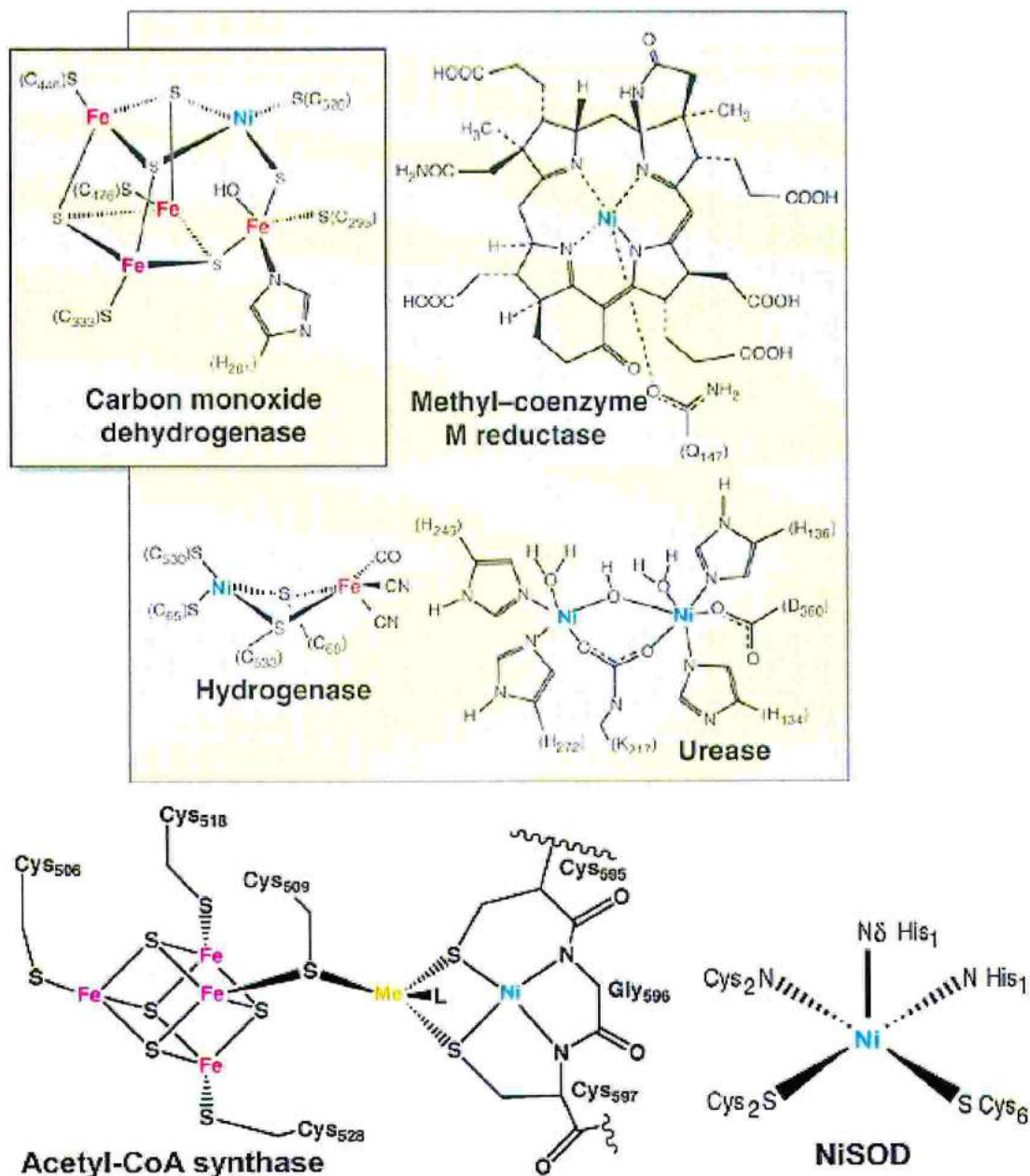


Figure 9.1: Schemes of active sites in Ni-containing enzymes. A variety of active site geometries is used in reactions that rely on nickel, including homo- and hetero-bimetallic sites as well as incorporation in iron-sulfur clusters. The type of metal bridging the Fe-S cluster to the square-planar Ni(II)-site in Acetyl-CoA synthase is still controversial. NiSOD employs a less complex metal centre consisting of a single Ni-ion which cycles between the oxidation states III and II. The upper panel was taken from (Thauer, 2001).

**Urease** catalyses the hydrolysis of urea to carbamate and ammonia in the final step of organic nitrogen metabolism in plants and microbes. The increase of pH accompanied by urea hydrolysis in bacteria is the major cause of negative side effects by urease activity both on human and animal health and in agriculture (see (Benini *et al.*, 2000) and references therein). *Bacillus pasteurii* urease has a dinuclear Ni site where each Ni(II) is coordinated by an oxygen atom from a Ni-bridging carbamylated lysine, two His side chains and the oxygen of a bound water. The second Ni site Ni(2) is additionally coordinated by the carboxyl group of an aspartic acid residue. This results in a distorted square-pyramidal coordination for Ni(1) and in a distorted octahedral coordination for Ni(2).

**[NiFe]hydrogenase** catalyses the redox chemistry of molecular hydrogen. In anaerobes, H<sub>2</sub> is used as energy source whereas in fermentation H<sub>2</sub> is produced. This enzyme occurs in archaea, bacteria and also eukaryotes. Besides the [NiFe]hydrogenases, there are enzymes containing only iron or no metal in the active site (Fontecilla-Camps *et al.*, 1997). The Ni-ion is tetrahedrally coordinated by four sulfurs of Cys residues, two of which bridge the Ni site to the Fe site.

**Methyl CoM reductase** is the enzyme of the final step in methane formation in methanogenic archaea. The Ni site is octahedrally coordinated by the Ni-cofactor F430 (tetrahydroporphinoid prosthetic complex), an amino acid side chain (Gln Oε1) and a thiol or sulfonate group of Coenzyme M depending on the oxidation state of the metal centre. Factor F430 binds non-covalently in an equatorial plane by four nitrogen atoms to the Ni-ion.

**CO dehydrogenase** is responsible for CO metabolism in microorganisms, using CO as the only carbon and energy source by oxidizing it to CO<sub>2</sub>, and is found in aerobic carboxidotrophic bacteria, in phototrophic anaerobes such as *Rhodospirillum rubrum* (Drennan *et al.*, 2001), in anaerobic acetogenic bacteria, methanogenic archaea, hydrogenogenic bacteria and sulfate-reducing archaea and bacteria (see (Dobbek *et al.*, 2001) and references therein). Two classes of CO dehydrogenases were defined; those from aerobic bacteria containing a Mo-[2Fe-2S]-FAD cluster and those from anaerobic bacteria containing a Ni-[4Fe-4S] cluster. The anaerobic bacterium *Carboxydotherrmus hydrogenoformans* was found to contain a Ni-[4Fe-5S] cluster (Dobbek *et al.*, 2001). In aerobic bacteria, the CO dehydrogenase activity exists separately, i.e. as the only enzyme function, and in some of the anaerobic bacteria it is present together with an acetyl-CoA synthase activity.

The Ni-ion is coordinated by four sulfur ligands with a tetrahedrally distorted square planar geometry. Only one S-donor stems from an amino acid while the

other three are part of the Ni-[4Fe-5S] cluster.

**Acetyl-CoA synthase** activity occurs as one of the activities in the bifunctional enzyme CO dehydrogenase/acetyl-CoA synthase. The overall function of this enzyme in acetogenic bacteria is the conversion of CO<sub>2</sub> to acetyl-CoA. It uses the CO dehydrogenase activity to reduce CO<sub>2</sub> to CO which is subsequently used together with coenzyme A and a cobalt-containing corrinoid iron-sulfur protein (CoFeSP) to assemble acetyl-CoA. Instead, its function in methanogenic archaea is to degrade acetyl-CoA in order to obtain CO<sub>2</sub> and methane.

**Other enzymes** that depend on Ni are glyoxalase I from *E. coli*, acireductone dioxxygenase from *Klebsiella pneumoniae* and methylenediurease from *Burkholderia* species. The latter two were found more recently and are structurally not yet well characterized (Mulrooney & Hausinger, 2003).

Apart from these enzymes, other proteins bind nickel in a purposeful manner. They are involved in storage or transport of nickel or help to incorporate it into the enzymes mentioned. These proteins were reviewed e.g. in (Maroney, 1999), (Watt & Ludden, 1999) and (Mulrooney & Hausinger, 2003).

Metal coordination by sulfur ligands is common in redox-active Ni-containing enzymes. S-ligands in NiSOD confirm the suggestion that thiolate ligation represents a requirement for the function of redox-active Ni-centres at physiological redox potentials based on the fact that among Ni-containing proteins investigated so far only redox-active enzymes feature thiolate ligation but neither does the hydrolytically active urease and *E. coli* glyoxalase I nor do auxiliary proteins for Ni-related cellular tasks (Maroney, 1999).

Ni-coordination by backbone N atoms (one amino-terminal and one amide group N atom in NiSOD) is uncommon in proteins, but examples exist with short peptides (see references in (Maroney *et al.*, 1998)). Very recently it was found in the active site (A-cluster) of the bifunctional CO dehydrogenase/acetyl-CoA synthase, see (Doukov *et al.*, 2002) and (Darnault *et al.*, 2003). The acetyl-CoA synthase shows a Cys-Gly-Cys motif in which two Cys side chains and two backbone amide N atoms coordinate Ni(II) in square-planar geometry. Interestingly, this Ni(II) is thought to be redox-inactive although its N<sub>2</sub>S<sub>2</sub> ligand field is similar to that of redox-active Ni(II) in reduced NiSOD. The Ni-ion is part of a [Fe<sub>4</sub>-S<sub>4</sub>]-Me-Ni cluster with still controversial nature of the bridging metal Me (Hausinger, 2003). First evidence was presented for a copper ion (Doukov *et al.*, 2002) but in a subsequent investigation by another group, a Ni-ion was proposed at this site (Darnault *et al.*, 2003).

# Chapter 10

## Conclusions

Superoxide dismutases (SODs) are the frontline defence against oxidative stress which stems from the damaging effect of reactive oxygen species. SODs remove the superoxide radical  $O_2^{\bullet-}$ , the first radical generated in the chain of reductions from  $O_2$  to  $H_2O$ , from cells of aerobic organisms. The nickel-containing superoxide dismutase, NiSOD, was suggested to represent a novel class of the SOD family besides the well-characterized classes of Cu,ZnSOD and Mn-/Fe-SOD. NiSOD was isolated from a variety of *Streptomyces* species. *Streptomyces* are aerobic filamentous bacteria which are found ubiquitously in the soil.

NiSOD from *Streptomyces seoulensis* was crystallized in several crystal forms for structural investigations. Two of these crystal forms diffracted to better than 1.7 Å resolution at synchrotron radiation sources. In one of them, purely translational non-crystallographic symmetry was present which caused difficulties in the solution of the crystallographic phase problem. The other crystal form instead was used successfully to solve the NiSOD structure by the multiple wavelength anomalous dispersion method exploiting anomalous scattering at the K-edge of Ni. NiSOD proved to be sensitive to X-ray induced reduction of its metal centre in the course of diffraction data collection. As a consequence, the structure of the resting enzyme state had to be inferred from data obtained after minimal exposure to X-rays. At the same time, sensitivity to absorbed X-ray doses allowed the utilization of X-ray induced reduction as a means of visualization of intermediate states between the resting and fully reduced state. The latter state was also produced by soaking of NiSOD crystals in a solution containing the reducing agent thiosulfate.

NiSOD is found to be distinct from SODs of both other classes regarding oligomeric state, subunit structure and active site. It is a homohexamer of four-helix-bundle subunits where each subunit hosts an active site in an N-terminal loop. This loop is conformationally stabilized by hydrogen-bonds of some of its residues to residues from two neighbouring subunits, as confirmed by mutagenesis studies.

---

In the resting enzyme, the Ni(III) is five-coordinate in a square pyramidal geometry by the amino-group and imidazole N $\delta$  nitrogen of His 1, the amide nitrogen and thiolate sulfur of Cys 2 and the thiolate sulfur of Cys 6. The fully reduced enzyme state shows square-planar geometry. Loss of the axial ligand His 1 N $\delta$  is observed upon reduction to a formal Ni(II)-centre. An intermediate state of His 1 imidazole rotation around the C $\beta$ -C $\gamma$  bond was captured after application of an X-ray dose in-between those used in data collections for the resting and reduced enzyme state. The N $\delta$  atom is found at hydrogen-bonding distance to the carbonyl oxygen of Val 8 after its ligation to the Ni-ion is broken. Since N $\epsilon$  remains in the conformation of hydrogen-bonding to Glu 17 and Arg 47 from an adjacent subunit, it is supposed that in the reduced state His 1 is double-protonated. This would correspond to the protonation state expected from the pH  $\approx$  5 at which the crystals were grown.

The metal centre is located at the bottom of a small pocket in the outer surface of the hexamer. The pocket is formed with the help of the coplanar backbone nitrogen atoms of His 1, Asp 3, Cys 6 and Gly 7 as well as with the participation of the side chains of Pro 5 and Tyr 9 which create a bottleneck at its entrance. Substrate specificity is likely to arise from the shape of this pocket which is thought to be the place of superoxide binding during catalysis. The pocket's volume is just sufficient to contain two solvent water molecules with a distance of about 2.8 Å. Its bottleneck prevents larger anions from entering as can be concluded from the sulfate-ion of the crystallization liquor that sits at the entrance to the pocket. Neither the Ni-ion nor its ligands except His 1 N appear solvent accessible indicating an outer-sphere electron transfer between the superoxide radical and the redox-active metal. H<sup>+</sup> donors needed in the second step of the dismutation reaction may be the backbone nitrogen atoms within the pocket, the phenolic oxygen of Tyr 9 or water molecules in the enzyme's hydration shell.

The electrostatic potential at the pocket's entrance does not suggest the presence of long-range electrostatic attraction of superoxide anions to the positively charged active site as it is observed for Cu,ZnSOD. This is in accordance with the observed ionic strength dependence of these enzymes' catalytic rate constants but raises the question how their equally high catalytic rate can be reconciled with the different importance of substrate guidance to their active site.

The coordination environment of Ni in NiSOD is distinct from that in other Ni-dependent enzymes. Most particular are the presence of both the relatively high oxidation state (III) of the Ni-ion in resting NiSOD and the use of backbone nitrogen atoms in ligation. The presence of thiolate ligands, however, is found exclusively and commonly among those Ni-enzymes that show redox function, suggesting an important role of these ligands in the redox properties of their metal centre.

# Appendix A

## Protein X-ray Crystallography

### A.1 Protein Crystallization

Theoretical and practical considerations about preparing protein crystals are given in this section. For more detailed informations, see e.g. the books (McPherson, 1999) or (Ducruix & Giegé, 1999) from which the following notes were taken.

#### General aspects

Crystallization of molecules is a multiparametric process and can be divided into the steps of nucleation, growth and growth end. Practical problems do not only result from the large number of physical, chemical and biological parameters important to control crystallization but mainly from the inherent conformational flexibility of biological molecules. Further difficulties arise from the requirement that the protein is of high purity as contaminants can disturb the nucleation and/or growth process and that the protein is stable under the physico-chemical conditions of crystallization. Enzymes are in this respect usually well-behaving molecules.

To grow crystals from a molecule, this molecule has to be brought in a thermodynamically unstable, supersaturated state that may result in either a crystalline or amorphous phase upon return to a state of equilibrium. *Supersaturation* can be achieved by slow evaporation of the solvent or by varying in time one or more parameters of crystallization. *Solubility* of the biomolecule is of major importance in controlling crystallization. It is defined as the concentration of the solute (here, the biomolecule) in the crystallization solution when the molecules are in equilibrium with the crystal form at a given temperature, pH value and concentrations of all other compounds (water, buffer, crystallizing agent, additives). Solubility thus depends on the solvent (pH, ionic strength, dielectric constant, concentration and type of compounds) but also on the protein itself (hydrophilicity, net charge, type of solvent exposed residues). The level of supersaturation is specified by the ratio of

the actual protein concentration over the solubility value and its various zones are represented schematically in Fig. A.1.

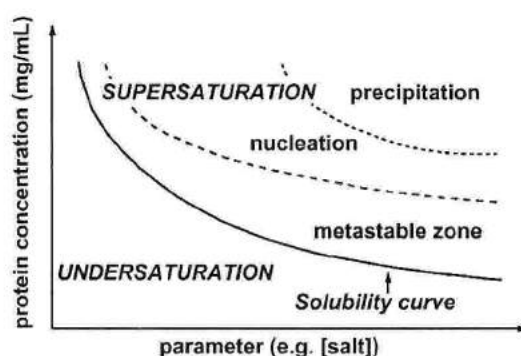


Figure A.1: Scheme of a two-dimensional solubility diagram. The solubility is given as a function of one crystallization parameter, with all other parameters kept constant. The solubility curve separates the under- and supersaturated zones. It corresponds to the situation at the end of crystal growth where the biomolecule solution is in equilibrium with the crystallized molecules. Below the curve, the system is in a stable undersaturated state and crystals will never grow. Above the curve, the different zones of supersaturation are shown. The excess of molecules in solution will appear as a solid phase until the concentration drops down to the solubility value. Sometimes the excess of molecules may appear in oily drops in a liquid-liquid phase separation.

*Precipitation* occurs at very high levels of supersaturation ( $\approx 30$  times the solubility value or more). In short time, the excess molecules separate from the solution in an amorphous state.

*Nucleation* occurs at supersaturation levels around 10 times the solubility value and appears either as homogeneous or inhomogeneous crystalline precipitation (the first being preferred since the latter is often induced by vibrations or particles like dust). Crystals form faster and in larger numbers of small (micro-)crystals with increasing supersaturation in the nucleation zone. The nucleation rate is defined as the number of nuclei formed per unit volume and unit time, and should not be too high in order to allow growth of few but large crystals. The advantage to have a wide nucleation zone in terms of successful ranges for parameters (e.g. [crystallizing agent]) is given if the solubility value is high since then the nucleation rate increases only slowly with increasing supersaturation. It is not always easy to distinguish amorphous from crystalline precipitation by looking at it under the microscope. To obtain a clear distinction one can centrifuge away the solution and set up a crystallization trial with the precipitate instead of fresh protein: the amorphous precipitate will dissolve whereas the microcrystals will grow.

In the *metastable zone*, the critical supersaturation is not yet reached which means

that spontaneous nucleation is not possible unless induced by vibrations, dirt particles or other ways. This zone is large when the solubility value of a given crystallization condition is low, making it difficult to reduce the nucleation rate and to obtain few but large crystals. When conditions at high solubility values do not work for the biomolecule of interest, the technique of *seeding* can be a solution to the problem. There, the metastable zone is used to 'seed' the microcrystal or the small macrocrystal into it (giving rise to the technique of *microseeding* or *macroseeding*). The crystals grow fed by the molecules in the metastable zone of the system to which they are transferred.

*Protein-protein interactions* that finally lead to the formation of a protein crystal can be divided into a long-range and short-range interaction. The long-range interaction is the net result of an electrostatic repulsion of the charged protein molecules (unless the solvent's pH equals the protein's pI) and a van der Waals attraction. Long-range interaction is not specific for the protein's shape and its surface-exposed residues and thus, even in the case of an attractive net interaction, is not sufficient for crystal growth but may also lead to amorphous precipitation. In contrast, the short-range interaction promotes specific and periodic intermolecular contacts needed to build the crystal. Protein contacts are due to polar interactions (hydrogen-bonds), hydrophobic interactions (van der Waals contacts) and salt-bridges.

The crystallizing agent that acts on the solubility of the protein is most often a salt or polyethylenglycol (PEG). Their effect is to immobilize water which results in an apparent increase of the protein concentration. Salt determines the ionic strength of the solvent which is defined as

$$I = \frac{1}{2} \sum_i C_i Z_i^2 \quad (\text{A.1})$$

where  $C_i$  is the concentration of the salt and  $Z_i$  is the valency of each ion  $i$ . For a solution of 0.1 M ammonium sulfate,  $(\text{NH}_4)_2\text{SO}_4$  one obtains\*

$$I = \frac{1}{2} (2 \times [\text{NH}_4^+] \times 1^2 + [\text{SO}_4^{2-}] \times 2^2) = 0.3 \text{ M.}$$

Ionic strength modifies the electrostatic interactions between the macromolecules: at increased ionic strength, more ions are present which screen their net charge and reduce the electrostatic repulsion. Consequently, effects of electrostatic

---

\*For salt concentrations above 0.2 M, the concentration  $C_i$  should be corrected by the chemical activity coefficient and, if a salt of a weak acid or base is used,  $C_i$  must be calculated depending on the pH of the solution with respect to the  $\text{pK}_a$ .

protein-protein interaction are predominant at low salt concentrations and those of hydrophobic interaction at high salt concentration. The phenomenon of decreased or increased solubility with increasing ionic strength is called '*salting-out*' or '*salting-in*', respectively. The type of salt is an important parameter as well, because two salts of equal concentration and valency of their ions may still vary in size and polarizability of these ions. The *Hofmeister series* rank salt ions according to their protein precipitation ability. Sulfate ions are found to reinforce the structure of water and biomolecules and at the other end of the series, ions as chloride and thiocyanate tend to denature biomolecules. Another critical parameter is the pH of the crystallization solution. pH influences the solubility as it decides on the net charge of the protein in dependence on its isoelectric point (pI). Solubility shows a minimum at the pI where it is also independent on ionic strength. The type of compound that is used to buffer a solution at a certain pH has to be considered as an additional parameter.

The solubility behaviour of a given biomolecule can so far not be determined theoretically and so it has to be found experimentally. A very simple way to get a first idea is to scan a range of crystallizing agent concentrations and analyse the response of the molecule. In practice, however, phase diagrams are not always set up systematically and instead, mutually unrelated premixed crystallization solutions (so-called '*sparse matrix*' kits) are used for initial screening of successful conditions to grow crystals (Jancarik & Kim, 1991).

### **Crystallization by the vapour diffusion method**

Two experimental set-ups are commonly in use, the sitting drop and the hanging drop set-up, see Fig. A.2. The principle of vapour diffusion crystallization consists of equilibrating a drop containing the biomolecule, crystallizing agent and maybe other compounds against a large reservoir containing the crystallizing agent in higher (most often double) concentration than the drop does. The equilibration process proceeds by diffusion of the volatile constituents (water or organic solvents) until vapour pressure in the drop equals that of the reservoir leading to a decrease of the drop volume and an increase of the concentration of all non-volatiles, including the biomolecule. Thus, supersaturation can be temporarily reached to which the biomolecule will respond in a manner depending on the properties of the crystallization solution in the drop and external parameters, such as the temperature.

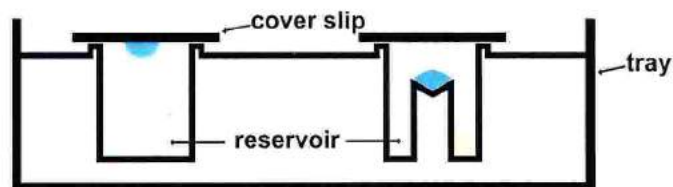


Figure A.2: Set-up of a hanging-drop (*left*) and sitting-drop (*right*) vapour-diffusion crystallization experiment. A drop of ca. 2-5  $\mu\text{L}$  on a glass plate (cover slip) is mixed containing one part of protein solution and one part of the 'reservoir' solution which is present in large excess (ca. 0.7-1.0 mL) at the bottom of the well and contains the crystallizing agent, a buffer and possibly other additives that may influence crystallization. The well is closed and sealed with vacuum grease to prevent vapour exchange between interior and exterior. The cover slip is siliconized to avoid movements of the drop upon putting it upside down in the hanging drop set-up.

## A.2 Steps in Crystal Structure Determination

This section gives a brief introduction to collection of X-ray diffraction data and the computational steps applied in the flow of data from the raw diffraction images to the final refined atomic coordinates. Further information can be taken from textbooks such as (Drenth, 1999) or the International Tables for X-ray Crystallography (Rossmann & Arnold, 2001).

With X-ray crystallography it is possible to determine the three-dimensional structure of a biomolecule, i.e. to do microscopy with atomic resolution. A difference to microscopy with visible light is that the picture of the object is not a real space picture, but a picture in a mathematical space (so-called '*reciprocal space*') which has to be transformed with the help of a computer to the real space picture. Fig. A.3 illustrates the principle set-up of an X-ray diffraction data collection.

The reason why the immediate result of the diffraction experiment is in reciprocal space (coordinates  $h, k, l$ ) and not in real space (coordinates  $x, y, z$ ) comes from the fact that conventional lenses to focus the diffracted waves onto an image plane do not exist due to a fundamental property of X-rays, the refractive index very close to one. Thus, the Fourier transform of the (intermediate) reciprocal space image to the (final) real space image has to be done computationally instead of optically. What is recorded on the detector,  $I(h, k, l)$ , yields the absolute square of the quantity  $\mathbf{F}(h, k, l)$ , the so-called *structure factor*, which in turn is related to the desired output of X-ray crystallography, the distribution of the molecule's electron

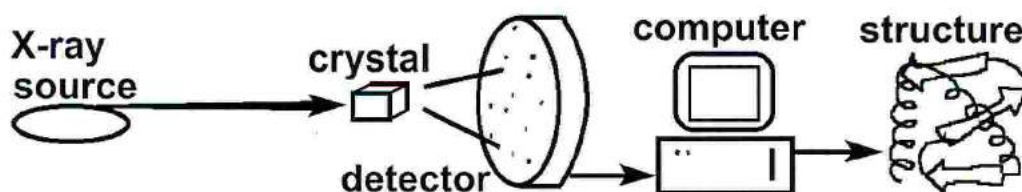


Figure A.3: Schematic set-up of an X-ray diffraction experiment. The X-ray source to the left produces the monochromatic X-ray beam with a cross section similar in size to the crystal which diffracts X-ray waves to different spots on the detector. The crystal is continuously rotated around an axis perpendicular to the beam direction and, at a given rotation angle, only those Bragg-planes (characterized by three indices  $h, k, l$ ) contribute to the diffraction pattern that fulfill the Bragg-equation (see text). After about 0.2 to 2° rotation of the crystal, an image of the diffraction pattern is stored and the collection of a new image can begin. A computer is used to derive from the total of images a table of diffraction spot intensities as a function of the indices, i.e.  $I(h, k, l)$ . By methods explained in the text, the real space picture of the molecule can then be derived.

density  $\rho(x, y, z)$ :

$$I(h, k, l) \sim |\mathbf{F}(h, k, l)|^2 \quad \text{where} \quad (\text{A.2})$$

$$\mathbf{F}(h, k, l) = \sum_{j=1}^N f_j \exp[2\pi i(hx_j + ky_j + lz_j)] \quad \text{and also} \quad (\text{A.3})$$

$$\mathbf{F}(h, k, l) \equiv |\mathbf{F}(h, k, l)| \exp(i\alpha_{hkl}) = FT[\rho(x, y, z)] \quad (\text{A.4})$$

$$= V \int_x \int_y \int_z \rho(x, y, z) \exp[2\pi i(hx + ky + lz)] dx dy dz \quad (\text{A.5})$$

$$\rho(x, y, z) = \frac{1}{V} \sum_{hkl} |\mathbf{F}(h, k, l)| \exp(i\alpha_{hkl}) \exp[-2\pi i(hx + ky + lz)] \quad (\text{A.6})$$

$V$  is the volume of the crystal's unit cell,  $f_j$  is the atomic form factor or *scattering factor* of atom  $j$  in the unit cell and  $\alpha_{hkl}$  is the phase which got lost upon recording the intensities on the detector. Without these phase angles, the Fourier transform in A.6 cannot be computed, giving rise to the '*phase problem*': only part of the necessary information for  $\rho(x, y, z)$  is available with the intensity  $I(h, k, l)$  of each diffraction spot, namely the magnitude of  $\mathbf{F}(h, k, l)$  but not the relative phase shift between the diffracted waves.

After a crystal has been grown, the basic steps towards the desired molecular model are as follows:

1. Collection, processing and reduction of X-ray diffraction data

2. Phase determination
3. Interpretation of electron density maps (model building)
4. Refinement of the molecular model

### Data collection, processing and reduction

The source of X-rays is either an X-ray generator based on a rotating anode or an electron (or positron) storage ring that produces synchrotron radiation. The latter offers the advantage of higher beam intensity in a smaller beam cross section. The disadvantage that comes along with this regards the damage that X-rays cause in the crystal by means of ionisation processes. In the course of data collection, this can lead to both an overall deterioration of the diffraction quality and to specific chemical modifications depending on properties of the biomolecule under investigation. The diffraction (Fig. A.3) is governed by the *Bragg-equation*,

$$\lambda = 2 d_{hkl} \sin \theta_{hkl} \quad (\text{A.7})$$

where  $\lambda$  is the wavelength of the incident X-ray wave,  $\theta_{hkl}$  is the angle between the incident and diffracted beam and  $d_{hkl}$  is the distance between adjacent 'planes' of atoms in the crystal which are specified by the *Miller indices*  $h$ ,  $k$ ,  $l$  and from which the diffraction arises. The resolution to which data was collected is usually defined as the smallest plane spacing  $d_{min}$  in Bragg's law for which the corresponding diffraction spot (also called reflection) was observable. Overall diffraction quality is characterised by  $d_{min}$  and the imperfection in the regularity of the molecules' arrangement in the crystal ('*mosaicity*'). The latter is part of the so-called static (time-independent) disorder and can usually be removed only by improving the conditions from which the crystal was grown. The resolution is also determined by dynamic disorder (the fast vibrations of molecules about their mean position) and its gradual decrease during data collection can be diminished using cryogenic cooling of the crystal with a nitrogen vapour stream at 100 K (Garman & Schneider, 1997).

For the Fourier transform (A.6) to be performed with sufficient accuracy, a certain amount of data has to be collected. The total degree of crystal rotation that has to be covered depends on the *symmetry* present in the crystal lattice. The higher the symmetry, the more redundant is the data recorded per degree of rotation. The symmetry can be derived from the first image by assessing the fit of the observed diffraction pattern to each of the predicted patterns corresponding to a certain choice of the seven possible crystal systems. Once good agreement of observed and predicted pattern is achieved by choosing the correct symmetry, unit cell parameters

and mosaicity value, the spot intensities on each image are integrated, adjusted on a common scale and symmetry-equivalent reflections are merged according to the crystal symmetry. An indicator of data quality is the 'reliability factor' of merging  $i$  symmetry-equivalents which should in theory have identical intensities:

$$R_{\text{sym}} = \frac{\sum_{hkl} \sum_i |I_i(h, k, l) - \langle I(h, k, l) \rangle|}{\sum_{hkl} \sum_i |I_i(h, k, l)|} \quad (\text{A.8})$$

The final result is then a list of reflections  $(h, k, l)$  to which an intensity  $I(h, k, l)$  and its statistical error estimate  $\sigma_I(h, k, l)$  is assigned.

If the crystal lattice has more symmetry than just the translation of unit cells in three dimensions, then each molecular object will be repeated in the unit cell for a number of times as a result of this additional symmetry, the *space group* symmetry. It is then enough to find the electron density for one repeat within the unit cell which is called *asymmetric unit*. For example, NiSOD crystallized in space group  $P2_12_12_1$  that has four asymmetric units and relates an atom at position  $(x, y, z)$  to three other positions,  $(-x + \frac{1}{2}, -y, z + \frac{1}{2})$ ,  $(-x, y + \frac{1}{2}, -z + \frac{1}{2})$  and  $(x + \frac{1}{2}, -y + \frac{1}{2}, -z)$ . In each asymmetric unit, there may be more than one molecule which may again be related by some symmetry. This symmetry, termed 'non-crystallographic', is valid only locally (within the asymmetric unit) in contrast to 'crystallographic' symmetry which is used to build the whole crystal from the contents of the asymmetric unit.

Whereas the selection among the seven crystal systems was made at the data integration stage, the precise space group of the crystal can be determined only now based on merging statistics (low  $R_{\text{sym}}$ ) and the list of 'systematic absences' which arise from translational components in the space group symmetry operators. A  $2_1$  screw axis for example involves a  $180^\circ$  rotation and a translation by half a unit cell dimension that causes a characteristic set of extinctions of diffraction spots, see (Rossmann & Arnold, 2001). From the 230 existing space groups, only the 65 non-centrosymmetric space groups are possible choices for proteins because of the asymmetry of amino acids (only L-amino acids are present in proteins) thus limiting symmetry elements to rotations and screw axes.

Finally, the intensities  $I(h, k, l)$  need to be converted to structure factor amplitudes  $|\mathbf{F}|(h, k, l)$ . Only after the intensities have been put on 'absolute scale' (meaning that the corresponding  $|\mathbf{F}|$  is expressed in numbers of electrons), the amplitudes can be computed as square root of  $I$ . The scale factor is obtained from the *Wilson plot* (Wilson, 1942). Moreover, with the help of this plot an estimate of the 'temperature factor'  $B$  is obtained. Thermal vibration of each atom around its mean position  $(x, y, z)$  leads to an apparent smearing of the electron density in the final distribution

$\rho(x, y, z)$ . The  $B$ -factor is related to the root mean square displacement of the atom  $j$  and appears in an exponential factor that damps the scattering power (expressed as  $f_j$  in A.3) the more the higher the resolution of the reflection is:

$$f_{j,\text{effective}} = f_j \cdot \exp \left[ -B_j \left( \frac{\sin \theta}{\lambda} \right)^2 \right] \quad (\text{A.9})$$

This is why the earlier mentioned dynamic disorder results in weakened spot intensities at increasing resolution. In summary, there are four unknown parameters per atom, three coordinates ( $x, y, z$ ) and the isotropic  $B$ -factor, for which ideally a great excess of observations need to be available to solve a crystal structure. Although anisotropic thermal motion is a more realistic assumption, there are usually not enough data available to model these anisotropic  $B$ -factors ( $3 \times 3$  tensors).

### Phase determination and improvement

There are several methods to solve the phase problem, each of which is applicable if certain conditions are fulfilled:

1. *Molecular Replacement*. A structurally similar template molecule serves to derive initial phases. Suitable templates are searched based on high primary sequence identity with respect to the molecule of interest.
2. *Isomorphous Replacement*. Besides data from the 'native' (untreated) crystal, additional data are needed from a crystal in which a heavy atom is attached to each protein molecule ('heavy-atom derivative'). Small differences between intensities  $I_{\text{native}}(h, k, l)$  and  $I_{\text{derivative}}(h, k, l)$  are used to obtain initial phase information.
3. *Multiple-wavelength anomalous dispersion (MAD)*. The protein has to contain a sufficiently heavy atom of which the anomalous scattering property is exploited by tuning the X-ray wavelength to its absorption edge. The heavy atom is not introduced by soaking the crystal in a heavy atom solution (as in case of isomorphous replacement) but has to be present already in the native protein. Intensity differences between data at different X-ray wavelengths are used to solve the phase problem.
4. *Direct Methods*. These are routinely used in small molecule crystallography, but rarely in macromolecular crystallography due to the prerequisite of having a high ratio of observations to parameters. This is given only if a protein crystal diffracts to atomic resolution (about 1.2 Å or higher, depending on the size of the protein or, more precisely, on the number of atoms per asymmetric unit).

In the following, the discussion is limited to MAD since the NiSOD structure was solved with this method. The preparations for the application of MAD begin already before the first diffraction image is collected as the X-ray wavelength has to be tuned to special values. To understand which values to choose, one has to consider the effect of the incident X-rays with wavelength  $\lambda$  on the scattering behaviour of the heavy atom. This is characterized by the so-called anomaly in the scattering factor  $f$  if  $\lambda$  is close to an absorption edge value (Fig. A.4):

$$f_{\lambda} = f_0 + f'_{\lambda} + if''_{\lambda} \quad (\text{A.10})$$

where  $f_0$  is the scattering factor far away from any influence of the absorption edge

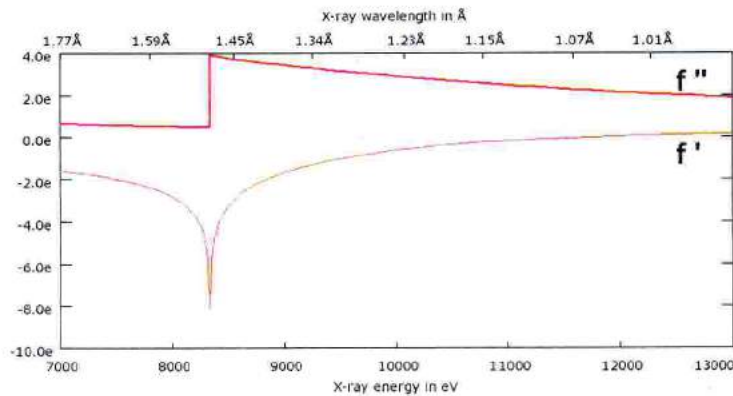


Figure A.4: Wavelength-dependence of the anomalous scattering factor for nickel at the K-edge derived using the theoretical approximation developed by Cromer and Liberman. This theory gives accurate values far from an absorption edge but does not account for the effects of neighbouring atoms in the particular protein of interest, which can be substantial near an absorption edge. Before starting the MAD data collection, a fluorescence scan close to the absorption edge is therefore carried out from which a protein specific  $f'$  and  $f''$  plot can be derived, cf. Fig. 6.1 and (Evans & Pettifer, 2001).

and  $f_{\lambda}$  is the now wavelength-dependent *anomalous scattering factor*. The immediate consequence of anomalous scattering is the break of *Friedel's law* which states that the reflections  $+(h, k, l)$  and  $-(h, k, l)$  have the same structure factor amplitude  $|\mathbf{F}|$  and opposite phase angles (Fig. A.5 A). Resulting 'anomalous differences'  $\Delta|\mathbf{F}|_{ano} = |\mathbf{F}(+)| - |\mathbf{F}(-)|$  are small but crucial to the MAD phasing method. They typically amount to only a few percent of  $|\mathbf{F}|$ . In addition, 'dispersive differences' are defined as  $\Delta|\mathbf{F}|_{disp} = |\langle \mathbf{F}(\lambda_1) \rangle| - |\langle \mathbf{F}(\lambda_2) \rangle|$ , i.e. over  $+$  and  $-(h, k, l)$  averaged differences between two datasets collected at distinct wavelengths. To maximize these useful differences, the choice of wavelengths is often made as follows:  $\lambda_{peak}$  is taken at the maximum of  $f''$  to optimize  $\Delta|\mathbf{F}|_{ano}$  whereas  $\lambda_{pi}$  and  $\lambda_{remote}$  are taken at the

minimum of  $f'$  (point of inflection in  $f''$ ) and far away from the absorption edge (where  $f'$  is close to zero), respectively, so that  $\Delta|\mathbf{F}|_{disp}$  is optimized. A smaller dispersive difference exists between  $\lambda_{peak}$  and  $\lambda_{pi}$  data.

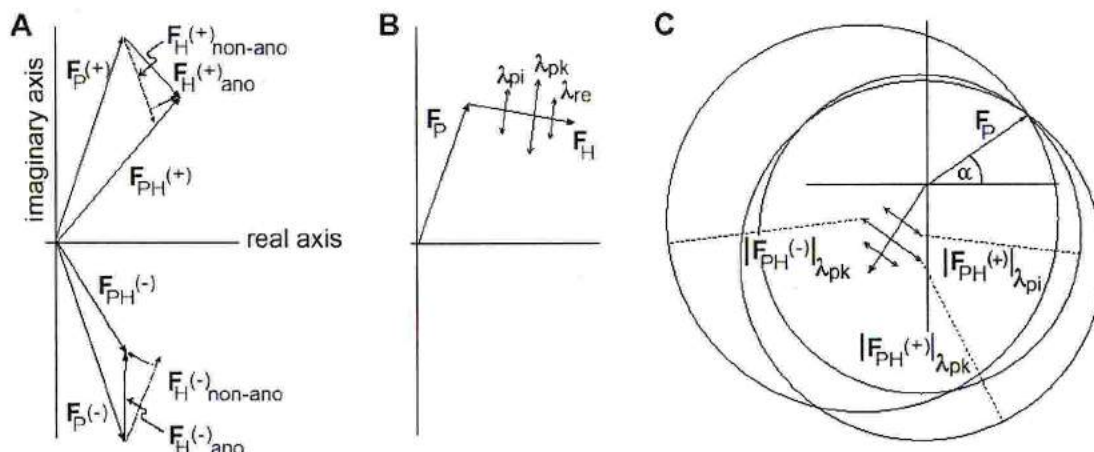


Figure A.5: (A) Break of Friedel's law illustrated in the complex plane (Argand diagram).  $\mathbf{F}_{PH}(+)$  and  $\mathbf{F}_{PH}(-)$ , the structure factors arising from both non-anomously scattering atoms (index P) and anomalous scatterers (index H), are no longer symmetric to the horizontal axis as are  $\mathbf{F}_P(+)/(-)$  and  $\mathbf{F}_H(+)/(-)_{non-ano}$  without anomalous scattering contribution. This is due to counterclockwise rotation of both  $\mathbf{F}_H(+)_ano$  and  $\mathbf{F}_H(-)_ano$  when anomalous scattering is present (see equation A.10 with  $i = \exp(i\pi/2)$ ). (B) For three wavelengths  $\lambda$  chosen as explained in the text, there are three vectors  $\mathbf{F}_H(+)$  and (here mirrored at the real axis) three vectors  $\mathbf{F}_H(-)$  whereas  $\mathbf{F}_P$  is wavelength-independent. (C) Harker diagram for the case of MAD with two wavelengths,  $\lambda_{peak}$  and  $\lambda_{pi}$ . To fulfill the relation  $\mathbf{F}_P = -\mathbf{F}_H + \mathbf{F}_{PH}$ , circles are drawn at the end of  $-\mathbf{F}_H$  with the corresponding measured magnitude of  $|\mathbf{F}_{PH}|$  as radius (dashed lines). The desired  $\mathbf{F}_P$  is then at the intersection of these circles.

Both anomalous and dispersive differences can be used to determine the positions of the anomalously scattering atoms in the unit cell. Textbooks show that, if a *Patterson map* with the general form

$$P(u, v, w) = \frac{1}{V} \sum_{hkl} |\mathbf{F}(h, k, l)|^2 \cos[2\pi(hu + kv + lw)] \quad (\text{A.11})$$

is calculated with coefficients  $(\Delta|\mathbf{F}|_{ano})^2$  or  $(\Delta|\mathbf{F}|_{disp})^2$  instead of  $|\mathbf{F}|^2$ , the set of anomalous scatterer positions can be derived from this map.  $(u, v, w)$  are coordinates in fractional units of the cell dimensions. Peaks in the Patterson map correspond to vectors between two atoms of the molecule and therefore do not give directly the anomalous scatterer positions. Assigning the highest peaks to vectors between either two anomalous scatterers and using the space group symmetry operators,

it is possible to derive their real positions. However, since the Patterson function is based on squared structure factor amplitudes  $|\mathbf{F}|^2$  and does not include phases, the Patterson map is symmetric with respect to its origin making it impossible to distinguish a set of atom positions from its enantiomorph.

For the determination of phase angles  $\alpha$  of non-anomalous scattering protein atoms, the structure factors of the anomalous scatterers  $\mathbf{F}_H$  are first calculated via equation A.4 from their coordinates. This is done for the initially obtained coordinate set and its enantiomorph, only one of which will finally lead to correct phases (see below). Having determined the vectors  $\mathbf{F}_H(+)$ ,  $\mathbf{F}_H(-)$  and together with the measured vector magnitudes  $|\mathbf{F}_{PH}(+)|$ ,  $|\mathbf{F}_{PH}(-)|$  it is then possible to derive the full vector  $\mathbf{F}_P$ , i.e. including the phases  $\alpha$ . Fig. A.5 B and C explain this graphically in the Harker diagram. Using the relation  $\mathbf{F}_{PH} = \mathbf{F}_P + \mathbf{F}_H$ , one finds the endpoint of vector  $\mathbf{F}_P$  by drawing circles at the endpoint of vectors  $-\mathbf{F}_H$  with radius  $|\mathbf{F}_{PH}|$ . For a sufficient number of circles each of which corresponds to a given Friedel member (+ or  $-(h, k, l)$ ) at a given wavelength  $\lambda$ , the correct vector  $\mathbf{F}_P$  will end at the intersection of all the circles. Fig. A.5 B shows that there are six vectors  $\mathbf{F}_H$  if data at three different wavelengths were collected as mentioned above, but only three of them were exploited in Fig. A.5 C to find  $\mathbf{F}_P$ :  $\mathbf{F}_H(+)$  and  $\mathbf{F}_H(-)$  at the  $f''$  peak wavelength and  $\mathbf{F}_H(+)$  at the point of  $f''$  inflection. This corresponds to the situation present in phase determination for NiSOD.

An inversion of real space positions at the origin translates to mirrored structure factors with respect to the horizontal axis in the Harker diagram. The correct set of anomalous scatterer coordinates is chosen on the basis of features in the electron density map of the protein: amino acids should show the L-configuration and  $\alpha$ -helices the right-handed configuration. The choice is easier the better the maps are, thus often it is postponed after the initial phases are improved by one or a combination of the following techniques.

*Solvent flipping.* The technique is based on the observation from well refined protein crystal structures that the electron density map between protein molecules appears flat due to the dynamic motion of solvent molecules. This feature is imposed on the still noisy map calculated with the phases from MAD by inversion (flipping) the sign of the solvent density (Abrahams, 1997). Subsequently, new structure factor amplitudes and phases are calculated from the modified map density via equation A.4. An improved map is then obtained by using observed amplitudes  $|\mathbf{F}|$  and phases from the solvent flipping (or a combination of these with original MAD phases).

*Non-crystallographic symmetry (NCS) averaging.* NCS operators that relate protein molecules in the asymmetric unit can be used in averaging the electron density within

the protein region. An envelope around the single molecule is needed which, contrary to solvent flipping, excludes the solvent region. Phases calculated from the averaged electron density map are combined with existing phase information to obtain a new map of better quality. Although the protein conformation in NCS related molecules is not necessarily identical the averaging process can improve the map substantially at this stage of structure determination by reducing the noise level by a factor of  $\sqrt{n}$ , where  $n$  is the number of NCS related molecules (Kleywegt & Read, 1997).

*Histogram Matching.* This technique does not act directly on the electron density map  $\rho(x, y, z)$  but on the frequency distribution of electron density values  $\rho$ . It was found that high quality structures of proteins have a protein-independent frequency distribution which is taken as a standard. The frequency distribution in the map to be improved is then scaled to the standard distribution. This technique is used in combination with solvent flipping (Cowtan, 1994).

*ARP/wARP.* The electron density map is searched for high density regions in which dummy oxygen atoms are placed, applying conditions on minimum and maximum distances between these atoms. This yields a dummy atom model from which structure factor amplitudes and phases are calculated. In a refinement procedure (see below), the atoms are moved in such a manner that the calculated structure factor amplitudes get closer to the observed ones. From the improved dummy model, better maps are derived from which in turn a better model is produced by adding or removing dummy atoms. This procedure is repeated for as many cycles as is needed for convergence (Perrakis *et al.*, 1997).

### Model building and refinement

The electron density map is interpreted with respect to chemical constituents, i.e. mainly the protein's amino acids but also ordered solvent molecules from the crystallization liquor or metal cofactors if present. The model is built into the density maps by visual inspection on a molecular graphics program (e.g. O (Jones *et al.*, 1991)) and may be performed, at least regarding the amino acids, by the automated ARP/wARP procedure just mentioned. In principle, model building and refinement represents the last step of phase improvement. Refinement consists of adjusting the model to satisfy as good as possible two conditions. Firstly, the structure factor amplitudes  $|\mathbf{F}_{calc}|$  calculated from the model via equation A.4 should agree as close as possible with the experimental (observed) structure factor amplitudes  $|\mathbf{F}_{obs}|$ . Secondly, the geometry of molecular constituents in the model, such as amino acids and solvent compounds as sulfate, should agree with already to high resolution known stereochemical data. The first condition is monitored by the reliability factor

$$R = \frac{\sum_{hkl} \left| |\mathbf{F}_{obs}| - k|\mathbf{F}_{calc}| \right|}{\sum_{hkl} |\mathbf{F}_{obs}|} \quad (\text{A.12})$$

where  $k$  is a scaling factor.  $R$  should lie below 30% for a final refined structure but is dependent on the resolution to which diffraction data is available. A more objective version of this factor,  $R_{\text{free}}$ , is obtained if the summation does not extend over all  $(h, k, l)$  but just over a set of 5-10% of them which was excluded from refinement (Brünger, 1992). The second condition is monitored by the root mean square (rms) deviations of the model geometry from known standard geometry values. The refinement procedure is performed by computer programs, e.g. CNS (Brünger *et al.*, 1998) or REFMAC (Murshudov *et al.*, 1997), and usually allows a certain degree of deviation from stereochemistry (restrained refinement in contrast to constrained refinement). It usually consists of minimizing a function by varying the parameters  $(x, y, z, B)$  of each atom (or a group of atoms) in the model, i.e. atomic positions and an isotropic temperature factor. This can be achieved the more precisely the higher the ratio of observations to parameters is. As observations do not only count measured reflections but also the information from stereochemical data.

After convergence in the computational update of atomic positions and B-factors is reached, maps are calculated with the observed structure factor amplitudes and phases derived from the model. Usually, the map coefficients used in the Fourier transform A.6 are not just  $|\mathbf{F}_{\text{obs}}|$  but  $2|\mathbf{F}_{\text{obs}}| - |\mathbf{F}_{\text{calc}}|$ . This is advantageous in finding deviations between the electron density as proposed by the X-ray data and the current model structure. Even more indicative of these deviations is the 'difference Fourier map' with coefficients  $|\mathbf{F}_{\text{obs}}| - |\mathbf{F}_{\text{calc}}|$  which can be contoured at a high positive or negative level of the standard deviation  $\sigma$  of electron density in the map. The maps are inspected visually on the graphics and corrections to the model can be done. These are usually necessary, especially at the beginning of refinement since computational refinement has a limited 'radius of convergence', i.e. cannot move atoms for distances exceeding a few Å.

Computational refinement and 'manual' refinement on the graphics are alternated until the R-factors  $R$  and  $R_{\text{free}}$  do not drop further and the rms deviations from 'ideal' stereochemical values reached an acceptable low level.

### A.3 Translational non-crystallographic symmetry

In this section, the purely translational non-crystallographic symmetry (NCS) that occurs exclusively in NiSOD crystals of the 'big cell' form I but not in the 'small cell' form III (see chapter 6) is analyzed in detail. NCS in general and purely translational NCS (also termed pseudo-translation) in particular are reviewed in (Kleywegt & Read, 1997).

The translation vector  $(0.05, 0.5, 0)$  or  $\frac{a}{20} + \frac{b}{2}$ , as concluded from Patterson maps (Fig. 6.2), is inserted into the structure factor defining equation (A.3) to derive both the effect of pseudo-translation on the structure factors  $\mathbf{F}(hkl)$  and the parity groups of reflections for which a certain modulation of  $\mathbf{F}(hkl)$  holds (Table A.1):

$$\begin{aligned}
\mathbf{F}_{hkl} &= \sum_{i=1}^{N/2} f_i \exp \{2\pi i(hx_i + ky_i + lz_i)\} + \\
&\quad + \sum_{j=1}^{N/2} f_j \exp \left\{ 2\pi i \left[ h \left( x_j + \frac{a}{20} \right) + k \left( y_j + \frac{b}{2} \right) + l(z_j + 0 \cdot c) \right] \right\} \\
&= \quad \text{“} \quad + \sum_{j=1}^{N/2} f_j \exp \left\{ 2\pi i [hx_j + ky_j + lz_j] + 2\pi i \left[ h \frac{a}{20} + k \frac{b}{2} \right] \right\} \\
&= \quad \text{“} \quad + \left( \sum_{j=1}^{N/2} f_j \exp \{2\pi i [hx_j + ky_j + lz_j]\} \right) \cdot \exp \left\{ 2\pi i \left[ h \frac{a}{20} + k \frac{b}{2} \right] \right\} \\
&= \left( \sum_{j=1}^{N/2} f_j \exp \{2\pi i [hx_j + ky_j + lz_j]\} \right) \cdot \left( 1 + \exp \left\{ 2\pi i \left[ h \frac{a}{20} + k \frac{b}{2} \right] \right\} \right)
\end{aligned}$$

Table A.1: Structure factor modulations due to translational NCS in crystal form I

Parity group <sup>a</sup>	$h = 20n$ $k = 2n$	$h = 20n$ $k = 2n + 1$	$h = 20n + m$ $k = 2n$	$h = 20n + m$ $k = 2n + 1$
Modulation factor <sup>b</sup>	1	0	$1 + \exp \left( 2\pi i \frac{m}{20} \right)$	$1 - \exp \left( 2\pi i \frac{m}{20} \right)$
Percentage of reflections	2.9	2.9	47.1	47.1
$\langle F_{norm}(hkl) \rangle / \langle F_{mod}(hkl) \rangle^c$ in resolution bins				
$\infty - 5.27$	1	1.9	1.96	0.86
5.27 - 3.74	1	1.57	1.37	1.01
3.74 - 3.06	1	1.31	1.28	1.15
3.06 - 2.65	1	1.13	1.19	1.02
2.65 - 2.37	1	1.03	1.08	0.94
2.37 - 2.17	1	1.02	1.00	1.04
2.17 - 2.0	1	1.11	1.06	1.07
2.0 - 1.88	1	1.02	1.03	1.02
1.88 - 1.77	1	1.00	1.04	1.06
1.77 - 1.68	1	1.00	1.06	1.00
1.68 - 1.6	1	0.97	1.05	1.10

<sup>a</sup> $n$  and  $m$  are integers, with  $m = 1, \dots, 19$ 
<sup>b</sup>The modulated structure factor  $\mathbf{F}_{mod}(hkl)$  is the normal structure factor  $\mathbf{F}_{norm}(hkl)$  multiplied by this factor.

<sup>c</sup>Values were calculated with  $m = 10$ . The number of reflections used in averaging range from 180 (lowest resolution bin) to 800 (highest resolution bin).

For the parity group ( $h = 20n$ ,  $k = 2n$ ), where  $n$  is an integer, no modulation of the structure factor exists, i.e. the observed  $F(hkl)$  equals the one in the case of absent pseudo-translation,  $F_{norm}(hkl)$ . In the 1.6 Å data set to which Table A.1 refers, only 2.9% of the 213373 measured unique reflections belong to this group. All other parity groups show modulation of the magnitude of  $F(hkl)$  and, where the integer  $m$  in  $h = 20n + m$  equals one of the values 1,...,9,11,...,19, also the phase of  $F(hkl)$  is affected. The pseudo-translation was characterized in a manner proposed by (Chook *et al.*, 1998). The ratio of the averaged structure factor in case of absent modulation,  $F_{norm}(hkl)$ , to the averaged structure factor for a given parity group showing modulation is used as quantitative indicator for the presence of pseudo-translation. Values of this ratio that deviate from 1 by more than 20% are taken as criterion of this kind of NCS. The averaged structure factors in resolution bins were calculated for the purpose of this analysis with TRUNCATE (CCP4, 1994) as square root of observed intensities, i.e. not following the French & Wilson scheme (French & Wilson, 1978) as generally applied since this scheme results in enhancing weak reflections and thus in partly disguising the effect to be analysed here. Ratios obtained for  $m = 10$  are compiled in Table A.1.

Both parity groups for which extinction of reflections is expected, ( $h = 20n$ ,  $k = 2n + 1$ ) and ( $h = 20n + 10$ ,  $k = 2n$ ), show ratios greater than 1.2 to approximately 3.0 Å resolution, with a maximum of almost 2 for the lowest resolution bin. The parity group ( $h = 20n + 10$ ,  $k = 2n + 1$ ) that is expected to have the double magnitude of the unmodulated structure factor shows a slightly lower ratio than 1 for the lowest resolution bin but does not reach the theoretical value of 0.5. This indicates that the modulation of structure factors is restricted to low resolution data and that translational NCS in this crystal form is not exactly realized as defined by the translation vector given above since the extinction of reflections in the first two parity groups occurs merely as systematic weakness and in the third group as slight increase of structure factor magnitude.

The molecular rearrangement that resulted in crystal form III has been the removal of purely translational NCS which relates two hexamers in crystal form I. The above characterization of this NCS by ratios of averaged structure factors for certain parity groups revealed that low resolution reflections are affected by modulations of the structure factor magnitude and, for many parity groups, of the phase angle as well. MAD phasing with this crystal form could not be performed successfully since no procedure for calculation of protein phase angles which could appropriately take into account the observed structure factor modulations was implemented in available macromolecular crystallography program packages. NCS averaging of the translationally related hexamers did not improve the quality of electron density maps. The explanation might be that there is only little additional information gained for phase

improvement by averaging two density regions in an asymmetric unit if the NCS almost equals a crystallographic symmetry that would force the two regions to be in separate unit cells. This crystallographic situation is realized in crystal form III where a hexamer-relating translation corresponding to the component of 0.05 of the pseudo-translation vector is not present. Thus a purely crystallographic translation along the axis corresponding to the b axis of form I is possible and leads to the observed splitting of the unit cell. It is therefore the small but important component of 0.05 which does not permit the solution of the pseudo-translation problem by the introduction of pseudo-origins. This could correct for the component of 0.5 along b if it was present as the only component of pseudo-translation (see e.g. (Morais *et al.*, 2000) for a successful treatment of this case of pseudo-translation vector).

# Appendix B

## Spectroscopic Methods

This appendix gives a short introduction to spectroscopic techniques that were used for investigating structural features of NiSOD. Their physical principles, the information they need as input and the questions they are able to answer will be outlined. For more detailed information, see e.g. (Que, 2000).

### B.1 Visible/UV Spectroscopy

Most proteins absorb light in the near-ultraviolet (UV) and in the visible region of the electromagnetic spectrum, i.e. in the wavelength ranges 150-400 nm and 400-800 nm, respectively. The associated energy of the light quanta is used to excite electrons from a lower to a higher energy state. The wavelength at which absorption features occur and the strength of these features depends on the chemical nature of the absorbing species and to some extent also on the molecular environment of this species ('chromophore'). The latter is the basis for applications of UV/visible spectroscopy to investigate conformational transitions in proteins, enzyme catalysis and ligand-binding reactions.

The most common application, however, is the determination of the concentration of proteins and nucleic acids in solution. The absorbance  $A$  of a molecule depends linearly on the molecule's concentration in a solution according to the *Lambert-Beer law*

$$A = \epsilon cl \quad \text{with} \quad (\text{B.1})$$

$$A = -\log_{10}(I/I_0) \quad (\text{B.2})$$

where  $I_0$  and  $I$  are light intensities before and after passage through the protein solution,  $\epsilon$  is the molar extinction coefficient,  $c$  the concentration and  $l$  the light-pathlength in the cuvette. In case of proteins, an absorption peak occurs

between 275 and 280 nm wavelength which is due to delocalised electrons in the aromatic side chains of tryptophans, tyrosines and, to a smaller extent, in disulfide bridges. The molar extinction coefficient can be estimated from the number of these chromophores in the protein. Nucleic acids instead show a strong peak at 260 nm wavelength.

The absorption spectra of aromatic amino acids are sensitive to structural changes in their close neighbourhood. This allows the study of protein unfolding processes as a function of temperature or denaturing agents such as urea or guanidinium chloride. Applications in enzyme kinetics are based on changes in the absorption spectrum at wavelengths specific to the substrate or the product molecule. The rate of the catalytic reaction ( $-\frac{d[S]}{dt}$  or  $\frac{d[P]}{dt}$ ) can be determined by measuring the decrease in the substrate concentration [S] or the increase in product concentration [P] as a function of reaction time  $t$ .

Regarding metallo-enzymes, this technique can be employed in studies of the type and oxidation state of the metal species as for instance in the case of NiSOD. (Bourgeois *et al.*, 2002) and (Sjögren *et al.*, 2002) discuss the usefulness of UV/visible absorption and fluorescence spectrophotometry for studies in the crystalline state, including the triggering, control and monitoring of enzyme reactions, the trapping of reaction intermediates for subsequent cryogenic X-ray data collection and the comparison of enzyme activity to the solution state.

The detection and monitoring of radiation damage by X-ray-induced photoelectrons in the course of diffraction data collection is a very interesting application with regard to the present study of NiSOD (see section 7.3.1). Reduction of a metal-centre and/or disulfide bonds will introduce considerable changes to the spectrum. Examples concerning iron-containing enzymes can be found in (Karlsson *et al.*, 2000) and (Berglund *et al.*, 2002).

## B.2 Electron Paramagnetic Resonance Spectroscopy

Electron Paramagnetic Resonance (EPR) or Electron Spin Resonance (ESR) spectroscopy is a technique to investigate properties of a paramagnetic centre, i.e. its identity and chemical environment. This centre may be any chemical species with at least one unpaired electron, such as radicals or compounds containing certain transition metal ions. The physical phenomenon utilized in this technique is the interaction of the unpaired electron with an applied magnetic field, the *Zeeman-interaction*.

The fundamental physical quantities needed are the following:

$$\vec{\mu} = -g\mu_o\vec{S} \quad (\text{B.3})$$

$$E = -\vec{\mu} \cdot \vec{B} \quad (\text{B.4})$$

$$E_\gamma = h\nu \quad (\text{B.5})$$

The spin  $\vec{S}$  of the unpaired electron is related to a magnetic moment  $\vec{\mu}$  by two factors; the Bohr magneton\* and the *Landé* value  $g$  (for a free electron,  $g \approx 2.0023$ ). In the second equation, the change in the electron's energy is given and is due to interaction of the magnetic moment with the externally applied magnetic field  $\vec{B}$ . Inserting the first into the second equation yields

$$E = g\mu_o\vec{S} \cdot \vec{B} = g\mu_o m_S B. \quad (\text{B.6})$$

$m_S$  is the projection of the spin vector along the direction of the magnetic field and can have one of the two values  $+\frac{1}{2}$  or  $-\frac{1}{2}$  since for an electron,  $S = \frac{1}{2}$ . These two situations, corresponding to a spin vector parallel (antiparallel) to the magnetic field, result in the increase (decrease) of the electron's energy by the amount  $\frac{1}{2}g\mu_o B$ . The energy difference between these two spin states is

$$\Delta E = E_{+\frac{1}{2}} - E_{-\frac{1}{2}} = g\mu_o B \quad (\text{B.7})$$

and can be supplied to the unpaired electron by absorption of a light quantum of appropriate energy  $h\nu$ , where  $\nu$  is the frequency. This will cause the spins of the energetically favoured orientation ( $m_S = -\frac{1}{2}$ ) to flip into the unfavoured orientation ( $m_S = +\frac{1}{2}$ ) under the so-called 'resonance condition'

$$h\nu = \Delta E = g\mu_o B_{res}. \quad (\text{B.8})$$

The EPR measurement thus consists of varying the field strength at a fixed frequency of the incident radiation until the above condition is fulfilled (Fig. B.1), although, but technically more difficult, the opposite experimental mode, i.e. frequency modulations at a constant field strength, would also be conceivable. Typically, in the so-called X-band, the frequency is held at about 9 to 10 GHz (3 to 30 cm wavelength). Spectra may also be taken at lower or at higher frequencies, e.g. 3 GHz or 35 GHz, because the resolution of certain spectral features can be enhanced.

At thermal equilibrium the ratio of the sample's electron populations in spin-parallel and spin-antiparallel orientation is given by the *Boltzmann* distribution. Using typical values for the magnetic field strength, 0.1-1 Tesla, and room temperature, 300 K, one obtains

$$\frac{N_+}{N_-} = \exp(-\Delta E/k_B T) \approx 0.999 \quad (\text{B.9})$$

---

\*defined as  $\mu_o = e\hbar/2m \approx 9.285 \cdot 10^{24} \text{C/T}$  with  $e$  and  $m$  as the elementary charge and electron mass.

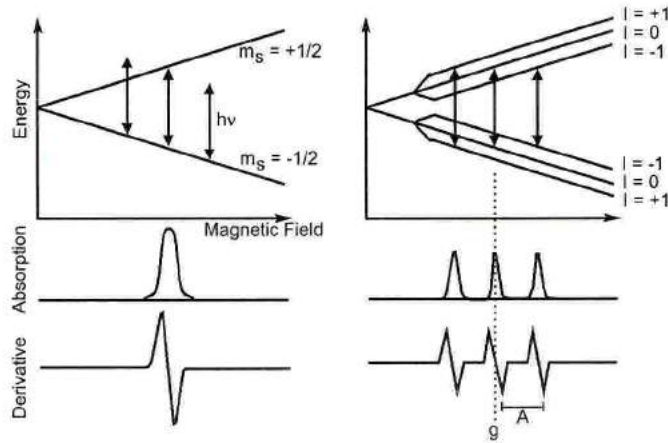


Figure B.1: Schematic representation of the generation of an EPR spectrum, taken from (Que, 2000). (*left*) When the energy condition B.7 is fulfilled, resonance absorption occurs. (*right*) In addition to *Zeeman*-interaction as in (A), hyperfine interaction with a nuclear spin  $I = 1$  is present. Here, the  $g$ -value defines the centre of the resonance being split in  $2I + 1$  lines by  $A$ , the hyperfine splitting constant (see text).

This means that there is only 0.1% net excess of spins in the  $m_S = -\frac{1}{2}$  state. As the net excess is needed for resonance absorption, it is usually increased using lower sample temperatures (between 4 and 100 K). Continuous EPR measurements necessitate that the net excess, i.e. the thermal equilibrium be restored after absorption of radiation. This is done on the time scale determined by the spin-lattice relaxation which underlies the removal of the absorbed energy. If the power of the incident radiation is too high (saturation) the population difference decreases and the measurement loses sensitivity by broadening the resonance lines.

Once the resonance absorption has been observed, it is possible to calculate the corresponding  $g$  value for the paramagnetic centre under investigation:

$$g = h\nu / \mu_o B_{res}. \quad (\text{B.10})$$

The usefulness of EPR spectroscopy lies in the fact that  $g$  is not simply a number as given above but that it is often anisotropic, i.e. dependent on the orientation of the paramagnetic centre's environment relative to the direction of the applied magnetic field. Generally, properties of the centre are deduced from the influence of various types of interactions, such as spin-orbit interaction and hyperfine interactions, on the EPR spectrum. In the following, this is briefly described separately for those interactions which are relevant to the study of transition metals.

(a) *Spin-Orbit Interaction*

If the unpaired electron exhibits an energetical coupling between its spin  $\vec{S}$  and

its orbital angular momentum  $\vec{L}$  then an additional term  $\lambda\vec{L} \cdot \vec{S}$ , where  $\lambda$  is the spin-orbit coupling constant, has to be considered in (B.6):

$$E = g\mu_o\vec{B} \cdot \vec{S} + \lambda\vec{L} \cdot \vec{S} \equiv \mu_o\vec{B} \cdot \mathbf{g} \cdot \vec{S}_f \quad (\text{B.11})$$

$\lambda\vec{L}$  may be considered as a local magnetic field which modulates the external field  $\vec{B}$  and which is generated, from the electron's view point, by the nucleus' motion around it. In the last part, a formulation has been used to show that with a 'fictitious spin'  $\vec{S}_f$ , an analogous expression as in (B.6) can be obtained for the energy if the  $g$  value is replaced by a  $3 \times 3$  tensor  $\mathbf{g}$ . This means that the paramagnetic centres of a sample in which they are statistically oriented with respect to the magnetic field may show more than one resonance line. Usually not all nine elements of the  $\mathbf{g}$ -tensor are needed; since the tensor is most often symmetric about the diagonal, the three principle values  $g_x$ ,  $g_y$  and  $g_z$  or, in axially symmetric molecular centres, two values  $g_{\parallel}$  and  $g_{\perp}$  are sufficient (Fig. B.2).

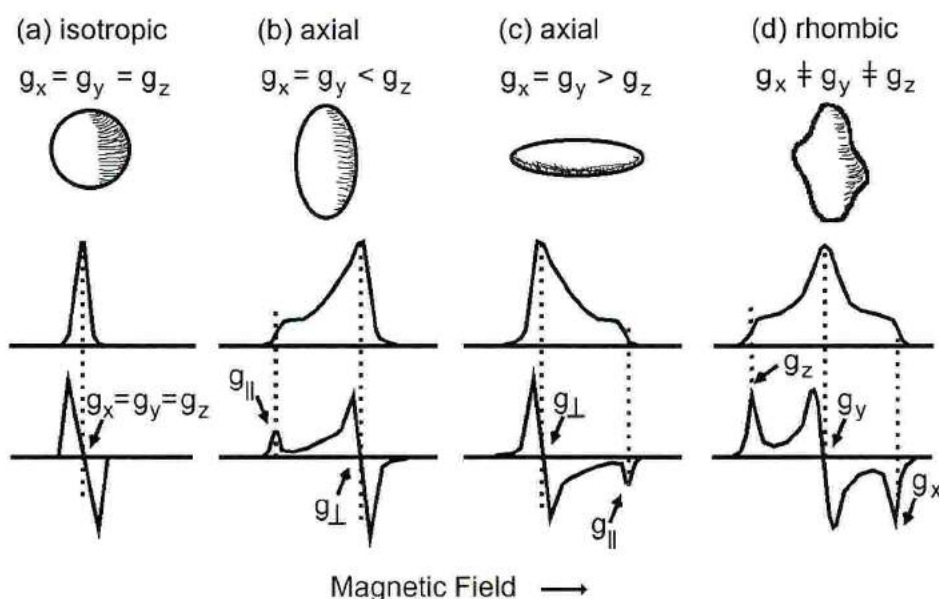


Figure B.2: Basic spectra for a spin =  $\frac{1}{2}$  paramagnet, taken from (Que, 2000). The anisotropy of  $\mathbf{g}$  is presented both numerically and graphically as solid bodies.

The spin-pairing of electrons in the  $3d$  orbital of a transition metal ion should be according to *Hund's rule*, i.e. giving preference to parallel spins while successively occupying the first five possible configurations and then filling up the remaining configurations with electrons of opposite spin. In a metal ion of a specific coordination environment, however, this scheme may be modified due to energetical reasons: the ionic (electrostatic) and/or covalent bonds of the ligands to the ion cause characteristic splittings between the energy levels of the  $3d$  orbitals (as shown in

crystal field and ligand field theory). Depending on the geometry and strength of the ligands, a specific distribution of the electrons in the  $3d$  orbitals may be energetically favourable. This causes the distinction between low-spin and high-spin complexes; if the crystal field is so strong that the above rule is not obeyed any more, the number of unpaired electrons and therefore the total spin of all  $3d$  electrons will be smaller than in the case of weak or absent crystal field. Thus, via the number of the unpaired electron's and the orientation of their  $3d$  orbitals in the external magnetic field, the observed resonance spectrum will reflect the influence of the ligand environment.

(b) *Hyperfine- & Superhyperfine Interaction*

The overall shape of the spectrum is determined by the anisotropy of the  $g$  values and hence by the spin-orbit interaction. If now the unpaired electron is under the influence of a nuclear spin  $I$  of either its associate nucleus ("hyperfine interaction") or a nucleus of a ligand ("superhyperfine interaction") then additional features are visible in the EPR spectrum (Fig. B.1, *right*). In case of isotropic superhyperfine interaction, these features, however, may be located at only one of the three  $g$  features in the spectrum due to the directionality of the involved  $I > 0$  ligand and  $3d$  orbitals.

The magnetic moment  $\mu_n = g_n \mu_{0,n} I$  of the nucleus ( $g_n$  and  $\mu_{0,n}$  are the nuclear  $g$ -value and magneton, respectively) is the source of a magnetic field, the nuclear hyperfine field  $B_{HF}$  which combines with the laboratory field to an overall field required to satisfy the resonance condition (B.8):

$$B_{res} = B_{Lab} + B_{HF} \quad (\text{B.12})$$

$I$  can adopt  $2I + 1$  orientations in the applied field  $B_{Lab}$ , thus giving rise to an equal number of hyperfine lines in the spectrum. The lines are separated by the hyperfine splitting constant  $A$  measured in mT (or Gauss).

In summary, information extracted from the interpretation of an EPR spectrum on a transition metal ion may contain the

1. metal type and its oxidation state,
2. type of the  $d$ -orbital of the unpaired electron,
3. covalent contribution to the bond between the metal ion and a ligand,
4. identity of a ligand and its position in the coordination environment (e.g. equatorial, axial).

## B.3 X-ray Absorption Spectroscopy

X-ray Absorption Spectroscopy (XAS) can yield structural information about a local region also from non-crystalline samples and is therefore usually considered complementary to X-ray crystallography which is able to provide the whole structure of a sample molecule as soon as it can be prepared in crystalline form. The following introduction to XAS is taken from R.A. Scott in (Que, 2000).

The X-ray absorption spectrum is a measurement of the energy-dependent absorption coefficient of a particular element present in the sample. On the synchrotron beamline it is possible to sweep the X-ray energy across the range in which the sharp rise in the absorption coefficient due to electron dissociation from a core level of the absorbing atom occurs. The 'absorption edge' of NiSOD due to the K-edge of nickel is shown in Fig. 4.6 and may serve as example. Traditionally, the spectral features of the immediate edge region (X-ray Absorption Near Edge Structure, XANES) are analysed separately from the almost periodic features above the edge (Extended X-ray Absorption Fine Structure, EXAFS). This is because the underlying phenomena and the obtainable information from these features are different. The EXAFS technique yields *radial* structural information within a radius of 4-5 Å around the absorbing atom. It answers the question *how many atoms of which atom type are at what distance* from the absorbing atom. If the environment of this atom is not homogeneous in the sample, an average is obtained which is in general less informative with respect to each single environment. XANES instead can yield *geometrical* structural information from spectral features in the edge region, i.e. it can distinguish between different coordination geometries, like tetrahedral from octahedral coordination for example.

### XANES

Since absorption edge energies are a monotonically increasing function of the element's atomic number and the X-ray energies accessible at synchrotrons lie between 2-30 keV, the K-edge can be used for the elements from P to Sn only. For heavier elements one can exploit the L-edges. The edge region of a spectrum can exhibit features as for example the shoulder in the NiSOD spectrum, Fig. 4.6. These peaks just before the absolute maximum of absorption arise from electronic transitions from the core level 1s to valence levels, e.g. 4p<sub>z</sub>, and can reveal information about the symmetry of the absorbing atom's site. In addition, the precise energy of the absorption edge depends on the charge density at the absorbing atom (i.e. its valence or oxidation state) which in turn is influenced by its chemical environment. The higher the oxidation state, the more will the absorption edge be shifted to a higher energy value.

## EXAFS

The information derived from EXAFS arises from the interaction of the X-ray dissociated core electron (the so-called photoelectron) with electron density surrounding the absorbing atom. The periodic modulations just above the absorption maximum in the spectrum stem from scattering of the photoelectron on electrons of neighbouring atoms. They encode therefore the structural information about the absorbing atom's neighbourhood. The origin of these modulations can be explained using the wave picture of electrons. The photoelectron just about to propagate away from the absorbing atom has to be superimposed with waves of previously generated photoelectrons which were back-scattered from neighbouring atoms. The modulations are thus an interference effect of electron waves at the site of the central atom. The interference can enhance or decrease the electron density at this site depending on the wavelength of the electron waves which is determined by the difference between the incoming photon's energy  $E$  and the edge energy (ionisation energy)  $E_0$ . This energy difference  $E - E_0$  represents the kinetic energy of the photoelectron and is scanned throughout the EXAFS region. An increase of electron density, i.e. increased amplitude of the back-scattered wave at the absorbing atom leads to a maximum in the EXAFS region and a decrease results in a minimum.

Each scattering atom around the absorbing atom contributes to the overall EXAFS spectrum with a sine wave. Each of these sine waves is described by three measurable quantities, the amplitude, the frequency and the phase. The frequency of a component sine wave is a measure of the distance from the absorbing to the scattering atom. The amplitude can be related to the number of atoms at that distance and also to the type of atom because the heavier an atom is the better it scatters, yielding an EXAFS component with a larger amplitude. If more than one atom of this type is located at a given distance from the absorbing atom their sine waves add up to a resulting wave of twice the amplitude but can otherwise not be distinguished since EXAFS exhibits only radial but not angular sensitivity. This purely radial dependence gives rise to the concept of 'shells' of atoms. Finally, the phase of the sine wave can reveal the identity of the scattering atom. This phase is determined by the phase shift in the photoelectron's wave introduced in the back-scattering process and is dependent on the electron density at the scattering atom. Thus different atom types result in different phase shifts, thereby modulating the overall EXAFS spectrum.

The quantitative analysis of EXAFS data in terms of absorber-scatterer distance, scatterer number and types is based on an expression for the quasi-periodic modulations of the absorption coefficient  $\mu$  at energy  $E$  in the EXAFS region with respect

to  $\mu_0$  at the edge energy  $E_0$ :

$$\chi \stackrel{def}{=} \frac{\mu - \mu_0}{\mu_0} \quad (\text{B.13})$$

$\chi$  is a function of the photoelectron's wavenumber  $k = \frac{2\pi}{\lambda}$  and consists of a summation over shells of scatterers. Each term of this sum shows three factors; an amplitude, a Debye-Waller factor describing the damping of the sinusoidal modulations due to static and dynamic variations in absorber-scatterer distances  $r_{as}$ , and a sine function  $\sin(2r_{as}k + \alpha_{as}(k))$  where  $\alpha_{as}$  is the phase shift. Usually, one plots the quantity  $k^3\chi(k)$  instead of  $\chi(k)$  alone to compensate for the damping factor and the  $k^{-1}$ -dependence of the amplitude factor. A Fourier Transform (FT) of this expression yields the distribution of absorber-scatterer distances  $r_{as}$  (after correction for the phase shift) in which each peak represents a particular shell of atoms. Interpretation of EXAFS data in terms of structural information uses simulations of the EXAFS spectrum assuming various hypothetical arrangements of atoms around the absorbing atom, i.e. various radial distributions of scattering atoms,  $r_{as}(\text{\AA})$ , and analyses which assumption results in the closest fit to the observed data.

There are two alternative experimental set-ups for collection of XAS data. The transmission technique uses two ionisation chambers as detectors, one before the sample to record the incident X-ray intensity  $I_0$  and another behind the sample to measure the intensity  $I$  after the absorption events. This gives a direct measure of the absorption coefficient. For dilute samples of absorbers, such as metalloenzymes in solution, the fluorescence excitation technique is in general employed. Here, the  $K_\alpha$  fluorescence emission is monitored while the incident X-ray photon energy is scanned through the K-edge and the EXAFS region. This provides a mimic of the absorption spectrum since the number of emitted  $K_\alpha$  photons is directly proportional to the number of photons absorbed. XAS on NiSOD was performed using the fluorescence excitation technique. Its advantage over the transmission technique is a higher sensitivity due to better signal-to-noise ratio. The reason is that a transmission spectrum of a dilute sample shows background absorption by all other atoms in the sample, whereas fluorescence excitation spectrum displays only the absorption by the atom of interest.

# Appendix C

## Kinetic Studies on Superoxide Dismutases

### C.1 General aspects of Kinetics

In the following, a short overview of steady state enzyme kinetics will be given which was adapted from textbooks like (Fersht, 1999) and (Jencks, 1969).

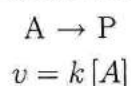
'*Steady state kinetics*' makes the assumption that the concentration of enzyme-substrate intermediates [ES] formed during the conversion of substrate to product does not change with time. As a consequence, the rate of catalysis  $v$  changes only slowly with time if the substrate S is present in large excess relative to the enzyme E (or shorter, if  $[S] \gg [E]$ ). This is fulfilled, for instance, in studies of cellular metabolism. The short initial period in which the steady state value of [ES] builds up is the subject of '*pre-steady state kinetics*'. It is especially insightful for the investigation of chemical mechanisms of enzyme catalysis and requires either measurements in very short time ranges ( $1 - 10^{-7}$  s) or other special techniques. In this short text, only kinetics applying to steady state conditions is considered.

The rate of reaction is given by

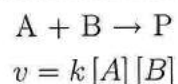
$$v = \frac{d[P]}{dt} = -\frac{d[S]}{dt} \quad (\text{C.1})$$

where [P] is the product concentration and  $t$  is the time. The order of a reaction is defined as the number of molecule concentrations to which  $v$  is proportional, e.g.:

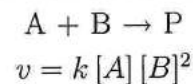
first-order reaction



second-order reaction



third-order reaction



$k$  is the proportionality constant between  $v$  and the concentrations of involved reactants. It is known as *catalytic rate constant* and is characteristic of a given enzyme. Its unit is  $\text{s}^{-1}$  in case of a first-order rate constant and  $\text{M}^{-1}\text{s}^{-1}$  for second-order rate constants.

For many enzymes, the *Michaelis-Menten equation* provides the general shape of expressions for the catalytic rate:

$$v = \frac{k_{cat} [E]_0 [S]}{K_M + [S]} \quad \text{where} \quad (\text{C.2})$$

$$k_{cat} [E]_0 = V_{max} \quad ([E]_0 = \text{total enzyme concentration}) \quad (\text{C.3})$$

$$K_M = [S]_{v=V_{max}/2} \quad (\text{Michaelis constant}) \quad (\text{C.4})$$

A plot of  $v$  versus  $[S]$  shows that for high  $[S]$ , the rate becomes saturated, i.e. essentially independent of  $[S]$ , with an asymptotic value of  $V_{max}$ . However, if  $[S] \ll K_M$ , the rate is linearly proportional to  $[S]$ :  $v = [S] \frac{V_{max}}{K_M}$ . The explicit expression for  $k_{cat}$  and  $K_M$ , and hence for  $v$ , depends on assumptions regarding how fast certain steps in the reaction scheme proceed and how many intermediates are formed during the conversion of  $[S]$  to  $[P]$ . Three cases are shortly discussed in the following.

### Michaelis-Menten kinetics.

The reaction scheme is assumed to be



An enzyme-substrate complex ES is formed non-covalently and reversibly. Its rate of formation or dissociation is

$$K_S = \frac{[E][S]}{[ES]} \quad (\text{C.6})$$

$[E]$  refers to the concentration of free enzyme, i.e.  $[E] = [E]_0 - [ES]$ . The catalysis takes place in the second step with the first-order rate constant

$$k_{cat} = \frac{v}{[ES]} \quad (\text{C.7})$$

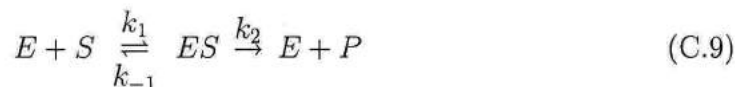
from which the expression for the rate

$$v = \frac{k_{cat}[E]_0[S]}{K_S + [S]} \quad (\text{C.8})$$

is derived. It should be noted that the following assumptions were made:

1. Low  $[P]$ : the reverse reaction  $E + P \rightarrow ES$  is ignored.
2. The complex EP is ignored due to its fast dissociation.
3. Thermodynamic equilibrium between  $E + S$  and ES.

The last assumption is given if in the reformulation of the above scheme



holds that  $k_2 \ll k_{-1}$ , with  $k_1$  and  $k_{-1}$  as second-order rate constants of substrate association and dissociation, respectively. These assumptions lead to a rate law which is equal to the Michaelis-Menten equation if  $K_M$  is replaced by  $K_S$ . Thus, for Michaelis-Menten kinetics,  $K_M = K_S$ .

### Briggs-Haldane kinetics.

The above assumption of thermodynamic equilibrium between  $E + S$  and  $ES$  is now omitted and  $k_2$  may be similar to  $k_{-1}$  as is true for fast enzymes such as SOD. The catalytic rate for the assumed reaction scheme (C.9) is

$$v = \frac{k_2[E]_0[S]}{(k_2 + k_{-1})/k_1 + [S]} \quad (\text{C.10})$$

By comparison with the Michaelis-Menten equation, one obtains the following expression for the Michaelis constant, using  $K_S = \frac{k_{-1}}{k_1}$ ,

$$K_M = (k_2 + k_{-1})/k_1 = K_S + \frac{k_2}{k_1} \quad (\text{C.11})$$

In Briggs-Haldane kinetics therefore,  $K_M$  is greater than  $K_S$ . The first-order catalytic rate constant  $k_{cat}$  corresponds as before to  $k_2$ .

### Kinetics with intermediates after ES.

If there is one or more additional intermediate state after the  $ES$  complex, the reaction scheme can be written as



In this case, the rate is given by the Michaelis-Menten equation where the following substitutions have to be made:

$$K_M = \frac{K_S}{1 + K' + K'K''}, \quad \text{i.e. } K_M < K_S \quad (\text{C.13})$$

and

$$k_{cat} = \frac{k_4 K' K''}{1 + K' + K'K''}. \quad (\text{C.14})$$

Experimental information for rate constants  $K'$ ,  $K''$  etc. can in general be obtained only from pre-steady state kinetic measurements.

In conclusion,  $k_{cat}$  can either be a simple first-order rate constant for the conversion of ES to EP or a complex function of all first-order rate constants involved in the several intermediate states. A property of  $k_{cat}$  is that it cannot be greater than any of these intermediate first-order rate constants in the forward reaction pathway and thus represents a lower limit on the chemical rate constants. In other words,  $k_{cat}$  is the maximum number of substrate molecules converted to products per active site and unit time, and therefore is often called '*turnover number*'. The Michaelis constant either equals in the simplest case the dissociation constant,  $K_M = K_S$ , or corresponds to an apparent or overall dissociation constant in case of more complex reaction schemes.

The ratio  $\frac{k_{cat}}{K_M}$ , which is an apparent second-order catalytic rate constant for the reaction of *free* enzyme with *free* substrate, has interesting properties. It determines the specificity for competing substrates if an enzyme has more than one possible substrate. Secondly, it can be used as criterion how close the overall catalytic rate approaches the '*diffusion limit*' of random enzyme-substrate encounters in solution. If  $[S] \ll K_M$ , the rate is  $v = \frac{k_{cat}}{K_M}[E]_0[S]$ , i.e.  $\frac{k_{cat}}{K_M}$  corresponds to a second-order rate constant. Applying Briggs-Haldane kinetics for fast enzymes, it follows that

$$\frac{k_{cat}}{K_M} = \frac{k_{cat} k_1}{k_{cat} + k_{-1}} < k_1 \quad \text{since } k_{-1} > 0. \quad (\text{C.15})$$

The more  $\frac{k_{cat}}{K_M}$  approaches  $k_1$ , the closer the enzymes works at diffusion limited rate since  $k_1$  is determined by the rate of collisions of enzyme and substrate and thus represents the absolute limit on the catalytic power of an enzyme.

The Michaelis-Menten parameters  $k_{cat}$  and  $K_M$  can be used to distinguish different types of inhibition modes. If  $K_M$  is apparently increased to  $K_{M,app}$  upon the enzyme's reaction with an inhibitor while  $k_{cat}$  (or  $V_{max}$ ) remains unchanged, then the inhibitor competes with the substrate for the active site ('*competitive inhibition*'). Parameters used to express the inhibition efficiency are the inhibitor concentration  $[I]$  that leads to the loss of 50 % enzyme activity ( $IC_{50}$ ) and the association constant of inhibitor binding to the enzyme that can be obtained as

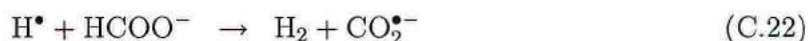
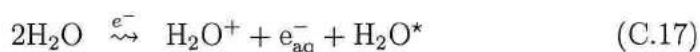
$$K = \frac{[E][I]}{[EI]} \quad \text{or} \quad K = \frac{[I]}{\frac{K_{M,app}}{K_M} - 1} \quad \text{or} \quad K = \frac{IC_{50}}{1 + \frac{[S]}{K_M}} \quad (\text{C.16})$$

Non-competitive inhibition is present when  $K_M$  is unaffected and  $k_{cat}$  lowered. Also a mixed inhibition mode exists in which both  $K_M$  and  $k_{cat}$  are changed with respect to kinetic behaviour in the absence of inhibitor. Both competitive and non-competitive inhibitors bind reversibly in contrast to inactivators.

## C.2 Superoxide Dismutase Activity Assays and Kinetics

A variety of methods exists to assess the activity of a given sample of SOD. These methods can be divided in direct and indirect assays (Halliwell & Gutteridge, 1999).

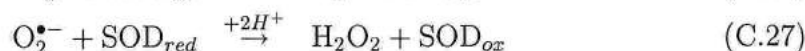
The *direct method* uses pulse radiolysis to generate superoxide anions and monitors the rate of the disappearance of the superoxide electronic absorbance at 245-260 nm due to active SOD. A source of high energy (2 MeV) electrons is used to ionize and excite water in the dilute aqueous solution of SOD. The solution may be saturated with O<sub>2</sub> and contain sodium formate (HCOONa) to facilitate the production of O<sub>2</sub><sup>•-</sup> according to the following reactions, see (Klug *et al.*, 1972), (Choudhury *et al.*, 1999) and (Halliwell & Gutteridge, 1999):



The observed decrease in the O<sub>2</sub><sup>•-</sup> absorbance  $A(t)$  as a function of time  $t$  after the O<sub>2</sub><sup>•-</sup>-producing pulse is a direct measure for SOD activity and can be used to obtain the catalytic rate constant of the dismutation reaction. From the Lambert-Beer law (B.1),

$$A = \varepsilon l [\text{O}_2^{\bullet-}] \quad (\text{C.25})$$

with  $\varepsilon$  as extinction coefficient of O<sub>2</sub><sup>•-</sup> (e.g.  $\varepsilon_{250\text{nm}} = 2000 \text{ M}^{-1}\text{cm}^{-1}$ ), the superoxide concentration is determined. Based on the two-step formulation of the dismutation reaction (Klug *et al.*, 1972),



the rate constants can be determined as follows:

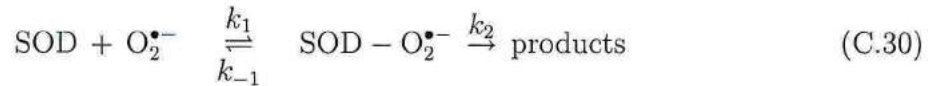
$$-\frac{d[\text{O}_2^{\bullet-}]}{dt} = k_{\text{ox}} [\text{SOD}_{\text{ox}}] [\text{O}_2^{\bullet-}] + k_{\text{red}} [\text{SOD}_{\text{red}}] [\text{O}_2^{\bullet-}] \quad (\text{C.28})$$

Assuming that  $k_{ox} = k_{red} = k$  and using  $[\text{SOD}_{ox}] + [\text{SOD}_{red}] = [\text{SOD}]_0$ , one obtains

$$-\frac{d[\text{O}_2^{\bullet-}]}{dt} = k [\text{SOD}]_0 [\text{O}_2^{\bullet-}] \Rightarrow [\text{O}_2^{\bullet-}] = e^{-k[\text{SOD}]_0 t}. \quad (\text{C.29})$$

Under the condition  $[\text{O}_2^{\bullet-}] \gg [\text{SOD}]_0$ , a plot of  $\ln[\text{O}_2^{\bullet-}]$  versus time  $\Delta t$  yields a straight line having a slope  $k [\text{SOD}]_0$ , the observed first-order rate with respect to  $\text{O}_2^{\bullet-}$ . Division by the known enzyme concentration  $[\text{SOD}]_0$  results in the second-order rate constant  $k$ .

Both reaction steps (C.26) and (C.27) follow Briggs-Haldane kinetics (C.10), see (Fee & Bull, 1986) and (Falconi *et al.*, 2002):



$$\frac{k_{cat}}{K_M} = \frac{k_1 k_2}{k_2 + k_{-1}} \approx k_1 \quad \text{since } k_2 \gg k_{-1}. \quad (\text{C.31})$$

*Indirect assays* use biochemical ways to generate superoxide radicals *in vivo* (Halliwell & Gutteridge, 1999).  $\text{O}_2^{\bullet-}$  is allowed to react with a detector molecule and SOD inhibits the reaction with the detector molecule by removing  $\text{O}_2^{\bullet-}$  from the sample solution. McCord and Fridovich (1969) utilized a mixture of the enzyme xanthine oxidase and its substrate xanthine for  $\text{O}_2^{\bullet-}$ -production and the detection system consisted of the haem protein cytochrome c. The change in cytochrome c absorbance at 550 nm is monitored during cytochrome c reduction by  $\text{O}_2^{\bullet-}$ . SOD inhibits the absorbance change upon removal of  $\text{O}_2^{\bullet-}$ . One unit of SOD activity is defined as the amount of enzyme that inhibits the reduction of cytochrome c by 50% under specified assay conditions. A general problem concerning this assay is the possibility that the absorbance change is not only due to SOD activity but also due to diminished production of  $\text{O}_2^{\bullet-}$ , e.g. when the xanthine oxidase is inhibited by unknown agents\*. The activity of the xanthine oxidase needs therefore to be monitored during the measurement. In addition, care must be taken that after  $\text{O}_2^{\bullet-}$  dependent reduction, cytochrome c is not reoxidised by the enzyme cytochrome oxidase which exists in many tissue extracts.

Besides the cytochrome c system which has been used for NiSOD as well (Youn *et al.*, 1996a + b, Kim *et al.*, 1996), other detector substances are in use, e.g. nitroblue tetrazolium (NBT). The molecule changes its colour to deep blue upon reduction by superoxide. This can be used in another assay method that is based on negative staining of SOD activity in non-denaturing polyacrylamide gels (Beauchamp & Fridovich, 1971). In principle, the gel is soaked in a solution containing NBT

\*This problem arises for example when SOD inhibition by  $\text{CN}^-$  or  $\text{N}_3^-$  is studied since these anions are also xanthine oxidase inhibitors.

and then exposed to fluorescence light for photochemical production of  $O_2^{\bullet-}$ . The reduction of NBT by  $O_2^{\bullet-}$  is inhibited where active SOD is present, thereby leaving a clear band in the blue background of the gel (see (Lee *et al.*, 2002) for application to NiSOD).

## ACKNOWLEDGEMENTS

I would like to thank

Kristina Djinovic Carugo for supervising and for the opportunity to work on the very interesting NiSOD project.

Sa-Ouk Kang and Jin-Won Lee for providing the protein and for fruitful collaboration in all stages of the NiSOD project.

Janos Hajdu for accepting the task of the external examiner.

Maurizio Polentarutti for help with the preparation of Xe-derivatized NiSOD crystals.

All members of the Lab for interesting scientific and non-scientific discussions and good company in the last four years.

The crystallography beamline staff of the ELETTRA synchrotron, Trieste, the European Synchrotron Radiation Facility, Grenoble, (in particular Gordon Leonard, Ed Mitchell and Andy Thompson), the Hamburg outstation of the European Molecular Biology Laboratory (in particular Paul Tucker).

Paul Adams, Gérard Bricogne, Eleanor Dodson, Randy Read, George Sheldrick and Clemens Vornrhein for helpful discussion about phasing NiSOD.

# Bibliography

- Abrahams, J.P. (1997). Bias Reduction in Phase Refinement by Modified Interference Functions: Introducing the  $\gamma$  Correction. *Acta Crystallogr. D* **53**, 371-376.
- Abreu, I.A., Xavier, A.V., LeGall, J., Cabelli, D.E. & Teixeira, M. (2002). Superoxide Scavenging by neelaredoxin: dismutation and reduction activities in anaerobes. *J. Biol. Inorg. Chem.* **7**, 668-674.
- Adams, M.W.W., Francis, E.J., Clay, M.D. & Johnson, M.K. (2002). Superoxide reductase: fact or fiction? *J. Biol. Inorg. Chem.* **7**, 647-652.
- Altschul, S.F., Gish, W., Miller, W., Myers, E.W. & Lipman, D.J. (1990). Basic local alignment search tool. *J. Mol. Biol.* **215**, 403-410.
- Auchère, F. & Rusnak, F. (2002). What is the ultimate fate of superoxide anion in vivo? *J. Biol. Inorg. Chem.* **7**, 664-667.
- Barton, G.J. (1993). Alscript: A tool to format multiple sequence alignments. *Protein Eng.* **6**, 37-40.
- Beauchamp, C. & Fridovich, I. (1971). Superoxide dismutase. Improved assays and an assay applicable to acrylamide gels. *Anal. Biochem.* **44**, 276-287.
- Benini, S., Rypniewski, W.R., Wilson, K.S., Miletto, S., Ciurli, S. & Mangani, S. (2000). The complex of *Bacillus pasteurii* urease with acetohydroxamate anion from X-ray data at 1.55 Å resolution. *J. Biol. Inorg. Chem.* **5**, 110-118.
- Berglund, G.I., Carlsson, G.H., Smith, A.T., Szöke, H., Henriksen, A. & Hajdu, J. (2002). The catalytic pathway of horseradish peroxidase at high resolution. *Nature* **417**, 463-468.
- Berisio, R., Lamzin, V.S., Sica, F., Wilson, K.S., Zagari, A. & Mazzarella, L. (1999). Protein Titration in the Crystal State. *J. Mol. Biol.* **292**, 845-854.
- Boggon, T.J. & Shapiro, L. (2000). Screening for phasing atoms in protein crystallography. *Structure* **8**, 143-149.

- Bordo, D., Pesce, A., Bolognesi, M., Stroppolo, M.E., Falconi, M. & Desideri, A. (2001). Copper-zinc superoxide dismutase in prokaryotes and eukaryotes. In: Handbook of Metalloproteins, Ed. by A. Messerschmidt, R. Huber, T. Poulos, K. Wieghardt. Wiley & Son, Chichester, UK, Vol. 2, 1284-1300.
- Bourgeois, D., Vernede, X., Adam, V., Fioravanti, E. & Ursby, T. (2002). A microspectrophotometer for UV-visible absorption and fluorescence studies of protein crystals. *J. Appl. Crystallogr.* **35**, 319-326.
- Brünger, A.T. (1992). Free R-value - a novel statistical quantity for assessing the accuracy of crystal structures. *Nature* **355**, 472-475.
- Brünger, A.T., Adams, P.D., Clore, D.M., DeLano, W.L., Gros, P., Grosse-Kunstleve, R.W., Jiang, J.-S., Kuszewski, J., Nilges, M., Pannu, N.S., Read, R.J., Rice, L.M., Simonson, T. & Warren, G.L. (1998). Crystallography & NMR System: a new software suite for macromolecular structure determination. *Acta Crystallogr. D* **54**, 905-921.
- Carrington, P.E, Chivers, P.T, Al-Mjeni, F., Sauer, R.T & Maroney, M.J. (2003). Nickel coordination is regulated by the DNA-bound state of NikR. *Nature Struct. Biol.* **10**, 126-130.
- Carugo, O. & Pongor, S. (2002). Protein fold similarity estimated by a probabilistic approach based on C( $\alpha$ )-C( $\alpha$ ) distance comparison. *J. Mol. Biol.* **315**, 887-898.
- Chayen, N.E. (1997). A novel technique to control the rate of vapour diffusion, giving larger protein crystals. *J. Appl. Crystallogr.* **30**, 198-202.
- Chook, Y.M., Lipscomb, W.N. & Ke, H. (1998). Detection and Use of Pseudo-Translation in Determination of Protein Structures. *Acta Crystallogr. D* **54**, 822-827.
- Choudhury, S.B., Lee, J.-W., Davidson, G., Yim, Y.-I., Bose, K., Sharma, M.L., Kang, S.-O., Cabelli, D.E. & Maroney, M.J. (1999). Examination of the Nickel Site Structure and Reaction Mechanism in *Streptomyces seoulensis* Superoxide Dismutase. *Biochemistry* **38**, 3744-3752.
- Chun, J., Youn, H.-D., Yim, Y.-I., Lee, H., Kim, M.Y., Hah, Y.C. & Kang, S.-O (1997). *Streptomyces seoulensis* sp. nov. *Int. J. Syst. Bacteriol.* **47**, 492-498.
- Chung, H.-J., Choi, J.-H., Kim, E.-J., Cho, J.-H. & Roe, J.-H (1999). Negative Regulation of the Gene for Fe-Containing Superoxide Dismutase by an Ni-Responsive Factor in *Streptomyces coelicolor*. *J. Bacteriol.* **181**, 7381-7384.
- Collaborative Computational Project Number 4 (1994). The CCP4 suite: programs for protein crystallography. *Acta Crystallogr. D* **50**, 760-763.

- Cowtan, K. (1994). 'dm': An Automated Procedure for Phase Improvement by Density Modification. *Joint CCP4 + ESF-EACMB Newsletter on Protein Crystallography* **31**, 34-38.
- Darnault, C., Volbeda, A., Kim, E.J., Legrand, P., Vernède, X., Lindahl, P.A. & Fontecilla-Camps, J.C. (2003). Ni-Zn-[Fe<sub>4</sub>-S<sub>4</sub>] and Ni-Ni-[Fe<sub>4</sub>-S<sub>4</sub>] clusters in closed and open  $\alpha$  subunits of acetyl-CoA synthase/carbon monoxide dehydrogenase. *Nature Struct. Biol.* **10**, 271-279.
- Dauter, Z., Dauter, M. & Rajashankar, K.R. (2000). Novel approach to phasing proteins: derivatization by short cryo-soaking with halides. *Acta Crystallogr. D* **56**, 232-237.
- de La Fortelle, E. & Bricogne, G. (1997). Maximum-likelihood heavy-atom parameter refinement for multiple isomorphous replacement and multiwavelength anomalous diffraction methods. *Methods Enzymol.* **276**, 472-494.
- Deng, H.-X., Hentati, A., Tainer, J.A., Iqbal, Z., Cayabyab, A., Hung, W.-Y., Getzoff, E.D., Hu, P., Herzfeldt, B., Roos, R.P., Warner, C., Deng, G., Soriano, E., Smyth, C., Parge, H.E., Ahmed, A., Roses, A.D., Hallewell, R.A., Pericak-Vance, M.A., & Siddique, T. (1993). Amyotrophic lateral sclerosis and structural defects in Cu,Zn superoxide dismutase. *Science* **261**, 1047-1051.
- Diederichs, K. & Karplus, P.A. (1997). Improved R-factors for diffraction data analysis in macromolecular crystallography. *Nature Struct. Biol.* **4**, 269-275 (Erratum in: *Nature Struct. Biol.* **4**, 592).
- Dixon, N.E., Gazzola, C., Watters, J.J., Blakely, R.L. & Zerner, B. (1975). Inhibition of Jack Bean urease (EC 3.5.1.5) by acetohydroxamic acid and by phosphoramidate. An equivalent weight for urease. *J. Am. Chem. Soc.* **97**, 4130-4131.
- Dobbek, H., Svetlitchnyi, V., Gremer, L., Huber, R. & Meyer, O. (2001). Crystal Structure of a Carbon Monoxide Dehydrogenase Reveals a [Ni-4Fe-5S] Cluster. *Science* **293**, 1281-1285.
- Doukov, T.I., Iverson, T.M., Seravalli, J., Ragsdale, S.W. & Drennan, C.L. (2002). A Ni-Fe-Cu Center in a Bifunctional Carbon Monoxide Dehydrogenase/Acetyl-CoA Synthase. *Science* **298**, 567-572.
- Drennan, C.L., Heo, J., Sintchak, M.D., Schreiter, E. & Ludden, P.W. (2001). Life on carbon monoxide: X-ray structure of *Rhodospirillum rubrum* Ni-F-S carbon monoxide dehydrogenase. *PNAS* **98**, 11973-11978.
- Drenth, J. (1999). Principles of Protein X-Ray Crystallography. Second Edition, Springer-Verlag, New York.
- Ducruix, A. & Giegé, R. (Editors) (1999). Crystallization of Nucleic Acids and Proteins. Oxford University Press, New York.

- Edwards, R.A., Whittaker, M.M., Whittaker, J.W., Baker, E.N. & Jameson, G.B. (2001). Outer sphere mutations perturb metal reactivity in manganese superoxide dismutase. *Biochemistry* **40**, 15-27.
- Engh, R.A. & Huber, R. (1991). Accurate Bond and Angle Parameters for X-ray Protein Structure Refinement. *Acta Crystallogr. A* **47**, 392-400.
- Ermler, U., Grabarse, W., Shima, S., Goubeaud, M. & Thauer, R.K. (1997). Crystal Structure of Methyl-Coenzyme M Reductase: The Key Enzyme of Biological Methane Formation. *Science* **278**, 1457-1462.
- Ermler, U., Grabarse, W., Shima, S., Goubeaud, M. & Thauer, R.K. (1998). Active sites of transition-metal enzymes with a focus on nickel. *Curr. Opin. Struct. Biol.* **8**, 749-758.
- Esnouf, R.M. (1999). Further additions to MolScript version 1.4, including reading and contouring of electron-density maps. *Acta Crystallogr. D* **55**, 938-940.
- Evans, G. & Pettifer, R.F. (2001). CHOOCH: a program for deriving anomalous-scattering factors from X-ray fluorescence spectra. *J. Appl. Crystallogr.* **34**, 82-86.
- Falconi, M., O'Neill, P., Stroppolo, M.E. & Desideri, A. (2002). Superoxide Dismutase Kinetics. *Methods Enzymol.* **349**, 38-49.
- Fee, J.A. & Bull, C. (1986). Steady-state Kinetic Studies of Superoxide Dismutases. *J. Biol. Chem.* **261**, 13000-13005.
- Fersht, A. (1999). Structure and Mechanism in Protein Science. W.H. Freeman, New York.
- Finkel, T. & Holbrook, N.J. (2000). Oxidants, oxidative stress and the biology of ageing. *Nature* **408**, 239-247.
- Fontecilla-Camps, J.C., Frey, M., Garcin, E., Hatchikian, C., Montet, Y., Piras, C., Vernède, X. & Volbeda, A. (1997). Hydrogenase: A hydrogen-metabolizing enzyme. What do the crystal structures tell us about its mode of action? *Biochimie* **79**, 661-666.
- French, S. & Wilson, K. (1978). On the Treatment of Negative Intensity Observations. *Acta Crystallogr. A* **34**, 517- 525.
- Fridovich, I. (1989). Superoxide Dismutases. *J. Biol. Chem.* **264**, 7761-7764.
- Fridovich, I. (1995). Superoxide Radical and Superoxide Dismutases. *Annu. Rev. Biochem.* **64**, 97-112.
- Fridovich, I. (1998a). Oxygen Toxicity: A Radical Explanation. *J. Exp. Biol.* **201**, 1203-1209.
- Fridovich, I. (1998b). Oxidative Stress. *Encyclopedia of Life Sciences* <http://www.els.net>, Nature Publishing Group, London.

- Fridovich, I. (2001). Reflections of a Fortunate Biochemist. *J. Biol. Chem.* **276**, 28629-28636.
- Garman, E.F. & Schneider, T.R. (1997). Macromolecular Cryocrystallography. *J. Appl. Crystallogr.* **30**, 211-237.
- Getzoff, E.D., Tainer, J.A., Weiner, P.K., Kollman, P.A., Richardson, J.S. & Richardson, D.C. (1983). Electrostatic recognition between superoxide and copper, zinc superoxide dismutase. *Nature* **306**, 287-290.
- Halliwell, B. & Gutteridge, J.M.C. (1999). Free Radicals in Biology and Medicine. Third Edition, Oxford University Press, Oxford.
- Hanss, J. & Krueger, H.-J. (1998). First Isolation and Structural Characterization of a Nickel(III) Complex Containing Aliphatic Thiolate Donors. *Angew. Chem. Int. Ed.* **37**, 360-363.
- Hart, P.J., Balbirnie, M.M., Ogihara, N.L., Nersissian, A.M., Weiss, M.S., Selverstone Valentine, J. & Eisenberg, D. (1999). A Structure-based Mechanism for Copper-Zinc Superoxide Dismutase. *Biochemistry* **38**, 2167-2178.
- Hausinger, R.P. (2003). Ni and CO: more surprises. *Nature Struct. Biol.* **10**, 234-236.
- Hendrickson, W.A. & Teeter, M.M. (1981). Structure of the hydrophobic protein crambin determined directly from the anomalous scattering of sulfur. *Nature*, **290**, 107-113.
- Holm, L. & Sander, C. (1996). Mapping the protein universe. *Science* **273**, 595-602.
- Holm, R.H, Kennepohl, P. & Solomon, E.I. (1996). Structural and Functional Aspects of Metal Sites in Biology. *Chem. Rev.* **96**, 2239-2314.
- Hough, M.A. & Hasnain, S.S. (2003). Structure of Fully Reduced Bovine Copper Zinc Superoxide Dismutase at 1.15 Å. *Structure* **11**, 937-946.
- Hubbard, S.J. & Thornton, J.M. (1993). 'NACCESS', Computer Program, Department of Biochemistry and Molecular Biology, University College London.
- Inarrea, P. (2002). Purification and Determination of Activity of Mitochondrial Cyanide-Sensitive Superoxide Dismutase in Rat Tissue Extract. *Methods Enzymol.* **349**, 106-114.
- Jabri, E., Carr, M.B., Hausinger, R.P. & Karplus, P.A. (1995). The crystal structure of urease from *Klebsiella aerogenes*. *Science* **268**, 998-1004.
- Jancarik, J. & Kim, S.H. (1991). Sparse matrix sampling: a screening method for crystallization of proteins. *J. Appl. Crystallogr.* **24**, 409-411.
- Jencks, W.P. (1969). Catalysis in Chemistry and Enzymology. Dover Publications, Inc., New York.

- Jones, S. & Thornton, J.M. (1996). Principles of Protein-Protein Interactions Derived From Structural Studies. *PNAS* **93**, 13-20. The internet tool is located at <http://www.biochem.ucl.ac.uk/bsm/PP/server/>.
- Jones, T.A., Zou, J.Y., Cowan, S.W. & Kjeldgaard, M. (1991). Improved methods for building protein models in electron density maps and the location of errors in these models. *Acta Crystallogr. A* **47**, 110-119.
- Karlsson, A., Parales, J.V., Parales, R.E., Gibson, D.T., Eklund, H. & Ramaswamy, S. (2000). The Reduction of the Rieske iron-sulfur cluster in naphthalene dioxygenase by X-rays. *J. Inorg. Biochem.* **78**, 83-87.
- Kim, E.-J., Kim, H.-P., Hah, Y.C. & Roe, J.-H. (1996). Differential expression of superoxide dismutases containing Ni and Fe/Zn in *Streptomyces coelicolor*. *Eur. J. Biochem.* **241**, 178-185.
- Kim, E.-J., Chung, H.-J., Suh, B., Hah, Y.C. & Roe, J.-H. (1998). Transcriptional and post-translational regulation by nickel of sodN gene encoding nickel-containing superoxide dismutase from *Streptomyces coelicolor* Mller. *Mol. Microbiol.* **27**, 187-195.
- Kleywegt, G.J. & Read, R.J. (1997). Not your average density. *Structure* **5**, 1557-1569.
- Kleywegt, G.J. & Jones, T.A. (1998). Databases in Protein Crystallography. *Acta Crystallogr. D* **54**, 1119-1131.
- Klug, D., Rabani, J. & Fridovich, I. (1972). A direct demonstration of the catalytic action of superoxide dismutase through the use of pulse radiolysis. *J. Biol. Chem.* **247**, 4839-4842.
- Kraulis, P.J. (1991). MOLSCRIPT: a program to produce both detailed and schematic plots of protein structures. *J. Appl. Crystallogr.* **24**, 946-950.
- Krüger, H.-J., Peng, G., Holm, R.H. (1991). Low Potential Nickel(III,II) Complexes: New Systems Based on Tetradentate Amidate-Thiolate Ligands and the Influence of Ligand Structure on Potentials in Relation to the Nickel Site in [NiFe]-Hydrogenases. *Inorg. Chem.* **30**, 734-742.
- Kurtz, D.M. & Coulter, E.D. (2002). The mechanism(s) of superoxide reduction by superoxide reductases in vitro and in vivo. *J. Biol. Inorg. Chem.* **7**, 653-658.
- Laskowski, R.A., MacArthur, M.W., Moss, D.S. & Thornton, J.M. (1993). PROCHECK: a program to check the stereochemical quality of protein structures. *J. Appl. Crystallogr.* **26**, 283-291.
- Leclere, V., Boiron, P. & Blondeau, R. (1999). Diversity of superoxide-dismutases among clinical and soil isolates of *Streptomyces* species. *Curr. Microbiol.* **39**, 365-368.

- Lee, J.-W., Roe, J.-H. & Kang, S.-O. (2002). Nickel-containing Superoxide Dismutase. *Methods Enzymol.* **349**, 90-101.
- Leonidas, D.D., Boix, E., Prill, R., Suzuki, M., Turton, R., Minson, K., Swaminathan, G.J., Youle, R.J. & Acharya, K.R. (2001). Mapping the ribonucleolytic active site of eosinophil-derived neurotoxin (EDN). *J. Biol. Chem.* **276**, 15009-15017.
- Leslie, A.G.W. (1992). *Joint CCP4 + ESF-EACMB Newsletter on Protein Crystallography* **26**.
- Liochev, S.I. & Fridovich, I. (2000). Copper- and Zinc-containing Superoxide Dismutase Can Act as a Superoxide Reductase and a Superoxide Oxidase. *J. Biol. Chem.* **275**, 38482-38485.
- Liochev, S.I. & Fridovich, I. (2001). Copper, Zinc Superoxide Dismutase as a Univalent NO<sup>-</sup> Oxidoreductase and as a Dichlorofluorescein Peroxidase. *J. Biol. Chem.* **276**, 35253-35257.
- Liochev, S.I. & Fridovich, I. (2002). Nitroxyl (NO<sup>-</sup>): a Substrate for Superoxide Dismutase. *Arch. Biochem. Biophys.* **402**, 166-171.
- Maliekal, J., Karapetian, A., Vance, C., Yikilmaz, E., Wu, Q., Jackson, T., Brunold, T.C., Spiro, T.G. & Miller, A.-F. (2002). Comparison and Contrasts between the Active Site PKs of Mn-Superoxide Dismutase and Those of Fe-Superoxide Dismutase. *J. Am. Chem. Soc.* **124**, 15064-15075.
- Maroney, M.J., Davidson, G., Allan, C.B. & Figlar, J. (1998). The Structure and Function of Nickel Sites in Metalloproteins. *Structure and Bonding* **92**, 1-65.
- Maroney, M.J. (1999). Structure/function relationships in nickel metallobiochemistry. *Curr. Opin. Chem. Biol.* **3**, 188-199.
- Matthews, B.W. (1968). Solvent content of protein crystals. *J. Mol. Biol.* **33**, 491-497.
- McCord, J.M. & Fridovich, I. (1969). Superoxide Dismutase. An enzymic function for erythrocyte hemocuprein. *J. Biol. Chem.* **244**, 6049-6055.
- McCord, J.M. (2000). The Evolution of Free Radicals and Oxidative Stress. *Am. J. Med.* **108**, 652-659.
- McPherson, A.J. (1999). Crystallization of Biological Macromolecules. Cold Spring Harbor Laboratory Press, New York.
- Merritt, E.A. & Bacon, D.J. (1997). Raster3D: photorealistic molecular graphics. *Methods Enzymol.* **277**, 505-524.
- Merritt, E.A. (2001). "X-ray Anomalous Scattering", an internet tool located at [http://www.bmsc.washington.edu/scatter/AS\\_index.html](http://www.bmsc.washington.edu/scatter/AS_index.html).

- Montet, Y., Amara, P., Volbeda, A., Vernede, X., Hatchikian, E.C., Field, M.J., Frey, M. & Fontechilla-Camps, J.C. (1997). Gas excess to the active site of Ni-Fe hydrogenase probed by X-ray crystallography and molecular dynamics. *Nature Struct. Biol.* **7**, 523-526.
- Morais, M.C., Baker, A.S., Dunaway-Mariano, D. & Allen, K.N. (2000). Crystallization and preliminary crystallographic analysis of phosphonoacetaldehyde hydrolase. *Acta Crystallogr. D* **56**, 206-209.
- Mulrooney, S.B. & Hausinger, R.P. (2003). Nickel uptake and utilization by microorganisms. *FEMS Microbiol. Rev.* **27**, 239-261.
- Murshudov, G.N, Vagin, A.A. & Dodson, E.J. (1997). Refinement of Macromolecular Structures by the Maximum-Likelihood Method. *Acta Crystallogr. D* **53**, 240-255.
- Nicholls, A., Sharp, K.A. & Honig, B. (1991). Protein folding and association: insights from the interfacial and thermodynamic properties of hydrocarbons. *Proteins* **11**, 281-296.
- Orpen, A.G., Brammer, L., Allen, F.H., Kennard, O., Watson, D.G. & Taylor, R. (1989). Tables of bond lengths determined by X-ray and Neutron Diffraction. Part 2. *J. Chem. Soc. Dalton Trans.*, Supplement.
- Otwinowski, Z. & Minor, W. (1997). Processing of X-ray diffraction data collected in oscillation mode. *Methods Enzymol.* **276**, 307-326.
- Perrakis, A., Sixma, T.K., Wilson, K.S. & Lamzin, V.S. (1997). wARP: Improvement and Extension of Crystallographic Phases by Weighted Averaging of Multiple Refined Dummy Atomic Models. *Acta Crystallogr. D* **53**, 448-455.
- Perrakis, A., Morris, R. & Lamzin, V.S. (1999). Automated protein model building combined with iterative structure refinement. *Nature Struct. Biol.* **6**, 458-463.
- Que, L. (Editor) (2000). Physical Methods in Bioinorganic Chemistry. University Science Books, Sausalito (CA), USA.
- Ragsdale, S.W. (1998). Nickel biochemistry. *Curr. Opin. Chem. Biol.* **2**, 208-215.
- Read, R.J. (1986). Improved fourier coefficients for maps using phases from partial structures with errors. *Acta Crystallogr. A* **42**, 148-157.
- Rossmann, M.G. & Arnold, E. (Editors) (2001). International Tables for Crystallography, Vol. F (Crystallography of biological macromolecules). Kluwer Academic Publishers, Dordrecht, The Netherlands.
- Rost, B. & Sander, C. (1993). Prediction of Protein secondary Structure at better than 70% accuracy. *J. Mol. Biol.* **232**, 584-599.

- Salvemini, D., Wang, Z.-Q., Zweier, J.L., Samouilov, A., Macarthur, H., Misko, T.P., Currie, M.G., Cuzzocrea, S., Sikorski, J.A. & Riley, D.P. (1999). A Nonpeptidyl Mimic of Superoxide Dismutase with Therapeutic Activity in Rats. *Science* **286**, 304-306.
- Schreuder, H.A, Groendijk, H., van der Laan, J.M. & Wierenga, R.K. (1988). The transfer of protein crystals from their original mother liquor to a solution with a completely different precipitant. *J. Appl. Crystallogr.* **21**, 426-429.
- Shannon, R.D. (1976). Revised Effective Ionic Radii and Systematic Studies of Interatomic Distances in Halides and Chalcogenides. *Acta Crystallogr. A* **32**, 751-767.
- Sheldrick, G.M. (2002). Macromolecular phasing with SHELXE. *Z. Kristallogr.* **217**, 644-650.
- Sjögren, T., Carlsson, G., Larsson, G., Hajdu, A., Andersson, C., Pettersson, H. & Hajdu, J. (2002). Protein crystallography in a vapour stream: data collection, reaction initiation and intermediate trapping in naked hydrated protein crystals. *J. Appl. Crystallogr.* **35**, 113-116.
- Sousa, R. & Lafer, E.M. (1990). The Use of Glycerol in Crystallization of T7 RNA Polymerase: Implications for the Use of Cosolvents in Crystallizing Flexible Proteins. *Methods* **1**, 50-56.
- Stura, E.A. (1999) in: Crystallization of Nucleic Acids and Proteins, Chapter 7. Ed. by A. Ducruix & R. Giegé. Oxford University Press, New York.
- Tainer, J.A., Getzoff, E.D., Richardson, J.S. & Richardson, D.C. (1983). Structure and mechanism of copper, zinc superoxide dismutase. *Nature* **306**, 284-287.
- Terwilliger, T.C. & Berendzen, J. (1999). Automated MAD and MIR structure solution. *Acta Crystallogr. D* **55**, 849-861.
- Thaller, C., Weaver, L.H., Eichele, G., Wilson, E., Karlsson, R. & Jansonius, J.N. (1981). Repeated seeding technique for growing large single crystals of proteins. *J. Mol. Biol.* **147**, 465-469.
- Thauer, R.K. (2001). Nickel to the Fore. *Science* **293**, 1264-1265.
- Thompson, J.D., Higgins, D.G. & Gibson, T.J. (1994). CLUSTAL W: improving the sensitivity of progressive multiple sequence alignment through sequence weighting, position-specific gap penalties and weight matrix choice. *Nucleic Acids Res.* **22**, 4673-4680.
- Tong, L. & Rossmann, M.G. (1997). *Methods Enzymol.* **276**, 594-611.
- Volbeda, A., Charon, M.H., Piras, C., Hatchikian, E.C., Frey, M. & Fontecilla-Camps, J.C. (1995). Crystal structure of the nickel-iron hydrogenase from *Desulfovibrio gigas*. *Nature* **373**, 580-587.

- Watt, R.K. & Ludden, P.W. (1999). Nickel-binding proteins. *Cell. Mol. Life Sci.* **56**, 604-625.
- Wilson, A.J.C. (1942). Determination of absolute from relative X-ray data intensities. *Nature* **150**, 151-152.
- Wuerges, J., Lee, J.-W., Kang, S.-O. & Djinovic Carugo, K. (2002). Crystallization of a Nickel-containing Superoxide Dismutase and Preliminary Phase Determination by MAD at the Ni K-edge. *Acta Crystallogr. D* **58**, 1220-1223.
- Wuerges, J., Lee, J.-W., Yim, Y.-I., Yim, H.-S., Kang, S.-O. & Djinovic Carugo, K. (2003). Crystal structure of nickel-containing superoxide dismutase reveals a novel nickel active site. Submitted for publication.
- Yost, F.T. & Fridovich, I. (1973). An iron-containing superoxide dismutase from *Escherichia coli*. *J. Biol. Chem.* **248**, 4905-4908.
- Youn, H.-D., Youn, H., Lee, J.-W., Yim, Y.-I., Lee, J. K., Hah, Y. C. & Kang, S.-O. (1996a). Unique Isozymes of Superoxide Dismutase in *Streptomyces griseus*. *Arch. Biochem. Biophys.* **334**, 341-348.
- Youn, H.-D., Kim, E.-J., Roe, J.-H., Hah, Y. C. & Kang, S.-O. (1996b). A novel nickel-containing superoxide dismutase from *Streptomyces spp.* *Biochem. J.* **318**, 889-896.